Spring 1-1-2014

Cooperative Planning for UAS-based Sensor Networks In Realistic Communication Environments

Maciej Stachura
University of Colorado Boulder, stachura@colorado.edu

Cooperative Planning for UAS-based Sensor Networks In Realistic Communication Environments

by

M. Stachura

M.Eng., Aerospace Engineering, University of Colorado, 2009

A thesis submitted to the

Faculty of the Graduate School of the

University of Colorado in partial fulfillment

of the requirements for the degree of

Doctor of Philosophy

Department of Aerospace Engineering Sciences

2014

This thesis entitled:
Cooperative Planning for UAS-based Sensor Networks In Realistic Communication Environments
written by M. Stachura
has been approved for the Department of Aerospace Engineering Sciences

Eric W. Frew

Brian M. Argrow

Date

The final copy of this thesis has been examined by the signatories, and we find that both the content and the form meet acceptable presentation standards of scholarly work in the above mentioned discipline.

Stachura, M. (Ph.D. Candidate, Aerospace Engineering)

Cooperative Planning for UAS-based Sensor Networks In Realistic Communication Environments

Thesis directed by Prof. Eric W. Frew

This dissertation develops a unified, tractable algorithm for distributed planning for multiple unmanned aircraft based sensor networks with performance bounds. An information-theoretic objective function is derived that incorporates sensing and communication to guide a cooperative team of unmanned aircraft. The communication is modelled with packet erasure channels for each link in a multi-hop mesh network. This objective is shown to be intractable and assumptions are made to find a tractable formulation. This tractable formulation is then distributed using the chain rule of mutual information and optimization algorithms are designed with performance bounds for different scenarios and compared against the fully centralized mutual information approach. This comparison is done analytically using submodularity under certain assumptions and Monte Carlo simulations to evaluate the algorithms when these assumptions break down.

A novel unmanned aircraft system platform was developed to facilitate experiments with multiple unmanned aircraft utilizing sensing and multi-hop mesh networking. This system was used to perform localization experiments of radio frequency emitters based on the received signal strength measurement. The planning algorithms were demonstrated with multiple aircraft to show there validity and tractability on a real world scenario. These experiments were used to asses the algorithms performance showing the improvement in sensing is appreciable and specifically the benefits of utilizing multi-hop communication.

Acknowledgements

First and foremost I'd like to thank my advisor, Eric Frew, for all of his support during my tenure as a graduate student. This work would not have been possible without his guidance and instruction. I'd also like to thank Brian Argrow for all of his help over the years, specifically related to flight testing and certification. My committee members, Ute Herzfeld, Tim Brown, and Nikolaus Correll also provided important guidance. This dissertation work was made possible by significant contributions from other students and staff at RECUV. I'd like to thank my elders, Cory Dixon and Jack Elston, who's significant work on the systems and software for RECUV's fleet of UAS made my work possible. Also, a big thanks to the other RECUV graduate students for all of their help over the years, specifically Holly Borowski, Tony Carfang, Jason Durrie, Tristan Gerritsen, Craig Turansky, and Neeti Wagle. Also, a big thanks to all of my pilots, Tom Aune, Greg Hine, James and John Mack, Jason Roadman and Doug Weibel for the long hours spent in the field with me. Finally I'd like to thank my family for their support and encouragement. Mom, dad, Maja, Phil, Ola, and Andrzej, this dissertation is dedicated to you.

Contents

Chapter

Tables

Table

Figures

Figure

Chapter 1

Introduction

Autonomous robot sensor networks are becoming a useful tool to gather information for many applications. In field deployments, especially those involving unmanned aircraft, the performance of the wireless communication subsystem is one of the main limitations affecting the performance of a network comprised of multiple vehicles [5]. In many cooperative information-gathering tasks, utilizing robotic sensor networks can result in conflicts between moving the robots to improve sensing performance versus ensuring good communication in order to share data and plans with each other. Communication requirements typically favor moving robots in the network closer together while sensing requirements often favor moving robots further apart, e.g. as they move closer to different tasks or targets.

1.1 Overview

The overall goal of this work is to control a cooperative unmanned aircraft system (UAS) sensor network in realistic information gathering scenarios that allows different communication schemes. The methodology to achieve this is the design of an efficient, unified approach that factors in sensing and communication into a single quantity that can be distributed locally to each aircraft. This work includes the analysis of the planning methods and examining the performance bounds.

Several challenges need to be addressed to achieve the goals of this work. First and foremost is formulating a planning algorithm that allows proper coordination between the vehicles. Factoring in the communication into this formulation is another key challenge. Computation of the utility function is made difficult by allowing multi-hop communication which will make the capabilities of the network a function of

the global configuration of the team. Further, a communication aware planning algorithm must be designed to run in real-time given the limited computationally abilities on small UAS.

Given this goal and these challenges, the algorithm developed, implemented, and assessed in this dissertation solves the problem of controlling a network of cooperative vehicles to perform information gathering tasks. The key features of the approach in the algorithm in this dissertation include:

- Distributed planning across the aircraft.
- Stochastic modeling of sensing and communication.
- Unified, efficient approach.
- Incorporates direct and multi-hop communication.

One example application of communication aware information gathering, which will be used throughout this dissertation to assess the control approach, is localization of radio frequency (RF) emitters by a team of unmanned aircraft (Figure 1.1).

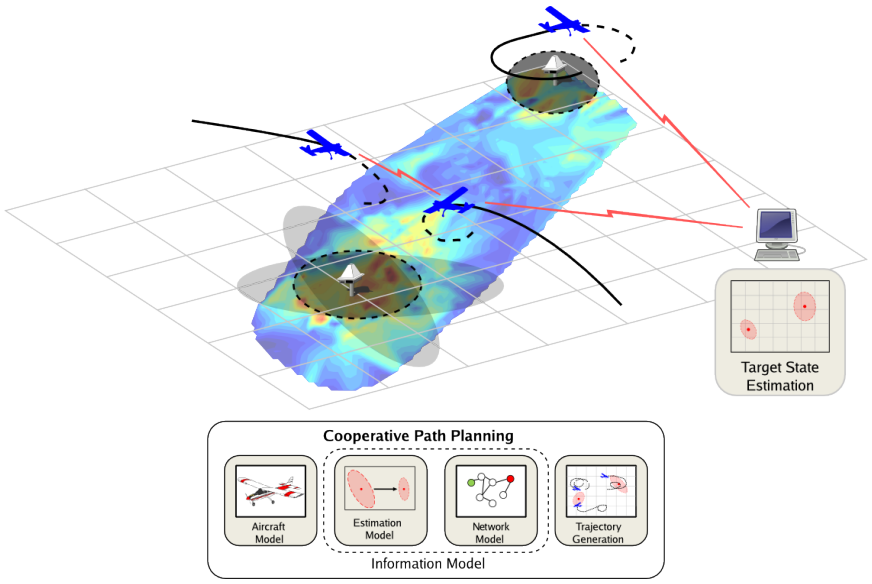

Figure 1.1: Overview of an example system that could use the algorithms described in this dissertation. Here there are three aircraft localizing two ground targets with a stationary fusion center processing the measurements.

1.2 Related Work

Distributed planning by robotic sensor networks has been studied extensively using information-theoretic metrics, e.g. mutual information or conditional entropy, without considering communication limitations in the problem formulation (as opposed to the related problem of assuring the algorithm itself performances well in the face of limited communication) [3, 15, 24, 16, 42, 56]. When the problem is linear, or linearized, and noise terms are Gaussian, optimal information gathering is done by minimizing a norm of the uncertainty captured in the error covariance matrix [15, 24, 3]. For general non-linear problems with non-Gaussian distributions, mixture models [25] or particle filters [16, 42] can be utilized to propagate probability distributions and approximate the information metrics. When using the mutual information planning metric, submodularity can be used to derive performance bounds of the distributed planner under the assumption the measurements are independent conditioned on the state being estimated [56].

A variety of different methods have been used to incorporate communication performance explicitly into distributed planning algorithms. One approach is to impose geometric constraints on the sensor network to maintain communication performance while optimizing a task-specific objective. Generally the geometric constraints require robots to stay in close proximity to one another, where the allowable separation distance is derived to maintain connectivity based on a disk communication model [44, 60] or to attain a given communication rate [10, 23]. An alternative to hard motion constraints is to implicitly restrict the motion by creating virtual forces between the vehicles that maintains a minimum range between vehicles while the primary task is performed [51]. A third approach treats assured communication as a task that can be assigned as part of a task allocation scheme [30, 21]. In those approaches, the overall objective depends on the achieved data rate or bit error rate of the communication network, and vehicles that are under-utilized in other tasks can be assigned to focus on improving data rate and maintaining connectivity [30]. A fourth approach considers the problem of reducing network bandwidth used for coordination by only communicating when necessary or useful [19, 2]. Finally, joint control of robot mobility and communication has been achieved for classes of data gathering problems [59, 61, 58].

Distributed planning that includes communication in the utility function is complicated by the fact

that overall performance is dependent on both sensing (getting the best measurements) and communication (getting the measurements to the best locations). Furthermore, sensing and communication are both stochastic functions of the individual robot capabilities, the robot sensor network configuration, and the external environment. Optimal information gathering needs an efficient, unifying approach that balances the contributions of sensing and communication appropriately. Geometric approaches tend to provide communication networks that stay connected and maintain feasible solutions, but can be conservative in terms of collecting sensor information. Task allocation strategies provide additional flexibility by treating sensing and communication equally, but can become intractable due to the combinatorial optimization over all possible sensing and communication allocations.

Another major approach to address path planning where the planner's objective communication is the bi-criteria approach of optimizing sensing performance and communication performance [22, 2, 19]. For static sensor networks, the network can be configured through a distributed process to either minimize the information-theoretic sensing uncertainty while constraining the number of expected data (re)transmissions or to minimize the number of data (re)transmissions while constraining the sensing cost [22]. Alternatively, communication bandwidth can be reduced in multi-hop mobile sensor networks when each robot only transmits *useful* data to its neighbors, where the *usefulness* metric is based on the distance between the distributions of the local and global estimates of the team sensing objective [2]. A limitation of the bi-criteria approach is that the performance will depend on user selected parameters. In general it is not clear how to select the constraints on either the sensing or communication.

This dissertation along with similar work [47, 14] specifically looks at developing an algorithm that computes the probability that an individual measurement gets through the network to a fusion center and optimizes the expected improvement in the sensing objective. When a single fixed base station is used, the communication channel can be estimated online and sensing can be performed via gradient descent to maximize the expected improvement in the Fisher Information Matrix [14]. Work published over the course of this thesis examined the case of receding horizon control utilizing multi-hop communication and plans over a fixed hierarchy to improve coordination of a team of vehicles [47]. The communication model is fixed throughout the mission and based on empirical data. The extension to multi-hop communication schemes

are shown in that paper to be a non-trivial. The resulting approach described in this dissertation can be viewed as encapsulating the approaches in Ref. [14] and Ref. [47], and can easily exploit online learning of the communication environment [14, 54].

The goal of the planning algorithms developed in this dissertation is to improve the sensing capabilities of teams of UAS with communication limitations. To assess these planning algorithms the sensing task of localizing ground-based RF emitters will be used. Most of the related work in RF localization has focused on indoor environments where the position of the sensor platform being controlled is found from the known positions of several access points, prior knowledge of the RSSI map [57], or simultaneous localization and mapping (SLAM) [9]. For the problem examined here the sensor platform, i.e. the unmanned aircraft (UA), already knows its position accurately through a combination of GPS and inertial sensors. However, it is assumed that it has no knowledge of the stationary ground nodes, and is tasked with geo-locating them using only RSSI measurements. Similar work was done by Fudge et al [13] using a binary Bayesian grid filter for both search and localization of RF emitters by a team of UA. The RF emitters in that paper were based on the Family Radio Service at 462.6375MHz. Work done by Kim et al [20] looked at localizing transient sources at the 2.4GHz frequency based on 802.15.4, specifically the ZigBee standard. Their work utilized the ratio of signal strength measurements between two robots and coordinated their movement to improve estimation. Their work was demonstrated in simulation. The same group also did experiments [43] with a single ground vehicle employing a directional antenna to localize ZigBee radios.

The algorithms presented in this dissertation will overcome several limitations of the related work. The derived mutual information utility that models both sensing and communication avoids the need for user selected parameters seen in the task allocation and bi-criteria schemes mentioned above. The conservative nature of the geometric approaches is overcome by the distributed mutual information utility that allows direct comparison against the full mutual information using both analytical and empirical bounds. The communication model in mutual information derivation allows for both direct and multi-hop communication schemes.

1.3 Detailed Problem and Solution

This dissertation addresses developing a unified, tractable algorithm for distributed planning for multi-UA based sensor networks with performance bounds. The detailed problem is to derive an information-theoretic objective function that incorporates sensing and communication and is tractable. This includes the design of distributed optimization algorithms with performance bounds for different scenarios. The solution to this problem is to derive mutual information for the case of coordinated sensor fusion over packet erasure channels that can include multi-hop communication. Given that the packet erasure channel is a stochastic model, mutual information combines the sensing and communication into a single utility metric that is a function of sensor state (e.g. robot position). Calculation of the mutual information is difficult for general sensing problems and includes enumeration over the power set of all possible communication links and time steps. As a result, this work introduces several simplifications in order to derive a tractable utility function that still maintains important properties of the mutual information utility.

A key part of the presented solution is assessing the performance of the presented algorithms. In particular, bounds on the performance of a distributed planning scheme are compared against the global optimum for scenarios that exhibit submodularity. It will be shown that certain network protocols, such as direct communication, provide submodular formulations while multi-hop communication schemes lose submodularity and guaranteed optimality bounds. Monte Carlo simulations are used to assess the performance and bounds of this approach. UAS flight experiments are used, specifically performing RF localization experiments for several different scenarios to demonstrate and assess the algorithms described in this work.

1.4 Contributions

This dissertation makes three key contributions: (1) derivation of the metric for controlling UAS sensor networks, (2) development and assessment of the distributed planning algorithm, (3) UAS development, flight experiments, and the demonstration and assessment of the planning algorithms.

(1) The metric for controlling the sensor networks is derived by combining sensing and communication into a single metric based on mutual information. This metric includes assumptions to allow a

tractable solution. A local utility function is derived that enables distributed optimization with performance bounds under certain conditions. The communication model is based on a packet erasure channel model and the formulation works with both direct and multi-hop communication schemes.

(2) The development and assessment of the distributed planning algorithm is central in this work. Algorithms utilizing the information metric to control the UAS sensor network for different network classes are derived. Assessment of the performance of these planning algorithms is done through several comparisons. It is shown that computing the mutual information over a general multi-hop sensor network is not tractable, so assumptions are made on the network model to simplify the calculation. Numerical assessments are done to show that this simplification still results in good performance of the planning algorithms in many cases. This simplified algorithm is also distributed across the vehicles. It is shown that for the assumptions of direct communication the result of the planner is analytically bounded to no worse than one half the optimal solution, though Monte Carlo simulations show that performance is typically significantly better than this bound. Finally, simulations are performed for the multi-hop communication model and shown to still have good performance compared to the centralized solution even in the absence of analytical bounds.

(3) The experimental contributions can be separated into three parts:

   (a) Several different UAS platforms were created for flight experiments to assess the algorithms developed in this work. This contribution included the NexSTAR UAS for localizing 2.4GHz RF emitters along with the multi-UA RF sensing system, comprised of the Tempest and Skywalker X8, for localizing 433MHz RF emitters along with single and multi-UA planning experiments. This contribution included significant additions to the current software suite used by the Research and Engineering Center for Unmanned Vehicles (RECUV) and contributed to the acquisition of many Certificates of Authorization (COAs) from the Federal Aviation Administration for flight of the UAS.

   (b) Flight experiments to design, test, and assess localization of RF sources. Experiments were

flown to show localization of 2.4GHz WiFi emitters utilizing an unscented Kalman filter (UKF). These experiments were used to assess different state vectors, antenna types, and other features. RF localization experiments were also flown for 433MHz emitters and used to compare different filter formulations, primarily the extended Kalman filter (EKF), UKF, and particle filter (PF).

(c) The culmination of this work was flight experiments of the distributed path planning algorithm. Single UA experiments utilizing the path planning algorithms were flown for the 433MHz localization problem. These experiments were used to assess the performance of active path planning for sensing and showed significant improvement compared against non path planning flights. Multi-UA experiments were flown to demonstrate the full distributed path planning algorithm and assess performance. Comparisons were made between direct communication and multi-hop network topologies and it was shown that for certain scenarios the increased range of a multi-hop network results in significant improvements in sensing. The flight experiments also demonstrated with multiple aircraft the tractability of these algorithms in a real world scenario.

Chapter 2

System Models

This chapter presents and derives the models used in the path planning. The goal of this work is using mutual information, the most common metric for information quantity, for distributed sensing over packet erasure channels that model multi-hop communication. The information dynamics are derived in this chapter along with the sensing, communication, and aircraft dynamics models specifically used in the simulations and experiments to evaluate the planning algorithms. The sensing problem used in this work is the localization of stationary RF emitters using the received signal strength as provided by the received signal strength indicator (RSSI) measurement. The simulation evaluation also included bearings only tracking of moving targets. The communication link model is the packet erasure channel model using both direct communication and multi-hop. The aircraft dynamics model is a non-holonomic vehicle model.

2.1 Information Dynamics

This section derives distributed information dynamics based on the mutual information between an unknown state of interest and measurements made by the sensors of the individual agents in a mobile sensor network. Consider an unknown state vector of interest $\mathbf{x}_k$ (e.g. the position of a moving ground target) that evolves according to discrete-time nonlinear dynamics

$$\mathbf{x}_{t+1} = f_x(\mathbf{x}_t, \mathbf{w}_t) \tag{2.1}$$

where t is the discrete time and $\mathbf{w}_t$ is a random disturbance vector that encapsulates the unknown inputs and disturbances in the state transition function. Further, consider the set S of N mobile sensors such that

each sensor $n \in S$ produces an observation $\mathbf{y}_t^n$ based on the nonlinear observation function

$$\mathbf{y}_t^n = h_n(\mathbf{x}_t, \mathbf{s}_t^n, \mathbf{v}_t^n) \tag{2.2}$$

where $\mathbf{s}_t^n$ is the sensor state (e.g. the position of a robot carrying the sensor) at time t and $\mathbf{v}_t^n$ is random sensor noise. Let each sensor state evolve according to deterministic nonlinear dynamics

$$\mathbf{s}_{t+1}^n = f_{s,n}(\mathbf{s}_t^n, \mathbf{u}_t^n) \tag{2.3}$$

where $\mathbf{u}_t^n$ is the control input for sensor i. For ease of notation combine variables for the individual agents into single vectors, so let $\mathbf{y}_t = [\mathbf{y}_t^1, \cdots, \mathbf{y}_t^N]^T$, $\mathbf{s}_t = [\mathbf{s}_t^1, \cdots, \mathbf{s}_t^N]^T$, $\mathbf{u}_t = [\mathbf{u}_t^1, \cdots, \mathbf{u}_t^N]^T$, and $\mathbf{s}_{t+1} = f_{s,}(\mathbf{s}_t, \mathbf{u}_t) = [f_{s,1}(\mathbf{s}_t^1, \mathbf{u}_t^1), \cdots, f_{s,N}(\mathbf{s}_t^N, \mathbf{u}_t^N)]^T$. Further, consider the case where the measurement $\mathbf{y}_t^n$ is sent over a *packet erasure channel* [4] that successfully delivers packets with probability $\beta_t^n(\mathbf{s}_t)$. Let $\mathbf{z}_t^n$ be the measurement received at the fusion center, then

$$\begin{aligned} \text{Prob}(\mathbf{z}_t^n = \mathbf{y}_t^n) &= \beta_t^n(\mathbf{s}_t) \\ \text{Prob}(\mathbf{z}_t^n = \emptyset) &= 1 - \beta_t^n(\mathbf{s}_t) \end{aligned} \tag{2.4}$$

Finally, let $p(x_t)$ be the probability distribution function of $\mathbf{x}_t$ with first and second moments (mean and covariance matrix) μ_t and P_t, respectively. Figure 2.1 is a graphical illustration of what this Markov chain looks like.

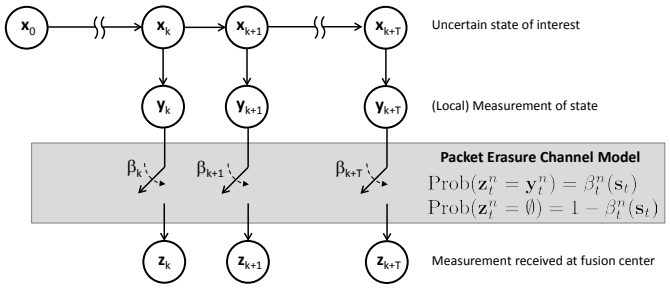

Figure 2.1: Markov chain with packet erasure channel.

2.1.1 Mutual Information

Let $X_T = \{\mathbf{x}_1, \cdots, \mathbf{x}_T\}$ be the sequence of states over the time interval from 1 to T. Let $Y_T = \{\mathbf{y}_1, \cdots, \mathbf{y}_T\}$ be the future measurements to be taken over that same interval where $\mathbf{y}_t = \{\mathbf{y}_t^1, \cdots, \mathbf{y}_t^n\}$.

Similarly, let $B_T = \{\mathbf{b}_1, \cdots, \mathbf{b}_T\}$, where $\mathbf{b}_t = \{b_t^1, \cdots, b_t^N\}$, be an indicator variable describing the network configuration over that same interval where $b_t^n \sim \text{Bern}\left(\beta_t^n(\mathbf{s}_t)\right)$ is a binary variable drawn from a Bernoulli distribution with probability β_t^n. Next, let Z_T be similarly defined as Y_T with the exceptions that these are only the measurements received at the fusion center. Finally, let $z_{i:j}^{n:m}$ be the set of measurements taken by sensors n through m over the time interval from i to j (with similar definitions for $y_{i:j}^{n:m}$ and $B_{i:j}^{n:m}$).

In this work the mutual information $I(X_T; Z_T)$ is used as the measure of information and is defined as the expected reduction in entropy:

$$I(X_T; Z_T) = H\left(X_T\right) - H\left(X_T | Z_T\right) \tag{2.5}$$

where $H\left(X_T\right)$ is the entropy of X_T and $H\left(X_T | Z_T\right)$ is the conditional entropy given the measurement sequence Z_T.

Calculation of mutual information for a Markov chain can be simplified by exploiting several key properties. A common approach is to apply the mutual information chain rule over time in order to derive a (temporally) sequential description of mutual information [56]. Since this work is concerned with distributed planning the chain rule of mutual information is instead applied over the vehicles first and then time.

$$\begin{aligned} I(X_T; Z_T) &= \sum_{n=1}^{N} I\left(X_T; \mathbf{z}_{1:T}^n | \mathbf{z}_{1:T}^{1:n-1}\right) \\ &= \sum_{n=1}^{N} \sum_{i=1}^{T} I\left(X_T; \mathbf{z}_t^n | \mathbf{z}_{1:t-1}^n, \mathbf{z}_{1:T}^{1:n-1}\right) \\ &= \sum_{n=1}^{N} \sum_{i=1}^{T} I\left(\mathbf{x}_t; \mathbf{z}_t^n | \mathbf{z}_{1:t-1}^n, \mathbf{z}_{1:T}^{1:n-1}\right) \end{aligned} \tag{2.6}$$

The first equality is due to the chain rule applied over vehicles and is shown graphically in Figure 2.2. The y-axis represents the time from $1:T$ and the x-axis the vehicle number from $1:N$. Each dot represents a measurement z_t^n. The second equality is from the chain rule applied over time for each vehicle. This is

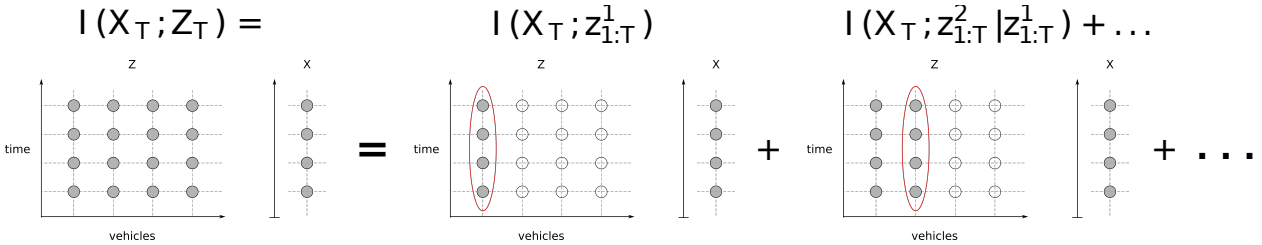

Figure 2.2: Graphical representation of the chain rule of mutual information.

shown graphically in Figure 2.3 for vehicle 3. The third equality is due to the Markov structure [56].

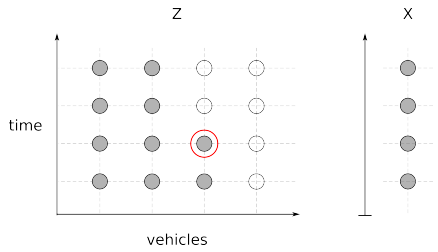

Figure 2.3: Graphical representation of the chain rule applied over time for vehicle 3.

The presence of the packet erasure channel complicates the calculation of the mutual information. However, additional structure in the graphical model can be exploited. In particular, from the Law of Total Probability [62] the term under the summation in (2.6) can be rewritten

$$\begin{aligned} & I\left(\mathbf{x_t}; \mathbf{z}_t^n | \mathbf{z}_{1:t-1}^n, \mathbf{z}_{1:T}^{1:n-1}\right) \\ & = \sum_{\chi_k} \{ I\left(\mathbf{x}_t; \psi_t^n | \psi_{1:t-1}^n, \psi_{1:T}^{1:n-1}\right) | B_{t,n} = \chi_k \} \cdot p_B(\chi_k) \end{aligned} \tag{2.7}$$

where ψ_t^n is the specific set of measurements received at the base station for a given $B_{t,n}$, i.e. with

$$\psi_t^n = \begin{cases} \mathbf{y}_t^n & b_t^n = 1 \\ \emptyset & b_t^n = 0 \end{cases} \tag{2.8}$$

The probability distribution function $p_B(\chi_k)$ describes the indicator vector $B_{t,n}$. Because the indicator variable is binary, $B_{t,n}$ comes from the discrete power set $2^{|B_{t,n}|}$ and thus the probability of every possible vector can be determined through enumeration from the packet erasure channel model. For example, for the case of a single sensor over 5 time steps, if $\chi_k = [1,0,1,0,0]^T$ then $p_B(\chi_k) = \beta_1(1-\beta_2)\beta_3(1-\beta_4)(1-\beta_5)$. Figure 2.4 graphically shows this calculation. The white dots represent a dropped measurement and the black represent a successful transmission at one instance in time/vehicle for the computation.

Calculation of $I\left(\mathbf{x}_t; \psi_t^n | \psi_{1:t-1}^n, \psi_{1:T}^{1:n-1}\right)$ is still difficult in general, so for the purposes of planning, this work assumes that a linearized, Gaussian model captures the dynamic behavior of the probability distribution of $p(\mathbf{x}_t)$ well enough. Linearizing the state dynamics about the trajectory of the mean of $p(\mathbf{x}_t)$, the state equations become

$$\begin{aligned} \mathbf{x}_{t+1} &\approx \Phi_t \cdot (\mathbf{x}_t - \mu_t) + \Gamma_t \cdot \mathbf{w}_t + f_x(\mu_t, 0) \\ \mathbf{y}_{n,t} &\approx H_{n,t} \cdot (\mathbf{x}_t - \mu_t) + \mathbf{v}_{n,t} + h_n(\mu_t, \mathbf{s}_{n,t}, 0) \end{aligned} \tag{2.9}$$

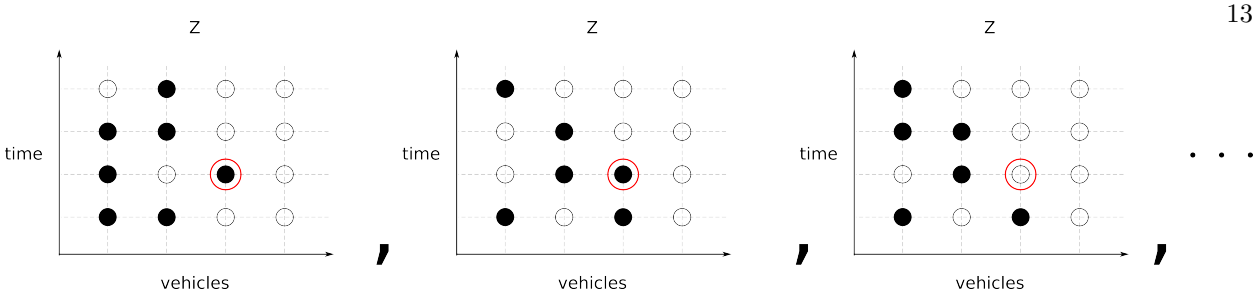

Figure 2.4: Graphical representation of the mutual information over the total probability.

where $\Phi_t = \nabla_{\mathbf{x}} f_x(\mu_t, 0)$, $\Gamma_t = \nabla_{\mathbf{w}} f_x(\mu_t, 0)$, $H_{n,t+1} = \nabla_{\mathbf{x}} h_n(\mu_t, \mathbf{s}_{n,t}, 0)$, and the process noise $\mathbf{w}_t$ and sensor noise terms $\mathbf{v}_{n,t}$ are assumed to be Gaussian white noise with covariance matrices $E[\mathbf{w}_t \mathbf{w}_t^T] = Q_t$ and $E[\mathbf{v}_{n,t} \mathbf{v}_{n,t}^T] = R_{n,t}$. The closed-loop trajectory of the mean μ_t depends on the actual future measurements that will be taken by the sensors. As a result, an additional assumption is needed, namely that the maximum-likelihood measurements are taken. In this case the closed loop trajectory of the mean of the system given by Equation 2.9 is equivalent to the open loop trajectory of the mean of the initial distribution, i.e.

$$\mu_{t+1} = f_x(\mu_t, 0) \equiv f_\mu(\mu_t). \tag{2.10}$$

Given the linear system description in Equation 2.9, the mutual information $I\left(\mathbf{x}_t; \psi_t^n | \psi_{1:t-1}^{1:N}, \psi_t^{1:n-1}\right)$ can now be derived. Let M_t^{n-} and M_t^{n+} be the information matrices (inverse covariance matrices) for the state $\mathbf{x}_t$ at time t given the measurements $\{\psi_{1:t-1}^n, \psi_{1:T}^{1:n-1}\}$ and $\{\psi_{1:t-1}^{1:N}, \psi_t^{1:n-1}, \psi_t^n\}$, respectively. The entropy of a Gaussian distribution is[1]:

$$H(\mathbf{x}) = -\frac{1}{2} \log\left[(2\pi e)^p |M|\right] \tag{2.11}$$

where $\mathbf{x} \in \mathbb{R}^p$ and $M \in \mathbb{R}^{p \times p}$ is the information matrix, so the mutual information is:

$$I\left(\mathbf{x}_t; \psi_t^n | \psi_{1:t-1}^n, \psi_{1:T}^{1:n-1}\right) = \frac{1}{2}\left(\log|M_t^{n+}| - \log|M_t^{n-}|\right). \tag{2.12}$$

The information matrices can be computed sequentially from an initial information matrix $M_0 = P_0^{-1}$ using Kalman filter and Kalman smoother equations [50]. The Kalman smoother equations are needed because the measurement set includes measurements from future times, i.e. to properly include $\psi_{1:T}^{1:n-1}$. However, it will be shown in Section 3.1.1 that computing a different form of the mutual information that does not require a smoother results in the same optimal trajectory.

2.2 Specific Models

This section defines the specific models used throughout both the simulation work and the flight experiments. These models are used in the computation of the utility function. Note that the planning algorithms are not limited to these specific models.

2.2.1 Communication

Two communication schemes are considered for this work direct and multi-hop. Direct communication assumes that each aircraft communicates directly with the fusion center. The multi-hop scheme allows for communications to hop through the other aircraft to the fusion center. For the work in this thesis both of these schemes model each individual link as a packet erasure channel based on empirical data.

2.2.1.1 Empirical Link Model

The communication link model was based on empirical data gathered in experiments between 2 unmanned aircraft along with an unmanned aircraft described in Section 4.2 communicating with the base station where the wireless communication is the 802.11 protocol at 2.4GHz based on Atheros WiFi cards. Figure 2.5 is a plot of this data. This data was based on 21 flight experiments on 6 different days between 2013-03-22 and 2013-06-07. The hardware utilized for these experiments is described in detail in Section 4.2 with the following summarized parameters:

- UDP Transmission
- Messages sent at 1Hz
- 40 byte packets
- 802.11b Ad-hoc protocol
- B.A.T.M.A.N. advanced routing protocol (version 2012.1)
- Atheros Mini-PCI Express hardware
- 63mW transmit power

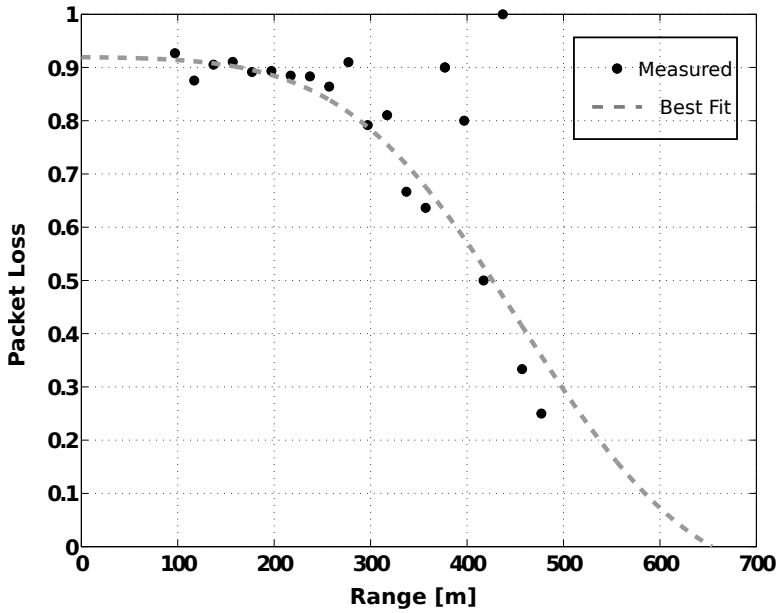

Figure 2.5: Packet Loss versus Range data based on experimental data.

- Omni-directional antennas

The fit to this function is the *erfc* function that was fit using least squares with the resulting function:

$$\beta_t^{i,j}(\mathbf{s}_t^i, \mathbf{s}_t^j) = .5 * \text{erfc}\left(\frac{\|\mathbf{s}_t^i - \mathbf{s}_t^j\| - 461}{195}\right) - 0.085 \tag{2.13}$$

where $\beta_t^{i,j}(\mathbf{s}_t^i, \mathbf{s}_t^j)$ is the link probability of a direct transmission between nodes i and j. This function is utilized as the individual link model for the utility function and is assumed independent of the number of links for the experiments flown.

2.2.1.2 Direct Communication

The direct communication model is where the sensor fusion is done at a ground station and each vehicle has a direct communication link to the station as shown in Figure 2.6. The direct communication case assumes that the vehicles are connected to each other through the ground station. In this case the packet erasure model described in Equation 2.4 is:

$$\begin{aligned} \text{Prob}(\mathbf{z}_t^n = \mathbf{y}_t^n) &= \beta_t^n(\mathbf{s}_t^n) \\ \text{Prob}(\mathbf{z}_t^n = \emptyset) &= 1 - \beta_t^n(\mathbf{s}_t^n) \end{aligned} \tag{2.14}$$

where the term $\beta_t^n(\mathbf{s}_t^n)$ for vehicle n is only a function of it's own sensor state $\mathbf{s}_t^n$ at time t and the value is drawn from the empirical link model in Equation 2.13.

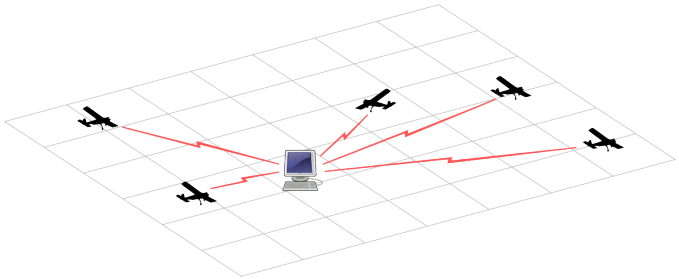

Figure 2.6: Overview of direct communication.

2.2.1.3 Multi-hop Communication

The multi-hop communication scheme allows aircraft to take advantage of other aircraft in the network as relay nodes as shown in Figure 2.7. Multi-hop communication has the potential to improve the performance of the network by increasing the coverage area. As in the direct communication scheme, multi-hop communication models an individual link with the empirical model so that the probability of a successful transmission from vehicle i to j at time t is $\beta_t^{i,j}(\mathbf{s}_t)$. Note that this individual link probability is assumed to be only a function of the positions of vehicles i and j, i.e. there is the assumption of no interference from the other vehicles and the value is taken from Equation 2.13.

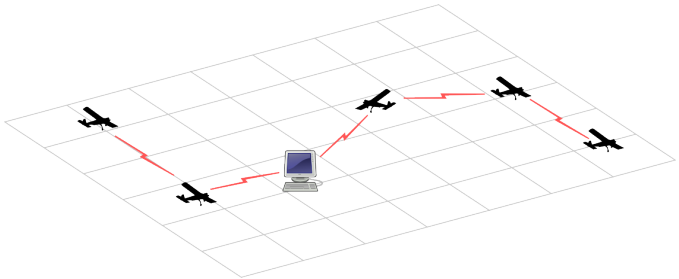

Figure 2.7: Overview of multi-hop communication

To model the probability of the entire multi-hop chain, we use the total probability over all of the

possible routes the message could take from the transmitting vehicle n to the fusion center b:

$$\beta_t^n(\mathbf{s}_t) = \sum_{\text{all routes n}\to\text{b}} p\left(\text{success}|\text{route}_k\right) p\left(\text{route}_k\right) \tag{2.15}$$

Where $p\left(\text{success}|\text{route}_k\right)$ is the probability of the packet reaching the fusion center given that it takes a specific route k. Since we assume each link is independent, this can be written as:

$$p\left(\text{success}|\text{route}_k\right) = \prod_{(i,j)\in\text{route}_k} \beta_t^{i,j}(\mathbf{s}_t) \tag{2.16}$$

The term $p\left(\text{route}_k\right)$ is the probability of the route k being chosen, which will depend on the implementation of the routing algorithm chosen. For the remainder of this dissertation the assumption is made that the algorithm will always choose the route with the highest probability of a successful transmission:

$$\text{route}_k^* = \arg\max_{\text{route}_k} \left[\prod_{(i,j)\in\text{route}_k} \beta_t^{i,j}(\mathbf{s}_t) \right] \tag{2.17}$$

This results in a simplified calculation for the probability of a successful transmission:

$$\beta_t^n(\mathbf{s}_t) = p\left(\text{success}|\text{route}_k^*\right) \tag{2.18}$$

2.2.2 Sensing

In this work, two different sensing problems are considered to evaluate the algorithms. The first of these looked at utilizing RF signal strength as a range measurement to localize ground targets. For the experimental work both 2.4GHz and 433MHz RF emitters were utilized. The second sensing problem involves localizing moving ground targets using bearings-only measurements. The following sub-section describes both the state and measurement equations for both of these classes of sensing problems.

2.2.2.1 Stationary RF Emitters

Localizing stationary RF emitters is based on measuring the signal power at the sensing aircraft. The signal power $P_{p,s}$ received at the sensor location, $\mathbf{s_t}$ at time t, from an emitter at location $\mathbf{p}_t = [x_t \; y_t]^T$ can be described by the empirical path loss model [32]

$$P_{p,s} = P_0 \left(\frac{d_0}{\|\mathbf{p}_t - \mathbf{s}_t\|} \right)^{\alpha} G_{p,s} \tag{2.19}$$

where P_0 and d_0 are reference power and reference distances, and α is the path loss exponent or the propagation decay exponent which is typically restricted to $2 \leq \alpha \leq 6$ depending on environmental factors like atmospheric conditions and the objects present in the environment. Received signal power is often expressed in decibels as

$$P_{p,s}^{db} = \kappa - \alpha 10 \log_{10} \left(\|\mathbf{p}_t - \mathbf{s}_t\| \right) + \nu \tag{2.20}$$

where $\kappa = 10 \log_{10} P_0 d_0^{\alpha}$ and $\nu = 10 \log_{10} G_{p,s}$ is an additive noise term. Various fading channel models can be used to describe ν, depending on the environment. The simplest form is to use additive white Gaussian noise (AWGN). A Rayleigh or Rician distribution can also be utilized for certain types of channels [49]. Figure 2.8 shows $P_{p,s}^{db}$ data gathered using the NexSTAR UAS [39] over two flight days from four different sources. A least squares fit was performed on this data to calculate values $\alpha = 3.48$ and $\kappa = 10.61$.

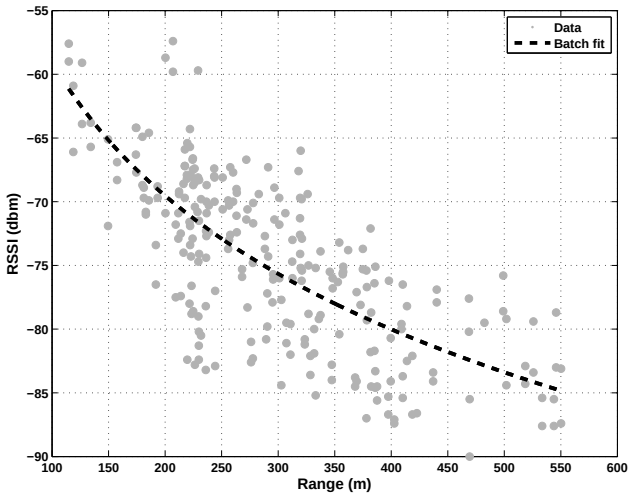

Figure 2.8: RSSI data gathered on July 12, 2011

This work uses a discrete time formulation for the emitter dynamics and measurement equations. For this work, only stationary emitters are considered. The radio parameters κ and α are affected by the environment and can change over the course of a day, so they are included in the system state. Thus, for

static emitters the state $\mathbf{x_t}$ at discrete time t is as follows:

$$\mathbf{x_t} = \begin{bmatrix} x_t \\ y_t \\ \kappa_t \\ \alpha_t \end{bmatrix} \tag{2.21}$$

The received signal power is a function of receiver position which is treated as the input to the system, i.e. $\mathbf{u_t} = \mathbf{s_t} = [\mathbf{x_s}, \mathbf{y_s}]^{\mathbf{T}}$.

The state equations include process noise terms to prevent filter saturation and provide flexibility in filter design and tuning. A linear state update equation with process noise $\mathbf{w_k}$ is assumed so that

$$\mathbf{x}_{t+1} = \mathbf{f}_x(\mathbf{x}_t, \mathbf{u}_t, \mathbf{w}_t) = \mathbf{x}_t + \mathbf{w}_t \tag{2.22}$$

For this work RSSI measurement provides received power in decibels, so the measurement equation is:

$$\begin{aligned} y_t &= P_{t,r}^{db} = h(\mathbf{x}_t, \mathbf{u}_t, v_t) \\ &= \kappa_t + 10\alpha_t \log_{10} \|(x_t, y_t) - (x_{s,t}, y_{s,t})\| + v_t \end{aligned} \tag{2.23}$$

where the measurement noise v_t is assumed to be Gaussian.

2.2.2.2 Bearings-only Tracking of Moving Targets

The second sensing problem involves UAS localizing moving ground targets using bearings-only measurements. The state, dynamics, and measurement functions for this problem are defined as:

$$\mathbf{x}_t = \begin{bmatrix} x_t \\ y_t \\ v_{x,t} \\ v_{y,t} \end{bmatrix} \tag{2.24}$$

$$\mathbf{x}_{t+1} = \mathbf{f}_x(\mathbf{x}_k, \mathbf{w}_t) = \begin{bmatrix} \mathbf{x}_t(1) + \Delta t \cdot \mathbf{x}_t(3) + \mathbf{w}_t(1) \\ \mathbf{x}_t(2) + \Delta t \cdot \mathbf{x}_t(4) + \mathbf{w}_t(2) \\ \mathbf{x}_t(3) + \mathbf{w}_t(3) \\ \mathbf{x}_t(4) + \mathbf{w}_t(4) \end{bmatrix} \tag{2.25}$$

$$y_t = \theta_t = h(\mathbf{x}_t, \mathbf{s}_t, \mathbf{v}_t) = \tan^{-1}\left(\frac{\mathbf{x}_t(2) - \mathbf{s}_t(2)}{\mathbf{x}_t(1) - \mathbf{s}_t(1)}\right) + v_t \tag{2.26}$$

where θ_t is the bearing angle from the sensor to the emitter, $v_{x,t}$ and $v_{y,t}$ are the velocity components of the targets, $\mathbf{w}_t(1) = \mathbf{w}_t(2) = 1m$ and $\mathbf{w}_t(3) = \mathbf{w}_t(4) = 0.1m/s$ are the process noises for the position, and velocity respectively and the measurement noise v_t is a zero-mean gaussian noise with a standard deviation of 10^o.

2.2.3 Vehicle

In this work the sensor state, radio state, and aircraft state are all the same variable $\mathbf{s}_t$. The control of sensors/radio is modelled as a small UAS under autopilot control. It is assume that an autopilot provides low level control to the aircraft that is flying at a fixed altitude and airspeed, v_0. The only input into the aircraft is the turn rate, u_t, that controls the trajectory of the aircraft. The dynamic equation for a given time step Δt is the exact solution to the continuous unicycle kinematic model with constant turn rate:

$$\mathbf{s}_{t+1} = f_s(\mathbf{s}_t, \mathbf{u}_t) = \begin{bmatrix} x_{s,t+1} \\ y_{s,t+1} \\ z_{s,t+1} \\ \psi_{s,t+1} \end{bmatrix} \tag{2.27}$$

$$= \begin{bmatrix} x_{s,t} + v_0 \cdot \mathrm{sinc}\left(\frac{1}{2}u_t\Delta t\right)\cos\left(\psi_{s,t} + \frac{1}{2}u_t\Delta t\right)\cdot\Delta t \\ y_{s,t} + v_0 \cdot \mathrm{sinc}\left(\frac{1}{2}u_t\Delta t\right)\sin\left(\psi_{s,t} + \frac{1}{2}u_t\Delta t\right)\cdot\Delta t \\ z_{s,t} \\ \psi_{s,t} + \Delta t \cdot u_t \end{bmatrix}$$

for $|u_t| \leq \omega_{max}$ and where (x_s, y_s, z_s) is the 3D position of the aircraft, ψ_s is the heading angle relative to North, and $\mathrm{sinc}(x)$ is the sine cardinal function.

$$\mathrm{sinc}(x) = \begin{cases} \frac{\sin(x)}{x} & x \neq 0 \\ 1 & x = 0 \end{cases} \tag{2.28}$$

Chapter 3

Distributed Information Gathering Optimization Algorithm

This chapter examines the problem of distributed path planning for a mobile sensor network comprised of communication-aware robots performing general information gathering missions. Mutual information is used to compute utility functions that are optimized locally by each robot. Each robot computes the control input in a distributed manner that results in a combined action that can be bounded by the optimal centralized result utilizing submodularity in certain cases. It is shown that when the communication model includes multi-hop communication to expand the coverage of the sensor network, the property of submodularity is lost. The algorithms are evaluated in simulation by application to bearings-only tracking and to tracking an RF emitter based on signal strength with multiple aircraft and targets.

3.1 Planning

The overall objective of this work can now be defined. The control inputs $\mathbf{u}_t^n$ drive the sensor states $\mathbf{s}_t^n$ which in turn determine the measurements $\mathbf{z}_t^n(\mathbf{s}_t^n)$ and the information contained in them, where this dependence on the sensor state was dropped in the discussion of the previous section. In particular, the sensor state explicitly enters calculation of the erasure channel probabilities $\beta_t^n(\mathbf{s}_t^n)$ and the Jacobians of the measurement equations $H_{n,t+1}(\mathbf{s}_t^n) = \nabla_{\mathbf{x}} h_n\left(\mu_t, \mathbf{s}_{n,t}, 0\right)$.

Let the input vector over the planning horizon be $\mathbf{u} = \{\mathbf{u}_1, \cdots, \mathbf{u}_T\}$ and the sensor state vector over the planning horizon be $S_T = \{\mathbf{s}_1, \cdots, \mathbf{s}_T\}$. The global problem of interest here is:

Problem 1 (Maximize Mutual Information)

$$\begin{aligned} \textbf{maximize} \quad & J_1(\mathbf{u}) = I(X_T, Z_T(S_T(\mathbf{u}))) \\ \textbf{subject to} \quad & \mathbf{u}_t \in U_t, \quad \forall t \in [1, \cdots, T] \\ & \mathbf{s}_{t+1} = f_s(\mathbf{s}_t, \mathbf{u}_t). \end{aligned} \tag{3.1}$$

For a candidate input $\mathbf{u}$ the cost function $J_1(\mathbf{u}) = I(X_T, Z_T(S_T(\mathbf{u})))$ can be solved numerically since $2^{|B_i|}$ is a finite set. However, it requires a summation over the entire power set which has $2^{|B_i|} = 2^{T \cdot N}$ elements (Equation 2.7). An approximation is desired that can yield good measurements when optimized, but at reduced computational cost. This need motivates the introduction of a modified measurement model. In particular, assume the fusion center receives the expected amount of information per measurement, which is realized by assuming the sensor noise covariance has its expected value. In other words, define and use the new measurement set $\tilde{Y}_i$ with modified noise covariances $\tilde{R}_{n,t}^{-1} = E\{b_t^n R_{n,t}^{-1}\} = \beta_t^n R_{n,t}^{-1}$. The new modified information measure can now be expressed as the mutual information $I(X_T; \tilde{Y}_T)$ between the states and the new measurement set. This leads to a new problem statement:

Problem 2 (Maximize Modified Mutual Information)

$$\begin{aligned} \textbf{maximize} \quad & J_2(\mathbf{u}) = I(X_T, \tilde{Y}_T(S_T(\mathbf{u}))) \\ \textbf{subject to} \quad & \mathbf{u}_t \in U_t, \quad \forall t \in [1, \cdots, T] \\ & \mathbf{s}_{t+1} = f_s(\mathbf{s}_t, \mathbf{u}_t). \end{aligned} \tag{3.2}$$

3.1.1 Distributed Optimization

This work considers distributed planning algorithms across the sensor network. The distribution is done over a pre-defined order that comes from the first line of Equation 2.6, i.e. vehicle n plans its path given the paths of the previous $n-1$ vehicles and then sends the plan to vehicle $n+1$. Previous work has looked at applying the chain rule over time first instead of the vehicles [56, 22]. The major disadvantage of splitting the mutual information by vehicles first instead of time is that we now have measurements from future times in the term $\mathbf{z}_{1:T}^{1:n-1}$.

This term complicates calculation of the information filter at each step, e.g. by running the Kalman information filter equations forward to time T processing all of the measurements in $\{\mathbf{z}_t^n, \mathbf{z}_{1:t-1}^n, \mathbf{z}_{1:t}^{1:n-1}\}$ and

then running a Kalman Smoother [50] back to time t to process $\{\mathbf{z}_{t+1:T}^{1:n-1}\}$. To avoid each vehicle having to do this complex calculation, each robot solves a different local optimization that provides the same result with less computation. In particular, each robot takes advantage of the fact that:

$$\arg\max_{\mathbf{z}_{1:\,T}^{n}} I\left(X_T; \mathbf{z}_{1:\,T}^{n} | \mathbf{z}_{1:T}^{1:n-1}\right) = \arg\max_{\mathbf{z}_{1:\,T}^{n}} I\left(X_T; \mathbf{z}_{1:T}^{1:n}\right) \tag{3.3}$$

which is derived as follows:

$$\begin{aligned}
\mathbf{z}_{1:\,T}^{n*} &= \arg\max_{\mathbf{z}_{1:\,T}^{n}} I\left(X_T; \mathbf{z}_{1:\,T}^{n} | \mathbf{z}_{1:T}^{1:n-1}\right) \\
&= \arg\max_{\mathbf{z}_{1:\,T}^{n}} \left[H\left(X_T | \mathbf{z}_{1:T}^{1:n-1}\right) - H\left(X_T | \mathbf{z}_{1:T}^{1:n-1}, \mathbf{z}_{1:\,T}^{n}\right)\right] \\
&= \arg\max_{\mathbf{z}_{1:\,T}^{n}} \left[-H\left(X_T | \mathbf{z}_{1:T}^{1:n}\right)\right] \\
&= \arg\max_{\mathbf{z}_{1:\,T}^{n}} \left[H(X_T) - H\left(X_T | \mathbf{z}_{1:T}^{1:n}\right)\right] \\
&= \arg\max_{\mathbf{z}_{1:\,T}^{n}} I\left(X_T; \mathbf{z}_{1:T}^{1:n}\right)
\end{aligned} \tag{3.4}$$

This holds because both $H\left(X_T | \mathbf{z}_T^{n-1}\right)$ and $H\left(X_T\right)$ are constant with respect to $\mathbf{z}_{1:\,T}^{n}$. The utility function for a given $\mathbf{z}_{1:\,T}^{n}$ is computed by using the version of Equation 2.6 that performs the chain rule over time first. This results in the entire calculation moving forward in time and not having to use the smoother at each step. This is shown graphically in Figure 3.1 comparing processing the measurements across time first instead of vehicles. This allows us to reformulate the modified optimization problem with a new *local*

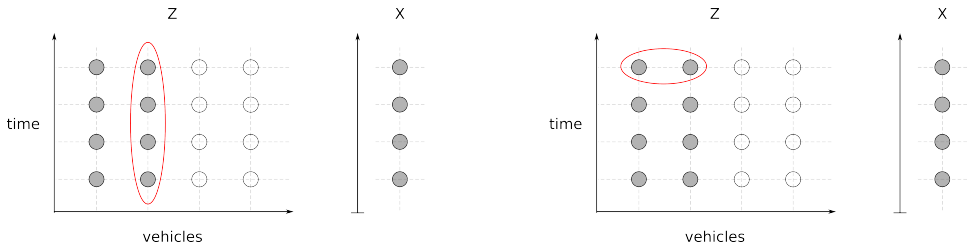

Figure 3.1: Graphical comparison of the two forms of the chain rule.

optimization objective $J_3^n(\mathbf{u_n})$ such that each robot solve:

Problem 3 (Maximize Distributed Modified Mutual Information)

$$\begin{aligned} \textbf{maximize} \quad & J_3^n(\mathbf{u_T^n}) = I(X_T, \tilde{\mathbf{y}}_{1:T}^n(S_T^n(\mathbf{u}_T^n))|\tilde{Y}_T^{n-1}) \\ & \forall\ n \in \{1, \ldots, N\} \\ \textbf{subject to} \quad & \mathbf{u}_t^n \in U_t^n, \quad \forall t \in [1, \cdots, T] \\ & \mathbf{s}_{t+1}^n = f_s^n\left(\mathbf{s}_t^n, \mathbf{u}_t^n\right) \end{aligned} \tag{3.5}$$

3.2 Performance Bounds

The goal of this section is to establish bounds for distributed optimization of Problem 3 against solving the centralized Problem 2. The discussion that follows will focus on selection of the control inputs $\mathbf{u}$ with the understanding that these lead to the measurements used in the calculation of the mutual information. The input vector for each sensor over the planning horizon will be denoted $\mathbf{u}^n = \{\mathbf{u}_1^n, \cdots, \mathbf{u}_T^n\}$ so that the total input vector can also be expressed as $\mathbf{u} = \{\mathbf{u}^1, \cdots, \mathbf{u}^n\}$. Let $U = U_1 \times U_2 \times \cdots \times U_N$ be the set of admissible control input sequences where U_n is the control set for sensor n. The optimal input is defined as:

$$\mathbf{u}^* = \arg\max_{\mathbf{u} \in U} J\left(\mathbf{u}\right) \tag{3.6}$$

with $J^* = J\left(\mathbf{u}^*\right)$.

When discussing distributed optimization, it is also helpful to take a set-theoretic perspective of the optimization process. Under this perspective, let the objective be represented as a function over the set of sensors S, denoted by $J(S)$ which is understood to be equivalent to $J(\mathbf{u})$. Further, if $E \subset S$ is a subset of sensors, e.g. $E = \{1, 3, n+1, N\}$, then $J(E)$ is understood to be the cost computed just from those sensors, e.g. $J(E) = J([\mathbf{u}^1, \mathbf{u}^3, \mathbf{u}^{n+1}, \mathbf{u}^N]')$. Let $\{n\}$ represent the set that only contains the n^{th} sensor, let $S_{<n} = \{1, 2, \cdots, n-1\}$ be the set of all sensors with label less than n, and let $S_{-n} = S \setminus n = \{1, 2, \cdots n-1, n+1, \cdots N\}$ be the set of all sensors except n. Then the objective function can be rewritten.

$$J(\mathbf{u}) = J(S) = \sum_{n=1}^{N} J^n\left(\{n\}, S_{<n}\right). \tag{3.7}$$

3.2.1 Direct Communication Assessment

The direct communication model assumes that the vehicles are connected to each other through the ground station and transmit both their planned trajectories and the measurements they take. Some known results for sequential distributed optimization of mutual information will be presented. Recall from Equation 2.14 that the term $\beta_t^n(\mathbf{s}_t^n)$ for vehicle n is only a function of it's own sensor state $\mathbf{s}_t^n$ at time t. This results in a form of the utility function that is submodular since each sensor contribution is independent conditioned on the state[56].

The decomposition of the objective function in Equation 2.6 motivates a sequential distributed optimization approach whereby each sensor optimizes a local function given the control inputs of the sensors with smaller labels. These labels can also be viewed as an ordering or prioritization, so the approach is referred to as hierarchical. In particular, each sensor solves the following equation.

$$\begin{aligned}\mathbf{u}^{n,h} &= \arg\max_{\mathbf{u}_n \in U_n} J^n(\mathbf{u}_n, \mathbf{u}^{1:n-1,h}) \\ &= \arg\max_{\mathbf{u}_n \in U_n} J^n(\{n\}, S^h_{<n}).\end{aligned} \tag{3.8}$$

In general, distributed hierarchical optimization as described in Equation 3.8 has guaranteed performance bounds when the objective function is non-decreasing (adding more members to the input set never decreases the cost) and submodular [28]. Submodularity is a diminishing returns property whereby the incremental value of adding another input is larger if added to a smaller set. Formally, define the marginal return or incremental cost of adding j to set E as $\rho_j(E) = J(\{j\} \cup E) - J(E)$. A set-valued function $J(E)$ is submodular if the following is true.

$$\rho_j(E_2) \geq \rho_j(E_1), \quad \forall E_2 \subseteq E_1 \subseteq E \quad \text{and} \quad j \in E - E_1. \tag{3.9}$$

It has been shown that mutual information between the state sequence X_T and a set of observations is submodular when the observations are independent of each other conditioned on the state [56]. This is the case with direct communication since the control inputs (hence sensor state and information content) achievable by one sensor are not limited by the actions of the other sensors.

Let $\mathbf{u}^h = [\mathbf{u}^{1,h}, \cdots, \mathbf{u}^{N,h}]'$ be the global control input vector that results from the distributed optimization with $J^h = J(\mathbf{u}^h)$ being the resulting utility. Because the mutual information is non-decreasing and

submodular for direct communication, the result from the hierarchical distributed approach will be no worse than half of the global optimal solution, i.e. $\frac{1}{2}J^* \leq J^h \leq J^*$.

A proof of this result is given in Appendix A.1. Having this guaranteed lower bound insures that the hierarchical approach will never produce arbitrarily bad results compared to the global optimal solution.

Implementation of the hierarchical approach trades optimality for communication overhead. The overall communication overhead scales linearly in the number of sensors as each sensor requires knowledge of one more control input than the previous (higher priority) sensor. Control inputs could be disseminated from each sensor to all the sensors that will eventually need it through a broadcast method, or each successive sensor could receive the previous control inputs, add its own, and then forward the information to the next sensor. This procedure could be realized through a token ring protocol. The distributed optimization procedure converges to a result after each vehicle performs its local optimization once, eliminating the need to iterate multiple times.

A special case of direct communication is the perfect communication assumption. Under perfect communication, Problem 1 and Problem 2 are identical. The perfect communication assumption holds in certain scenarios where either the vehicles are in an area where they will always be close to each other relative to their maximum communication range, or they are using a communication scheme that does not have range limitations such as satellite.

3.2.2 Multi-hop Communication Assessment

The communication model will now be expanded to allow multi-hop communication. The probability of each message getting through the network was derived in Equation 2.18 where each probability was potentially a function of the positions of every aircraft in the network. This communication model results in a utility function that in general loses the submodularity property due to the loss of independence between the measurements since the trajectory of one aircraft can affect the $\beta_t^n(\mathbf{s}_t)$ terms by acting as a relay. The following illustration is a counter-example scenario which shows where submodularity fails.

The example scenario in Figure 3.2 is for one step look-ahead planning for a target with position x_t and prior information M^- being observed by sensors measuring the 1-D position of the target with some

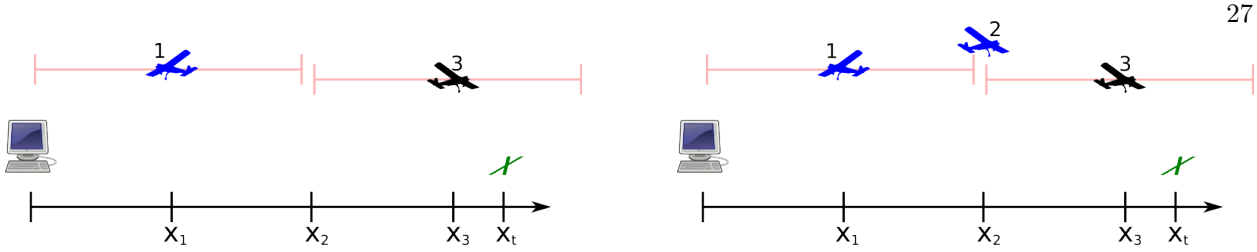

Figure 3.2: Example showing submodularity breaking down since (a) no information is gained with two robots but (b) some information is gained when a third completes the multi-hop chain.

information contribution I^j. The sensor positions given as x_1, x_2, and x_3 and the communication is based on the disc model with:

$$\beta^{i,j} = \begin{cases} 1 & r_{i,j} \leq r_0 \\ 0 & r_{i,j} > r_0 \end{cases} \tag{3.10}$$

where $r_{i,j}$ the distance between sensor i and j. In this example $r_{b,1} = r_{1,2} = r_{2,3} = r_0$ and therefore $r_{1,3} = 2r_0$. Also, since the state space is 1-D, the variables in the cost function are scalars with the utility defined as:

$$J(A) = \log \left| M^- + \sum_{j \in A} \beta^j I^j \right| \tag{3.11}$$

We define the sets $S = \{1\}$, $T = \{1, 2\}$, $j = \{3\}$. For submodularity to hold the relationship must be true.

$$\rho_j(S) \geq \rho_j(T), \ \forall \ S \in T \tag{3.12}$$

Where $\rho_j(S) = J(j \cup S) - J(S)$. In the example scenario in Figure 3.2(a) the function is written as:

$$\begin{aligned} \rho_j(S) &= J\left(\{3,1\}\right) - J\left(\{1\}\right) \\ &= \log\left[M^- + \beta^1 I^1 + \beta^3 I^3\right] - \log\left[M^- + \beta^1 I^1\right] \\ &= 0 \end{aligned} \tag{3.13}$$

Since $\beta_3 = 0$ because vehicle 3 is outside of communication range from vehicle 1 (and hence the base) without

vehicle 2 acting as a relay. In Figure 3.2(b) the function is written as:

$$\begin{aligned}\rho_j(T) &= J(\{3,1,2\}) - J(\{1,2\}) \\ &= \log\left[M^- + \beta^1 I^1 + \beta^2 I^2 + \beta^3 I^3\right] - \log\left[M^- + \beta^1 I^1 + \beta^2 I^2\right] \\ &= \log\left[M^- + I^1 + I^2 + I^3\right] - \log\left[M^- + I^1 + I^2\right] \\ &> 0\end{aligned} \tag{3.14}$$

Which implies that $\rho_j(S) < \rho_j(T)$, which violates submodularity.

3.3 Monte Carlo Simulations

The purpose of this section is to assess the algorithms presented in this chapter. All of the scenarios utilized in the simulations will involve unmanned aircraft systems (UAS) localizing and tracking ground targets. The sensing, communication, and vehicle models utilized in this section can be found in Section 2.2. The Monte Carlo simulations below consider two different sensing problems localization of RF emitters using RSSI and bearings-only tracking of moving targets.

3.3.1 Modified Mutual Information

The exact mutual information from Problem 1 is compared against the modified mutual information from Problem 2, specifically looking at the direct communication case. A numerical comparison is run between Problem 1 and Problem 2 to show how close the resulting solution is for both formulations. The set of 100 different initial positions, (x, y), shown in Figure 3.3 was run to compare the formulations. The truth value for κ and α are 11.5 and 3.5 respectively and the measurement noise v_t is zero-mean Gaussian noise with a standard deviation of 2.9, and these values are all based on empirical data [48]. The scenario involves localizing 3 stationary RF radio sources by 3 UA as described in Equations 2.21, 2.22, and 2.23. Since the computational complexity of computing Problem 1 grows with $2^{N \cdot T}$ each run was only for 3 time steps across the 3 vehicles. The value of the cost functions resulting from Problem 1 and Problem 2 are examined in Figure 3.4 for one set of initial conditions (the red numbers in Figure 3.3) shown in Figure 3.3. This plot shows for this one example that the solution to Problem 2 maps exactly to the optimal solution of Problem 1. Figure 3.4 spans over a discrete range of the admissible inputs for 3 vehicles over 3 time

steps (9 dimensional) that are mapped into the x-axis. The plot of the utility of the full mutual information calculation (Problem 1) is sorted from lowest to highest, and this same ordering is applied to the results of the utility from the modified mutual information, Problem 2. Note that what appears to be a constant offset between the two solutions has some variation and was not expected.

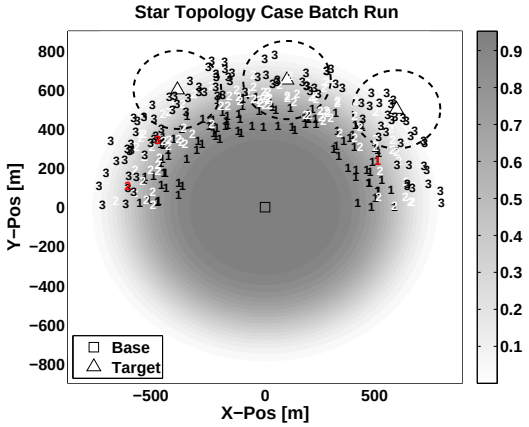

Figure 3.3: The Initial Conditions for the batch runs for the comparison of Problem 1 vs. Problem 2

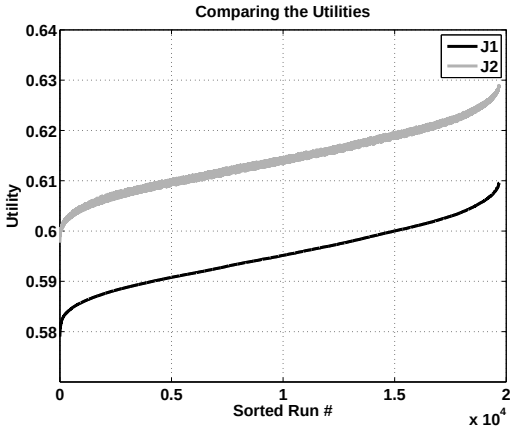

Figure 3.4: Comparing the value of the utility functions over the entire range of control inputs. Note, since this case has 9 degrees of freedom the x-axis is the run number where the entire set of possible inputs is discretized.

Next we examine the entire batch of 100 runs for Problem 1 vs. Problem 2 shown in Figure 3.3. The vehicles were purposefully placed in the region where communication dropouts are frequent to best illustrate the differences between Problem 1 and Problem 2 since they differ in how they factor in the communication model. Figure 3.5 contains a numerical comparison between the solutions to Problem 1 and 2 for the batch

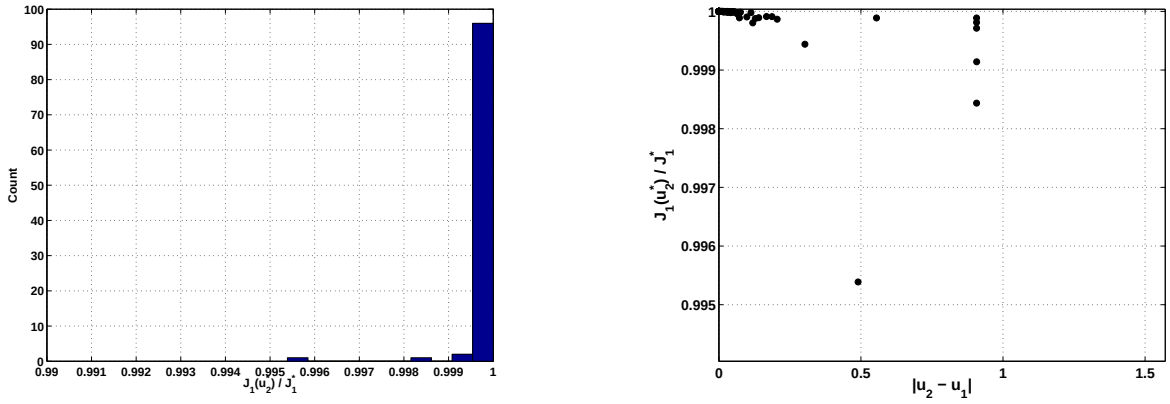

(a) (b)

Figure 3.5: (a) Histogram showing how $J_1(u_2^*)$ compares to J_1^* and (b) a comparison of how $\frac{J_1(u_2^*)}{J_1^*}$ compares against the difference in the control variables $|u_1^* - u_2^*|$.

of cases shown in Figure 3.3. Figure 3.5(a) contains a histogram showing $J_1(u_2^*)/J_1^*$, which is the mutual information cost of Problem 1 evaluated for the optimal solution u_2^* of the modified mutual information of Problem 2 divided by the optimal solution to Problem 1. In every case for this set of example scenarios the solution to the modified mutual information was within 99% of the optimal value of the full mutual information reinforcing the validity of using Problem 2. Figure 3.5(b) looks at this difference as a function of the difference in the control variable u. Note that the span of the y-axis is between 0.995 and 1.0 of the optimal. Also, the majority of final control inputs were very similar between both formulations of the mutual information. This further enforces the validity of using the much more computationally tractable modified mutual information solution contained in Problem 2.

If the $\beta_t^n(\mathbf{s}_t^n)$ terms are independent of each other, meaning that the communicating vehicles do not interfere with each other, then the measurements are independent of one another conditioned on the state, the modified mutual information utility is submodular, and the hierarchical solution to Problem 2 is guaranteed to be no worse than half the centralized optimal solution to Problem 2. The remainder of the comparisons done in this chapter will focus on the modified mutual information formulation in Problem 2.

3.3.2 Comparing Centralized to Distributed Planning

The performance of the distributed algorithm is compared against a centralized solution using 100 test cases that were run for three communication cases; direct communication with no dropouts (essentially $\beta = 1$ always), the direct communication model with packet loss, and the multi-hop communication model. The distribution of the starting positions for these scenarios is shown in Figure 3.6. The figure also shows the motion of the targets for the mission length, note that only two of them move. The simulated cases involved three aircraft performing bearings-only tracking of three moving ground targets whose state is the planar position and velocity as described in Equations 2.24, 2.25, and 2.26. For each type of communication model the aircraft were given the same 100 random starting points and planned a trajectory for the next 60 seconds with the sensors able to take measurements at 1Hz. The optimization was performed by a genetic algorithm.

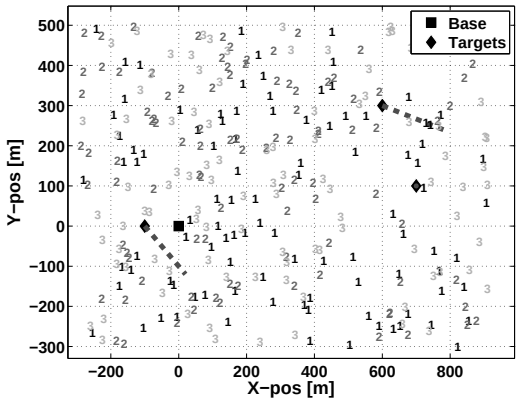

Figure 3.6: Batch Setup

Figure 3.7 is a series of histograms comparing the performance of the distributed hierarchical algorithm against the global optimum. For each random set of initial conditions the value of the utility function of the distributed hierarchical algorithm is calculated as a fraction of the global optimum. For all three cases the algorithm does better than the $\frac{1}{2}$ lower bound, even in the multi-hop case where this bound is not guaranteed. In fact, all 100 of the runs for the perfect communication and the direct communication model using a fixed hierarchy did better than 85% of the global optimum with 90% of the runs for both of these

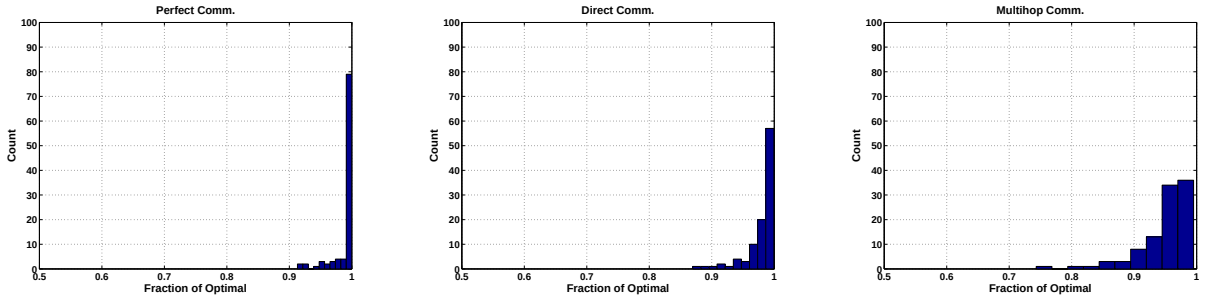

(a) (b) (c)

Figure 3.7: 100 Runs Comparing Hierarchical to Global Optimal (a) Perfect Comm., (b) Direct Comm. (c) Multi-hop Comm.

communication models doing better than 95% of the global optimum.

For the multi-hop case Figure 3.7(c) shows that the hierarchical algorithm still does a good job in many cases with a performance within 70% of the global optimal for all 100 cases. This plot shows that for some sensing problems, even without the guarantees of submodularity we can still expect good performance from the hierarchical algorithm. However there are scenarios where this algorithm will give poor performance.

The following set of batch runs once again involves localizing a stationary RF emitting node using the received signal strength. These test runs were set up specifically for cases where multi-hop communication is needed for good performance. This also results in illustrating scenarios where the hierarchical algorithm will fail to produce good performance. Figure 3.8 shows the problem setup. The top portion of the figure shows where the vehicle's were randomly position to start out, the zones are separated by a distance that still allows some communication. This setup forces the aircraft to form a chain from the aircraft in the zone furthest from the base station using the others as a relay back. Typically the best trajectories for this problem involve 3 of the aircraft forming a communication chain for the aircraft closest to the target which contributes most of the sensing improvement. These sets of aircraft labeled 1 to 4 were then randomly sorted across the zones as seen in the bottom of Figure 3.8. For certain assortments of aircraft this results in poor performance for the hierarchical algorithm. Figure 3.9 shows a histogram comparing the results of the hierarchical planner against the global optimal result. Note the in some cases the hierarchical algorithm resulted in poor performance below 50% of the centralized optimal solution. However, in general most of the

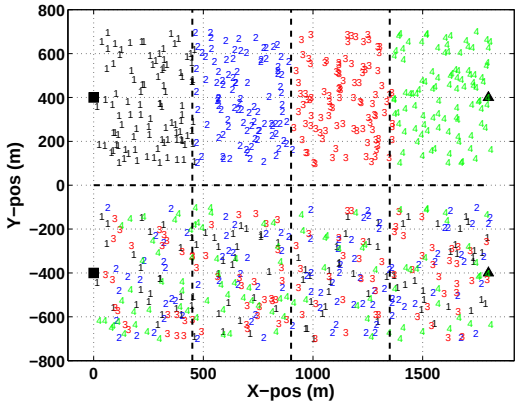

Figure 3.8: Simulation Setup

runs were still above 50%. Figure 3.10 shows the starting positions for both the three best and three worst performances relative to the global optimum. As expected the cases where the vehicles are setup near the best ordering of $1 \rightarrow 2 \rightarrow 3 \rightarrow 4$ the hierarchical comes close to the global optimal, while in the cases where the labelling is in the wrong direction we see poor performance.

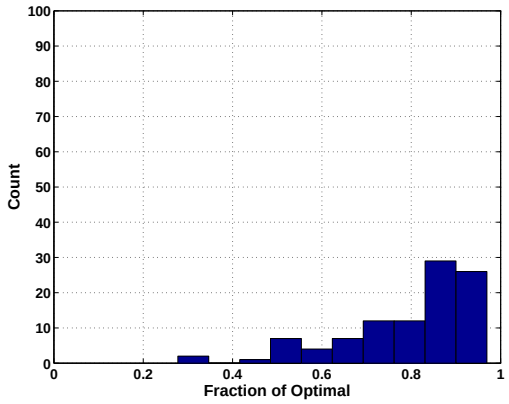

Figure 3.9: Batch runs comparing the fraction of optimal that the hierarchical results

To further show the importance on the ordering for the hierarchical algorithm in the multi-hop communication case two sets of batch runs were simulated, the first with the best possible ordering, $1 \rightarrow 2 \rightarrow 3 \rightarrow 4$, and the worst case ordering of $4 \rightarrow 3 \rightarrow 2 \rightarrow 1$. The resulting histograms are shown in Figure 3.11. These two plots illustrate where the performance of the hierarchical planning can suffer in certain scenarios. However, even in this worst case positioning, that majority of the runs were still above 50% of optimal. For these

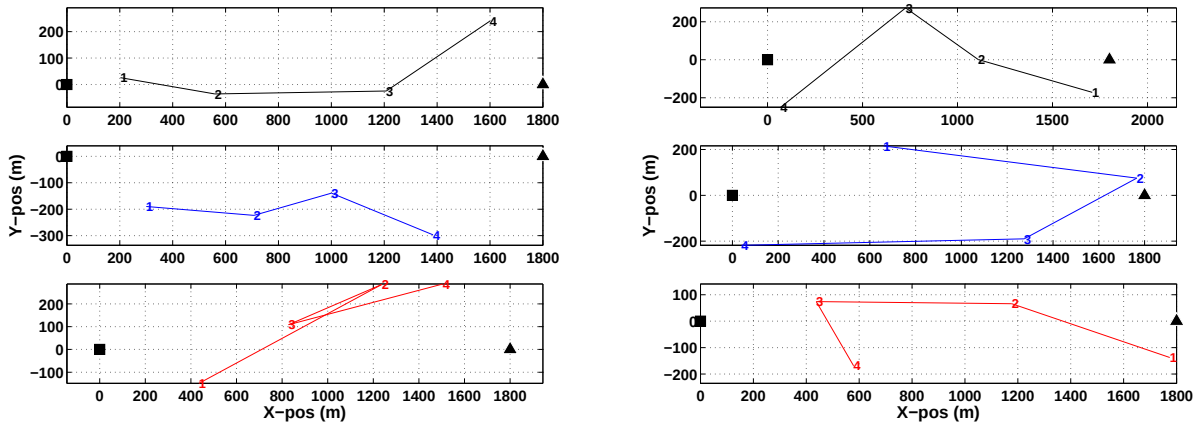

(a) (b)

Figure 3.10: Initial Conditions resulting in the (a) best and (b) worst performance

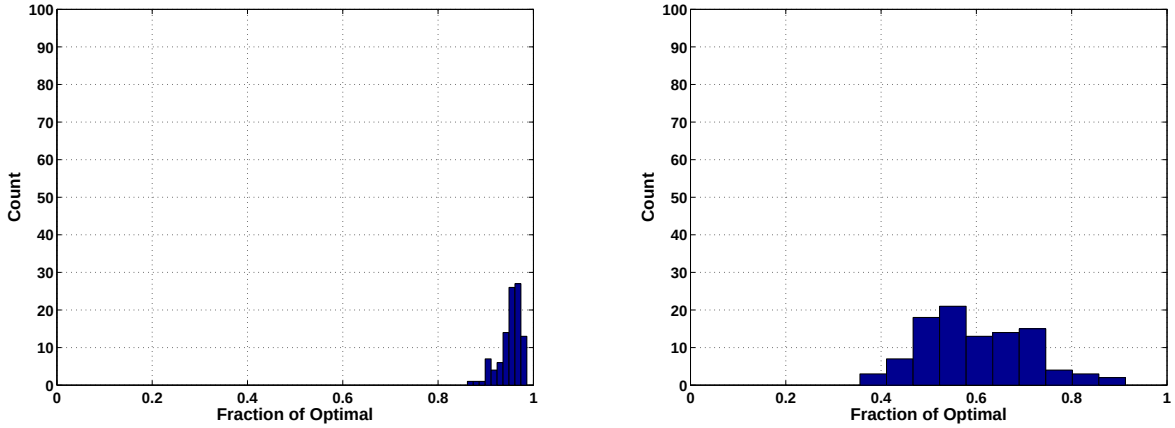

(a) (b)

Figure 3.11: Looking at the fraction of optimal for (a) correct chain and (b) the reverse

types of scenarios heuristics can also be applied such as re-ordering the labels on the vehicles.

3.4 Summary

This chapter examined the problem of distributed path planning for sensor networks composed of vehicles using packet erasure channels for communication. The local utility function used by each vehicle was derived as the local contribution to the mutual information of the entire team. The planning algorithm presented maximized the mutual information in a distributed manner for direct communication model and for systems employing multi-hop communication schemes. A distributed planning algorithm was presented that was submodular for the direct communication scheme and could thus be bounded to within half of the global optimal. It was shown that submodularity breaks down for the multi-hop communication scheme. Over a large batch of runs it was shown that the hierarchical algorithm still has decent performance. Monte Carlo simulations were also employed to examine the sub-optimality of assumptions to make the problem tractable and these simulations showed that the performance was close to the full calculation of mutual information.

Chapter 4

UAS Description

This chapter contains an overview of the hardware and software systems used to perform flight experiments to support the algorithms developed in this dissertation. This system was built on previous work [5, 6]. This work primarily utilized two different UAS, the NexSTAR UAS for WiFi localization, and the multi-aircraft RF sensing UAS comprised of the Tempest UAS and the Skywalker X8 UAS. In this work NexSTAR UAS was used for WiFi localization experiments. Both the Tempest and Skywalker X8 were used for 433MHz localization, communication link modelling, single aircraft path planning, and two aircraft cooperative planning experiments.

4.1 NexSTAR WiFi Sensing UAS

The NexSTAR WiFi sensing UAS shown in Figure 4.1 was utilized for localization of RF beacons at 2.4GHz. The detailed results of those experiments are outlined in Chapter 5. The NexSTAR UAS design has over 100 accumulated flights on three separate airframes.

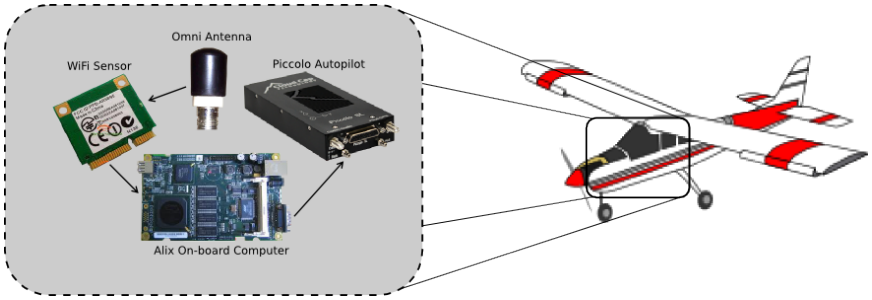

Figure 4.1: NexSTAR WiFi Sensing UAS

Table 4.1: NexSTAR Airframe Specifications

Wingspan	1.75m
GTOW	4.8kg
Motor	Neu 1506 3D
Battery	10Ah 5S Lipo
Endurance	45 minutes
Launch	Catapult

4.1.1 NexSTAR Airframe

The NexSTAR UA was designed for networking and autonomy software prototyping. The airframe is based upon the almost ready-to-fly kit by Hobbico, and was modified to house avionics and payload hardware. This commercial approach provides for a cheap airframe that requires approximately a week to convert to a semi-autonomous airframe (Appendix A in Ref. [6]). A pin was added to the airframe to enable rail launching. The airframe's balsa and monokote construction allows for easy modification and repair. The original NexSTAR UA was changed from a gas engine to an electric motor with approximately 45 minutes endurance, though Hobbico now provides a kit with an electric motor.

4.1.2 Piccolo Avionics System

The NexSTAR UAS utilizes the Piccolo Plus Autopilot [33]. The Piccolo Plus can be commanded either from a ground station through a dedicated 900MHz communication link, or an on-board supervisory computer. The Piccolo Plus autopilot manufactured by Cloud Cap Technology [33] provides UA guidance and control. The sensor suite includes an inertial measuring unit (IMU) with three-axis accelerations and angular rates, GPS position, and an air data system for measuring static and dynamic pressure. The autopilot accepts waypoint commands or provides a simplified kinematic model to higher-level guidance laws. The Piccolo Plus autopilot includes a hardware-in-the-loop simulation capability that allows end-to-end avionics testing in a lab setting. The Piccolo ground station is responsible for managing a direct 900 MHz wireless link to one or more Piccolo avionics, supplying differential GPS corrections, and serving as a bridge to the operator interface. The Piccolo provides a serial interface and software development kit (SDK) to allow an on-board computer to receive telemetry data and issue commands. This capability was used extensively in

this work.

4.1.3 WiFi RSSI Sensing Hardware

For the experiments presented here, the on-board computer is the PC Engines alix3d2 single board computer [38], which runs the experiment and collects data. For the WiFi localization work the alix3d2 was setup running openWRT Backfire [37]. The openWRT framework was also utilized to cross-compile the flight software. The WiFi sensing is done by an Atheros 802.11 mini PCI express card connected to the alix3d2. The Atheros chipset was chosen because it is supported in Linux. Experiments were run using either a regular 2.4GHz dipole antenna and a WiFi-Plus omni antenna [41] with a spherical pattern. The spherical antenna was found to give better measurements since it was less sensitive to orientation changes in the aircraft.

4.1.4 Software Architecture

The NexSTAR WiFi sensing UAS used a specific implementation of the NetUAS [7] system. In this work several new features and modules were added to the NetUAS system including a general UKF formulation, a turn-rate controller based on bank angle for the Piccolo Plus interface, an optimization class based on Covariance Matrix Adaptation Evolution Strategy (CMA-ES)[17], and several smaller parts to allow the localization part.

4.2 Multi-aircraft RF Sensing

The multi-aircraft RF sensing system shown in Figure 4.2 was designed specifically for controlled experiments with RF localization, and multi-UA experiments involving both sensing and communication. This built on the work from the NexSTAR WiFi sensing system.

4.2.1 Airframes

The Tempest Unmanned Aircraft is primarily fiberglass with carbon-fiber composite for reinforcement in the wing spar and the lower surface of the wing [27]. Detachable wings have a span of 3.2m with a gross

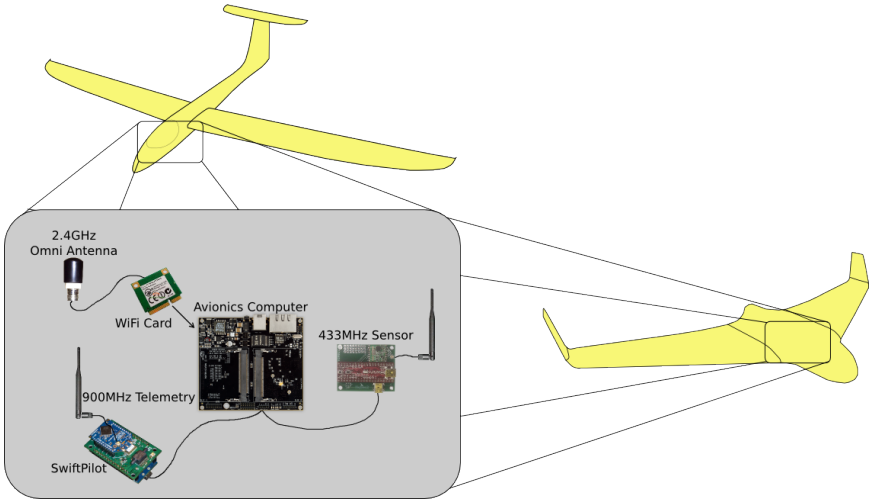

Figure 4.2: Overview of the multi-aircraft RF sensing system

take-off weight of 5.4kg. A smooth under surface and a folding propeller enables landing in grassy fields and road surfaces with no landing gear. The Tempest utilizes an in-runner electric motor with a gearbox manufactured by Neu Motors, a Castle Creations ICE speed control, a Graupner propeller, and a 11,000 mAh lithium polymer battery manufactured by MaxAmps providing endurance of approximately 60 minutes. The table below summarizes the specifications of the Tempest Airframe.

The Skywalker X8 [34] UA was designed specifically for this research. The airframe is the Skywalker X8 FPV aircraft which contains a large payload volume to house the required avionics and sensors. This commercial approach provides for a cheap airframe that requires minimal effort to convert to a UA. The foam construction results in a robust system for this type of application. The table below summarizes the specifications of the aircraft.

4.2.2 SwiftPilot Avionics System

The SwiftPilot (Figure 4.3) from Black Swift Technologies (BST) is a lightweight, customizable, and low-cost autopilot. The 70 x 34 x 27 mm package weighs 34 grams. Similar to the Piccolo Plus, the SwiftPilot utilizes a 6 axis IMU, GPS, a dynamic pressure sensor for airspeed, and a static pressure sensor to determine altitude. The SwiftPilot is the main component of the Black Swift Technologies RF sensing package that enables work at three different frequencies including 2.4GHz WiFi, a 900MHz primary communication link,

Table 4.2: Tempest Airframe Specifications

Wingspan	3.2m
GTOW	5.4kg
Motor	Neu 1509 3Y
Battery	11Ah 5S Lipo
Endurance	60 minutes
Launch	Winch

Table 4.3: Tempest Airframe Specifications

Wingspan	2.12m
GTOW	3.5kg
Motor	AX2820 KV780
Battery	5Ah 4S Lipo
Endurance	35 minutes
Launch	Hand Launch

and a 433MHz module. The SwiftPilot allows access to every control loop in the cascaded PID controller through the SwiftPilot SDK allowing higher level planning algorithms to perform robust trajectory planning and following. The SwiftPilot allows both software and hardware in the loop testing utilizing the X-Plane flight simulator. A provided SDK allows interfacing to the SwiftPilot through NetUAS over the 2.4GHz link.

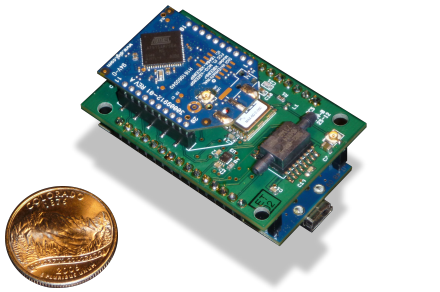

Figure 4.3: The BST SwiftPilot

4.2.3 RF Sensing Hardware

The BST [12] RF sensing system is used for measuring received signal strength of three different protocols each at their own frequency. For this work specifically the 433MHz link is measured between two HopeRF RFM22B FSK [36] transceiver modules. The radios return the address of the source radio along with the signal strength, so there is no data association problem. The 433MHz RF sensor along with the SwiftPilot are connected to an on-board avionics computer, the RouterStation from Ubiquiti [40]. The avionics computer is running a custom version of the OpenWRT Linux distribution [37]. During data collection, ground based beacons shown in Figure 4.4 emit signals for the airborne system to read, and maintains a log of its GPS based location measurements for use in post-processing and assessing the performance of localization and tracking algorithms.

The 433MHz signal is reported as an 8 bit unsigned integer with a value from 0 to 255. This value is converted to dBm signal strength using a chart from the RFM22B data sheet which shown in Figure 4.5. All of the data gathered in the course of these experiments fits in the linear regime resulting in a conversion

Figure 4.4: The RF emitting beacon.

function of:

$$P_{p,s}^{db} = 0.51(\text{RSSI}) - 123.1 \tag{4.1}$$

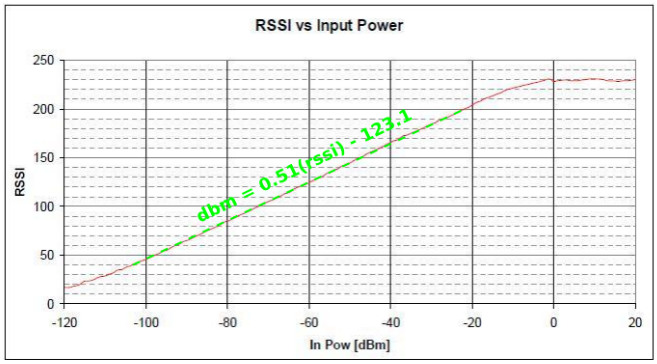

Figure 31. RSSI Value vs. Input Power

Figure 4.5: The fit from the HopeRF data sheet [35] with the function fit overlayed in green.

4.2.4 Software Architecture

For the multi-aircraft experiments modifications and additions to the NetUAS were made that were specifically tailored for this work. Specifically, a new interface was implemented to interact with the 433MHz sensor. The 433MHz sensor utilized a USB interface that returned an ASCII stream that included the emitter

ID and RSSI measurement.

The networking between the different aircraft and ground nodes runs on an 802.11 multi-hop mesh network utilizing the B.A.T.M.A.N. Advanced routing protocol [29] version 2012.1. This routing protocol is seamlessly used by the distributed planning algorithms to coordinate the vehicles and send measurements back to the fusion center. The sharing of plans and measurements was done for pre-determined IP addresses in the mesh.

4.3 FAA Certification

All flight experiments to support this work were flown under an Certificate of Authorization (COA) from the U.S. Federal Aviation Administration (FAA). The operation of unmanned aircraft systems in the U.S. National Airspace System (NAS) is governed by the Federal Aviation Administration. All of the flights to support this dissertation were flown in either the Table Mountain test site, Figure 4.6(a), and the Pawnee National Grasslands site, Figure 4.6(b) [45]. The FAA required separate COAs for each area and each airframe. This work also included securing a COA to allow multi-UA flight operations in a single COA area for the multi-UA RF sensing system.

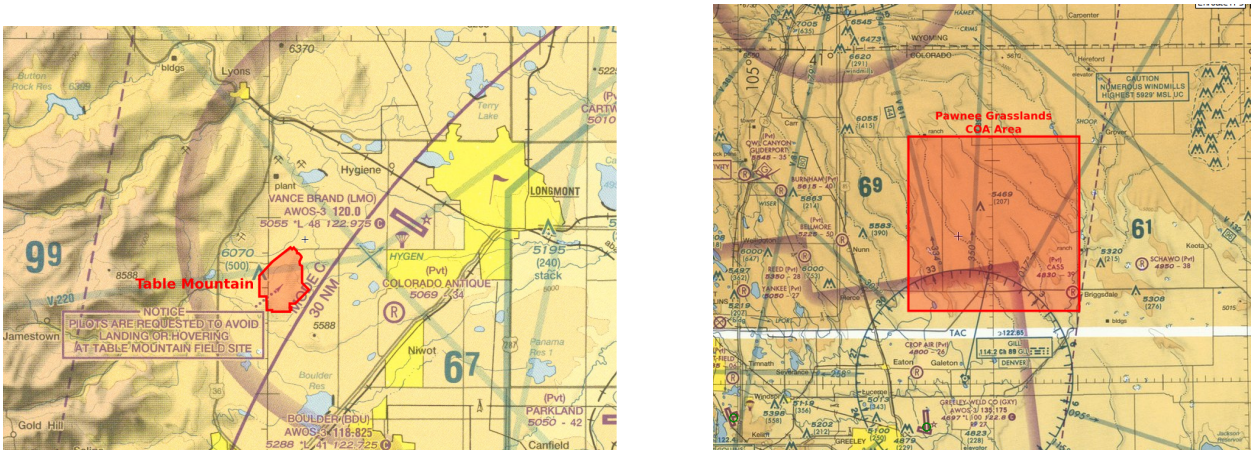

(a) (b)

Figure 4.6: Maps of (a) the Table Mountain test site and (b) the Pawnee National Grasslands test site.

Chapter 5

Radio Frequency Localization Experiments

Unmanned aircraft systems are advantageous platforms for performing RF source localization. First, UAS mobility enables rapid surveying of large areas. Second, the motion of the UA provides spatial diversity in the measurement geometry, which can improve the observability problem and performance of the estimation algorithm. Third, by flying overhead the aircraft can maintain much better line of sight (LOS) to any nodes on the ground compared against a similar ground-based system. This greatly reduces the fading (interference and noise) effects caused by multipath propagation in many scenarios, especially open areas [49].

This chapter presents a formulation and flight test results for geo-localization of stationary RF nodes. Two different frequencies were used for the experiments: (1) IEEE 802.11 (WiFi) nodes emitting at 2.4GHz along with (2) 433MHz emitters. This chapter focuses on work done to localize 2.4GHz emitters using the NexSTAR UAS. The sole sensor utilized for the localization is the received signal strength indication (RSSI) measurement that is provided on-board. Measurements are received as packets that include the identifying MAC address along with the RSSI measurement.

5.1 Localization of 2.4GHz Emitters

This work utilizes the unscented Kalman filter (UKF) [18] to perform RF source geo-localization. The UKF is chosen over the more conventional extended Kalman filter (EKF) [50] because of the nonlinearities of the RSSI measurement function. A sequential estimator is developed rather than a batch parameter estimator because real-time estimates of the state and uncertainty are required for active sensing planning

algorithms that can improve sensing geometry and estimation performance [46]. See Appendix A.2.2 for more details on the filter used here.

Figure 5.1 below shows the RSSI data gathered using the NexSTAR UAS [39] over two flight days from four different emitters. A least squares fit was performed on this data to calculate values for κ and α.

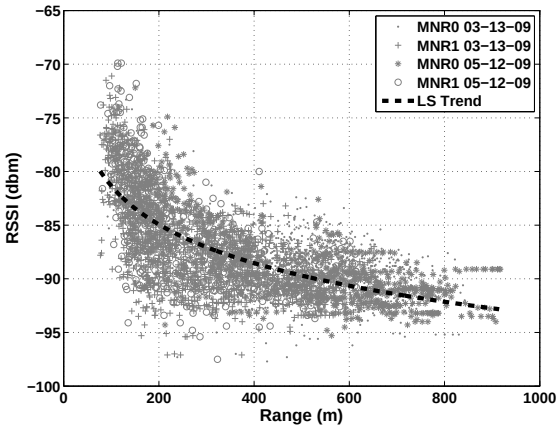

Figure 5.1: RSSI vs. Range measurements from 4 flight experiments.[46]

It is assumed that the on-board sensor has a maximum detection range of 800m. As a result, the estimator is always initialized with a position estimate chosen over a uniform random distribution from the sensing aircraft within the detection range. Though this could lead to high initial errors, results will show that the UKF was able to converge to a solution for the flight data that was gathered.

5.1.1 Results

The UKF was tuned using flight data (Figure 5.2) gathered on May 20th 2009 at the Table Mountain test range [5]. The process noise, $\mathbf{Q}$ and initial covariance $\mathbf{P}_0$ were tuned to give fast convergence while minimizing the final error. The GPS position of the node averaged over several minutes was assumed to be the true position. The measurement noise $\mathbf{R}$ is based on a least squares fit of the RSSI vs. range data

similar to what is seen in Figure 5.1. The $\mathbf{Q}$, $\mathbf{P}_0$, $\mathbf{R}$ were set to:

$$\mathbf{Q} = \begin{bmatrix} 10^{-2} & 0 & 0 & 0 \\ 0 & 10^{-2} & 0 & 0 \\ 0 & 0 & 5 \times 10^{-10} & 0 \\ 0 & 0 & 0 & 5 \times 10^{-9} \end{bmatrix} \tag{5.1}$$

$$\mathbf{P}_0 = \begin{bmatrix} 2 \times 10^4 & 0 & 0 & 0 \\ 0 & 2 \times 10^4 & 0 & 0 \\ 0 & 0 & 10^{-7} & 0 \\ 0 & 0 & 0 & 2 \times 10^{-4} \end{bmatrix} \tag{5.2}$$

$$\mathbf{R} = [9] \tag{5.3}$$

These three parameters are kept the same for all of the subsequent flights described in this work. Figure 5.2(a) shows an overview of the flight at Table Mountain along with the position estimates of the WiFi node (computed offline). Figure 5.2(b) shows the estimate error compared to the node position with the 3σ error bars. Note that the error does a good job of staying within these bounds. The results presented for the tuning are specifically for the state vector incorporating the radio parameters.

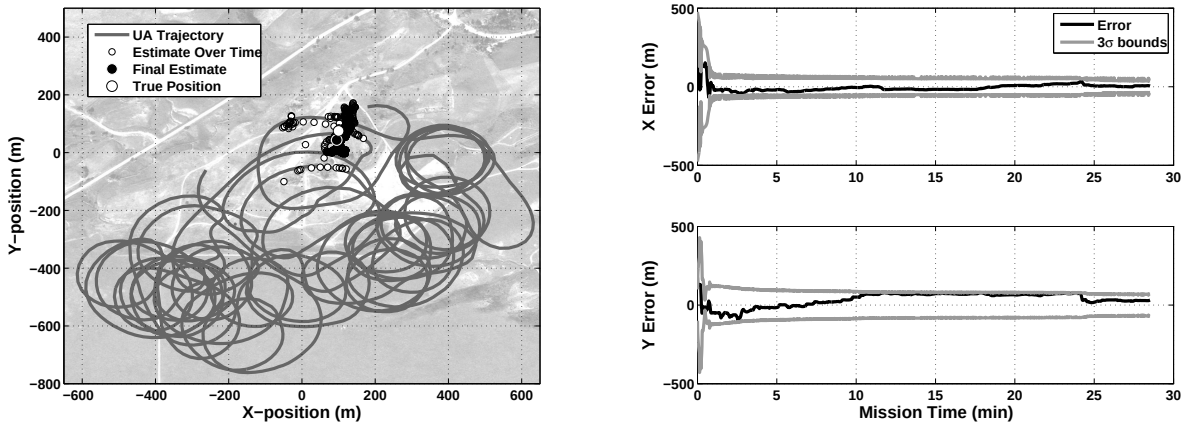

(a) (b)

Figure 5.2: (a) Overview of the flight trajectory and estimated position of the WiFi source. (b) True position errors with 3σ error bars.

5.1.1.1 Comparison of two different filter designs.

The four state UKF is compared against a UKF that uses the position only as the system state to demonstrate the improvement in having the radio parameters in the state. The two-state UKF keeps the radio parameters κ and α fixed. These two filter formulations were compared for six localization experiments spanning four flight days [5]. Table 5.1 shows a summary of the final error between the estimated position and the GPS position. Incorporating the radio parameters into the UKF results in less error for each run, with an average error reduction of 45.4%. This result matches other observations that show that the RF environment can vary greatly over the course of one flight, let alone over multiple days [5]. The two different antenna types used in these experiments are described in Section 5.1.1.3.

Table 5.1: Comparison of final error between the two UKF formulations

Date	Antenna Type	2 State UKF Error (m)	4 State UKF Error(m)	Error Reduction
2009-05-20	Omni	45.45	31.87	29.9%
2009-05-12	Omni	67.52	28.33	58.0%
2009-05-12	Omni	80.34	35.44	55.9%
2009-03-13	Dipole	136.72	44.57	67.4%
2009-03-13	Dipole	156.77	83.64	46.6%
2008-10-14	Dipole	42.40	36.32	14.4%

5.1.1.2 Localizing Multiple Targets

To further demonstrate the filter, multiple WiFi emitters were localized simultaneously. Figure 5.3(a) and Figure 5.3(b) show two separate flight tests localizing two emitters. Two separate unscented Kalman filters are run for each flight, generating separate estimates of the target position, transmission power κ, and path loss exponent α. Though α describes the RF environment, the propagation paths from the two emitters are different and could lead to slightly different values for α. Identification is performed from each node's unique MAC address that is contained in the packet along with the RSSI measurement. These two plots show that the trajectory of the aircraft and the estimates throughout the flight for both emitters.

It should also be noted that the hardware setup between these two flight days differs. The flight on 2009-03-13 (Figure 5.3(a)) had a regular dipole antenna attached to the 802.11 radio on the aircraft whereas

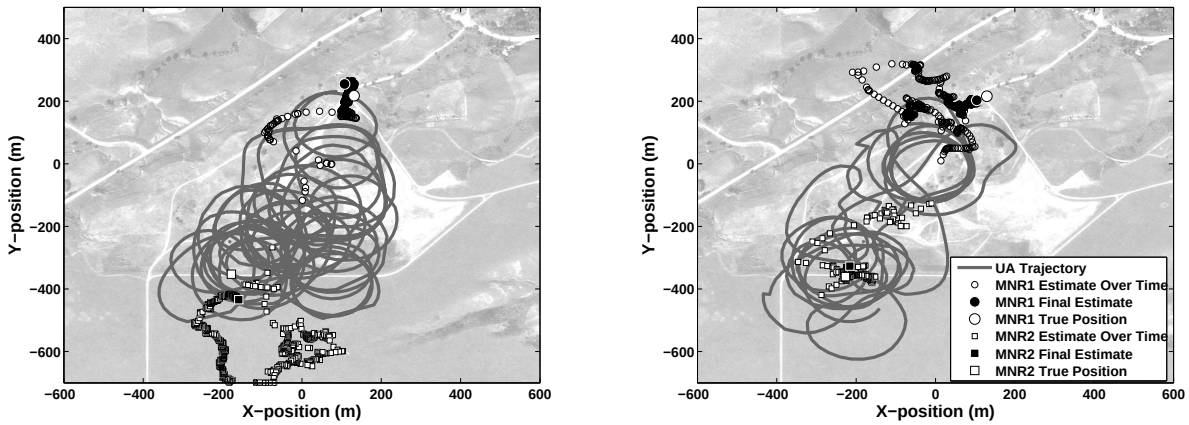

(a) (b)

Figure 5.3: Overview of the estimation of two nodes with a (a) dipole antenna and (b) true spherical antenna in the UA. The circles are Node 1 and the squares are Node 2.

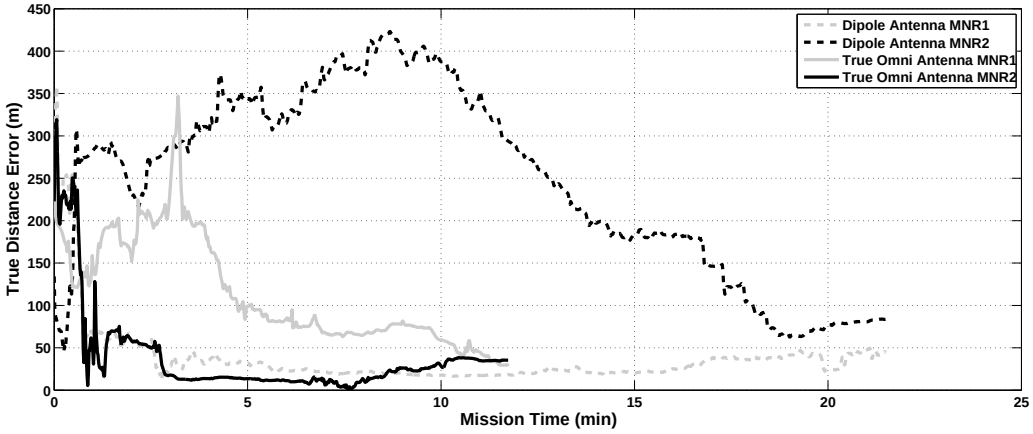

Figure 5.4: Comparison of the true errors from both flights.

the flight on 2009-05-12 (Figure 5.3(b)) had a true omni antenna attached to it with a spherical antenna pattern. The differences in performance of these two antennas is examined next.

5.1.1.3 Dipole Antenna vs. True Omni

One of the issues with utilizing UAS for this type of localization is that the antenna orientation of the sensing radio will change with the orientation of the aircraft. Since a regular dipole antenna has a

doughnut shaped antenna pattern [31], banking the aircraft towards or away from the node being localized will cause a change in RSSI that is not accounted for in the measurement model of the UKF. Experiments were conducted with both a dipole antenna and a true omni antenna that has a spherical antenna pattern in three dimensions, meaning that the orientation of the aircraft will not affect the RSSI measurement.

Two different flight tests were conducted using these two different antennas. The nodes being sensed were placed in similar positions for these flights and similar trajectories were flown. Since the UKF randomly chooses the initial conditions, it was run offline 500 times for each set of flight data to compare the differences in the UKF when applied to data collected by the two antennas. Using the spherical omni antenna showed a significant improvement in the estimate. Figure 5.5 shows a histogram comparison of the 500 runs for each flight. It was found that 91.7% of the time the spherical omni had less than 50m error, while the dipole only accomplished this 9.2% of the time. The dipole antenna had an average final error of 199.9m, while the spherical did much better at 30.5m. This result is expected since the measurement function essentially assumed a spherical antenna pattern and hence was a better representation of the data collected with the true omni antenna. The implication of these results are that the antenna patterns of both the transmitting and receiving (UAS) radios needs to be known or estimated for good tracking performance.

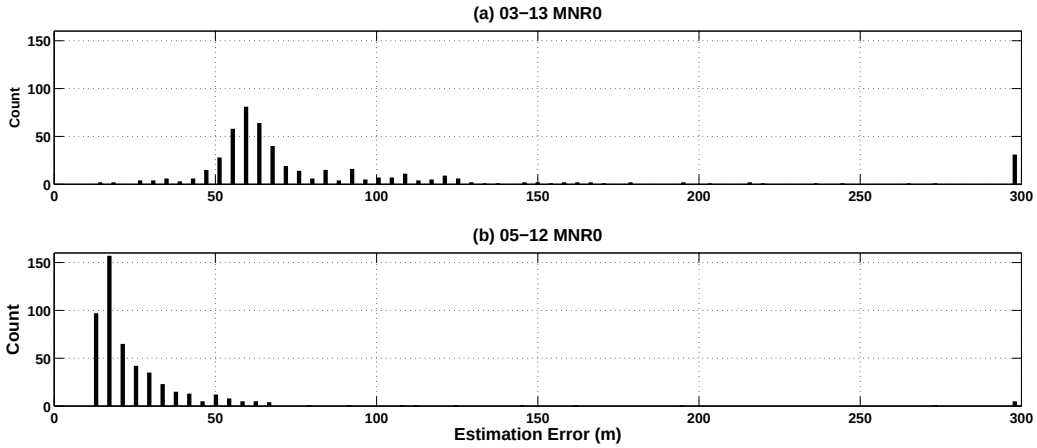

Figure 5.5: Histograms comparing the estimation errors for (a) a regular dipole antenna and (b) a spherical pattern antenna over 500 runs. For clarity the errors greater than 300m were binned to 300m on the histogram.

5.2 Radio Frequency Localization of 433MHz Emitters

This section describes experiments performed to compare different estimators in localizing 433MHz RF emitters. 15 flight experiments were flown to compare the EKF, UKF, and Particle Filter. See Appendix A.2 for details on the three estimation algorithms. Comparisons were done and it was shown that the UKF and PF both have similar performance but the UKF is computationally more efficient. For this work a total of 15 flight experiments were conducted under FAA COA's. All flight experiments were conducted at an altitude of approximately 100m above ground level using either the Tempest or Skywalker X8 airframe with the SwiftPilot RF sensing system.

Figure 5.6 contains the results of a specific flight test for the UKF and shows the aircraft trajectory with overlayed position estimates over the course of the flight. Figure 5.7 is the error with 2σ covariance bounds of the state variables $[x, y]$. The true values of x and y are based on the measured GPS position of the MNR.

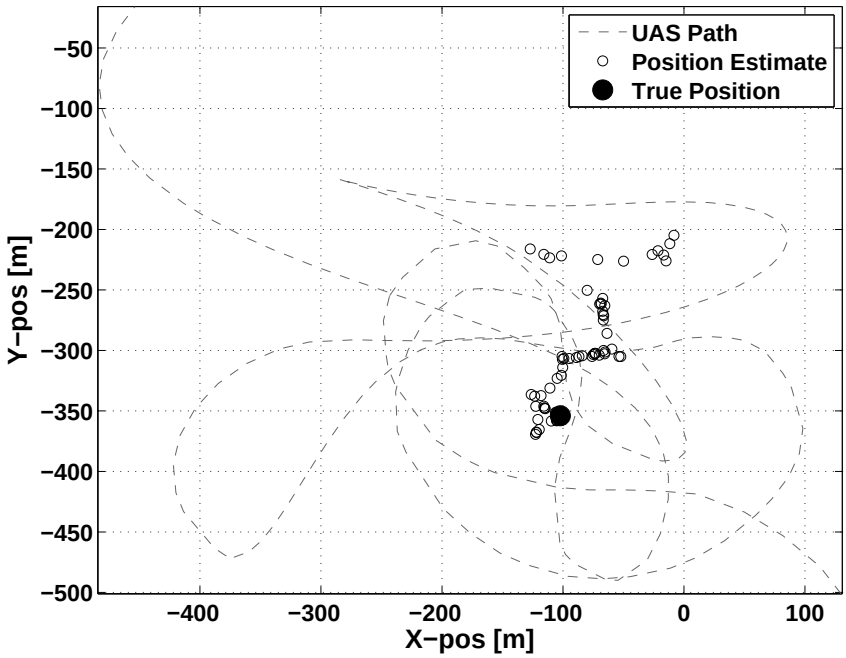

Figure 5.6: UKF trajectory with filter estimates.

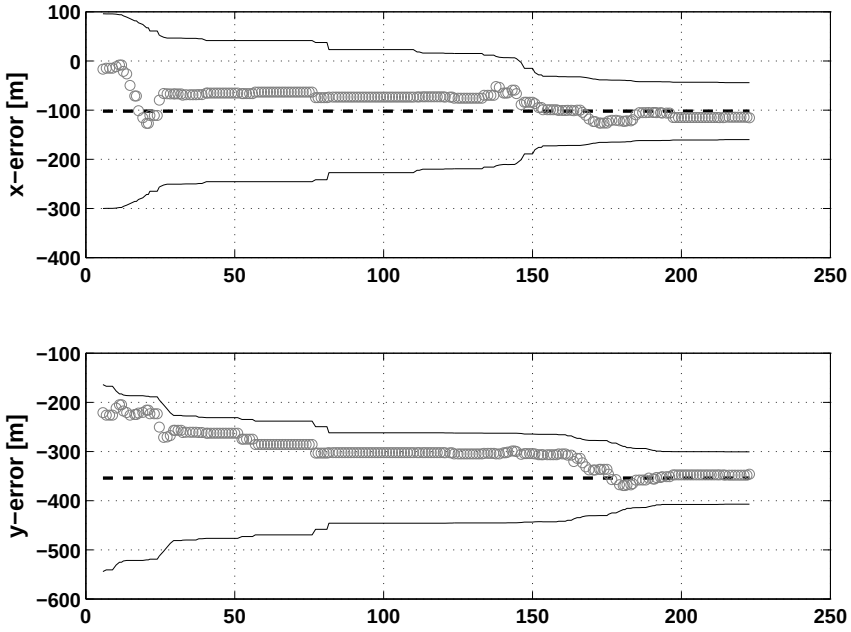

Figure 5.7: UKF x and y state errors with covariance bound.

5.2.1 Comparisons of Error

The performance of the filters are compared over all 15 of the flight experiments. Figure 5.8 contains the final position estimate of all 15 runs for the UKF, EKF, PF along with a batch estimator that processes all of the measurements simultaneously. Note that the local coordinate system for all flight experiments has an origin at the true MNR position, so in Figure 5.8 the true position is always the origin.

Now, lets examine the RMS error to compare the filters. Table 5.2 summarizes the RMS error over the duration of each experiment for the three filters considered. This table shows that the RMS error average over all 15 runs is very similar for the UKF and PF with the UKF doing slightly better. The EKF runs result in an RMS error that is around double the other two filters.

5.2.2 Varying Initial Conditions

Next lets investigate the sensitivity of the estimators to the initial XY position estimate for the target. In this subsection we compare the UKF, EKF and PF by averaging over the RMS and final errors over 10

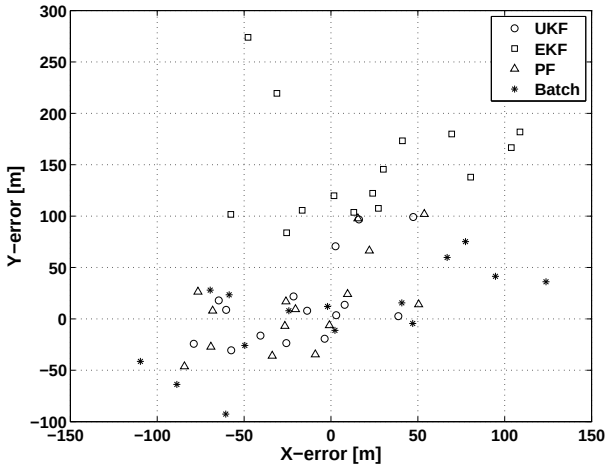

Figure 5.8: Comparison of final error for the 15 flight experiments.

Table 5.2: Comparison of the RMS error of the UKF, EKF, and PF

Run	UKF	EKF	PF
1	54.475619	100.472648	72.426069
2	66.320865	129.550860	73.753278
3	93.523608	118.530551	106.523886
4	113.625201	207.602142	109.708648
5	109.927401	167.766781	102.052957
6	129.705132	161.490911	135.404864
7	46.610845	155.874704	63.989727
8	60.105433	187.975298	74.001782
9	40.307259	204.478662	73.760890
10	71.159307	98.495014	65.765419
11	66.114343	146.899503	69.026192
12	48.509772	123.688565	42.484053
13	61.690903	114.563181	41.883992
14	58.452549	123.593202	39.416316
15	62.914190	123.187899	77.284578
Average	72.229495	144.277995	76.498843

runs with varied initial conditions. The plot below shows the averaged final errors graphically for all 15 runs:

Now, lets examine the RMS error to compare the filters. Once again, note that the errors are averaged across the 10 different runs with different initial estimates of the 2D position. Table 5.3 illustrates that the performance of the filter is not very sensitive to the initial guess of the emitter location and the performance

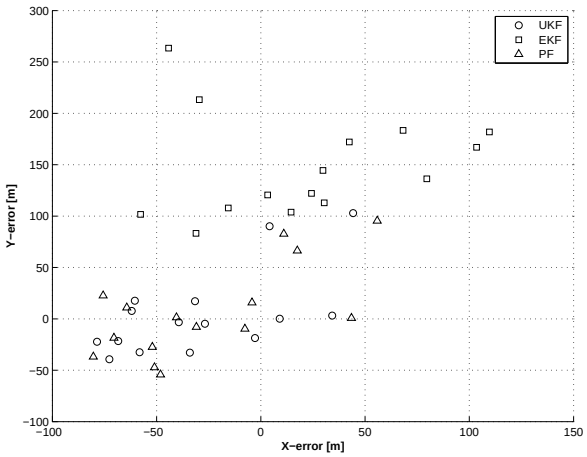

Figure 5.9: Comparison of final error for the 15 flight experiments for varied initial conditions

of the three filters is consistent with the previous sub-section.

5.2.3 Examining The Consistency Of The Different Filters

The experiment from Section 5.2.2 can also be used to measure the consistency of the filters. NEES (normalized estimation error squared) or Squared Mahalanobis distance is a metric of estimator consistency. It is defined as

$$NEES = \tilde{x}P^{-1}\tilde{x} \tag{5.4}$$

$$\text{where } \tilde{x} = x - \hat{x} \tag{5.5}$$

and P is the estimate's covariance matrix. We average the consistency i.e. NEES over the 10 runs from Subsection 5.2.2 to calculate ANEES (Average NEES).

We illustrate the comparison of the filter consistencies and ANEES using one of the experiments.

The NEES provides a single metric to combine the estimator accuracy with its confidence. Table 5.4 shows the average ANEES for each of the estimators over the different datasets. Again, we once again have similar performance for both the UKF and PF, with the EKF lagging behind in performance.

Table 5.3: Average RMS Error over varied initial conditions.

Run	UKF	EKF	PF
1	102.976141	98.932342	60.046421
2	72.585995	130.128328	75.467982
3	102.707571	119.538989	99.549227
4	115.894557	203.435750	113.060715
5	95.447963	167.545306	89.053345
6	128.504206	165.436358	121.192959
7	59.611726	152.433004	80.132752
8	67.848509	189.317968	77.965726
9	89.962875	206.842281	107.698603
10	92.054134	96.162405	100.323110
11	61.077884	149.084937	61.015343
12	48.073523	125.635491	43.114891
13	71.607337	113.867953	69.238168
14	66.114158	126.802949	62.623611
15	83.893632	119.475495	85.003760
Average	83.890681	144.309304	83.032441

Table 5.4: Average ANEES over the 15 flights.

Run	UKF	EKF	PF
1	10.148842	20.461809	3.801378
2	6.788238	37.809648	7.607790
3	4.985616	22.957916	9.992477
4	7.895886	23.272946	11.377674
5	2.208845	9.315427	1.869855
6	4.704092	10.958020	5.665178
7	1.081404	7.893515	2.953320
8	0.971426	12.864685	1.262961
9	2.169709	29.251126	2.065835
10	1.231119	2.102476	1.699970
11	0.820897	7.791210	0.802100
12	1.376205	5.839091	0.976613
13	0.874574	3.129895	0.959887
14	0.755482	4.279931	0.692040
15	1.283364	2.805053	1.219086
Average	3.153047	13.382183	3.529744

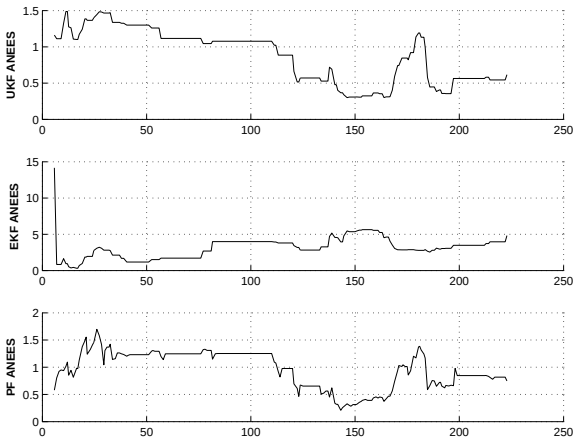

Figure 5.10: Comparison of filter consistency

5.3 Summary

These 433MHz localization experiments were used to compare the UKF, EKF, and PF. These experiments show the EKF has the worst performance of these three filters as expected due to the non-linearity of the measurement equation. The UKF and PF were close in performance with the UKF being computationally much cheaper. These experiments verified the choice to utilize the UKF in the planning experiments for both single and multi aircraft flight experiments.

Chapter 6

Flight Experiments of the Planning Algorithm

This chapter presents the results of experiments assessing the planning algorithm presented in Chapter 3. Experiments were run using a combination of the Tempest and Skywalker UAS described in Chapter 4. All flights were conducted at approximately 100m AGL. For all of the planning based flight experiments presented in this chapter the sensing objective was to localize stationary 433MHz emitters broadcasting 5 times per second. Four key sets of experiments were conducted:

(1) Localization of stationary RF radio beacons. This was done for both 2.4GHz and 433MHz beacons utilizing different UAS platforms. This work was described in Chapter 5 and will not be discussed further here.

(2) The development of an empirical packet erasure channel communication model. This is based on both air-to-ground and air-to-air flight experiments utilizing two way radio communication over a WiFi routing protocol.

(3) The demonstration and assessment of the planning algorithm for the specific case of a single aircraft. The experiments were first configured with the emitter and fusion center close together resulting in near perfect communiation throughout the flights. This was done to assess the performance of the planning algorithm focused mainly on sensing. Another single-aircraft experiment was run with the emitter far from the fusion center to assess the shortcomings of the system due to communication limitations.

(4) The demonstration and assessment of the planning algorithms for two aircraft. These experiments

successfully demonstrated the algorithms on a real system performing the RF localization task. The experiments were also used to showcase the improvement multi-hop communication can have on a multi-UAS system.

The work presented in this chapter will provide the flight results and assessment for Item 3 and Item 4 in the above list.

6.1 Single UA Flight Experiments

Single-aircraft experiments were flown to assess the improvement in sensing when the planning algorithm is utilized versus flying patterns without planning. These experiments involved the Tempest or Skywalker UAS localizing a stationary 433MHz source. A total of 16 flight experiments were flown. These experiments had three primary functions: (1) demonstrate the planning algorithm running in real-time on-board a small UAS, (2) assess the performance of the planning algorithm in localizing these RF sources compared with no planning, and (3) assess the limitations of a single-aircaft system due to limited communication range helping motivate the multiple UA experiments.

6.1.1 Mutual Information Path planning

For the single-aircaft planning the UA solves Problem 3, maximizing the modified local mutual information utility, which is equivalent to solving Problem 2 in the case of a single UA.

$$\begin{aligned} \mathbf{u}^{1*}_{1:10} = \quad & \arg\max J^1_3(\mathbf{u}^1_{1:10}) = \arg\max I(X_{10}, \tilde{y}^1_{1:10}(S^1_{10}(\mathbf{u}^1_{1:10})) \\ \textbf{subject to} \quad & \mathbf{u}^1_t \in [-\omega_{\max}, \omega_{\max}], \quad \forall t \in [1, \cdots, 10] \\ & \mathbf{s}^1_{t+1} = f^1_s\left(\mathbf{s}^1_t, \mathbf{u}^1_t\right) \end{aligned} \tag{6.1}$$

where f_s is defined in Equation 2.27 for a non-holonomic vehicle and $\omega_{\max}$ is the maximum turn-rate of the vehicle, computed from the maximum bank angle. For these experiments the maximum bank angle was set to 30^o, which resulted in an $\omega_{max} = 18.0$deg/s for the Tempest and $\omega_{max} = 23.2$deg/s for the Skywalker. The on-board computer plans over a 10 second horizon with a 1 second time step. The control is run in a receding horizon manner where the control horizon is half the planning horizon (5 seconds) followed by replanning for a further 10 seconds. The optimization is done on-board utilizing a standard genetic algorithm (GA)

[55]. At each planning step the GA initializes with the remainder of the previous optimal solution padded with 5s of flying straight along with three cases of (1) fly straight for 10s, (2) max right turn for 10s, and (3) max left turn for 10s. The initial population is also seeded with 6 uniform random sets of turn rates. Each new generation of trajectories is generated by selecting the trajectories with the best utility and performing mutation and cross-over. Utilizing the on-board processor running for a fixed time of two seconds allowed for approximately 100 generations of the fixed population size of 10 resulting in the evaluation of a total of 1000 possible trajectories.

There were a total of 16 experiments flown to evaluate single-aircaft planning. 15 of these experiments the RF target source was placed near the sensor fusion base station so that communication between the two was nearly perfect. This was done to evaluate the planning algorithm to improve the sensing. Figures 6.1 and 6.2 show examples of the trajectories for a flight with no planning and a flight with planning respectively. Appendix A.3 contains the trajectories for all other experiments. The 9 experiments with no planning

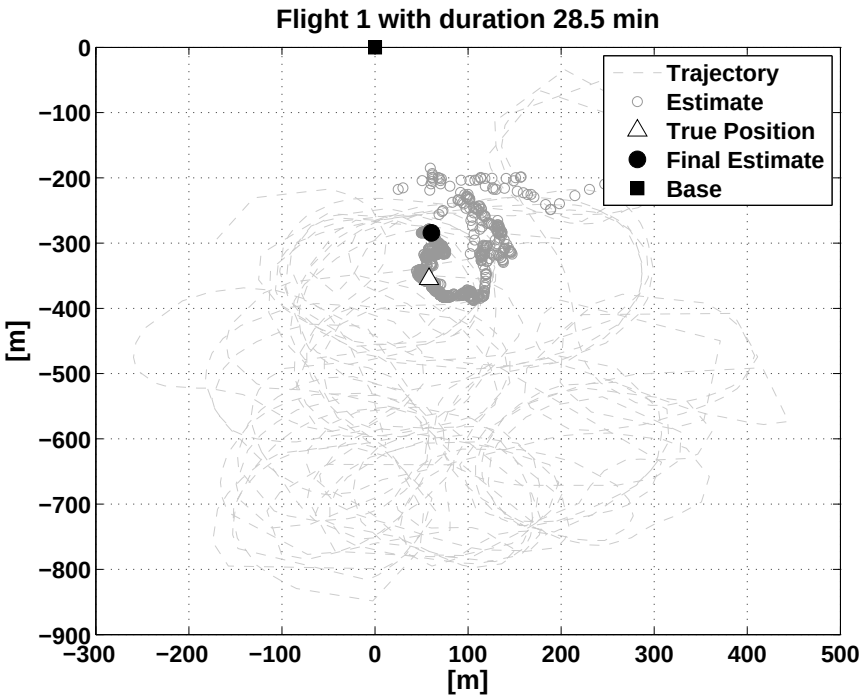

Figure 6.1: The trajectory for a flight with no planning.

involved having the aircraft fly different waypoint patterns near the emitting node. During these experiments

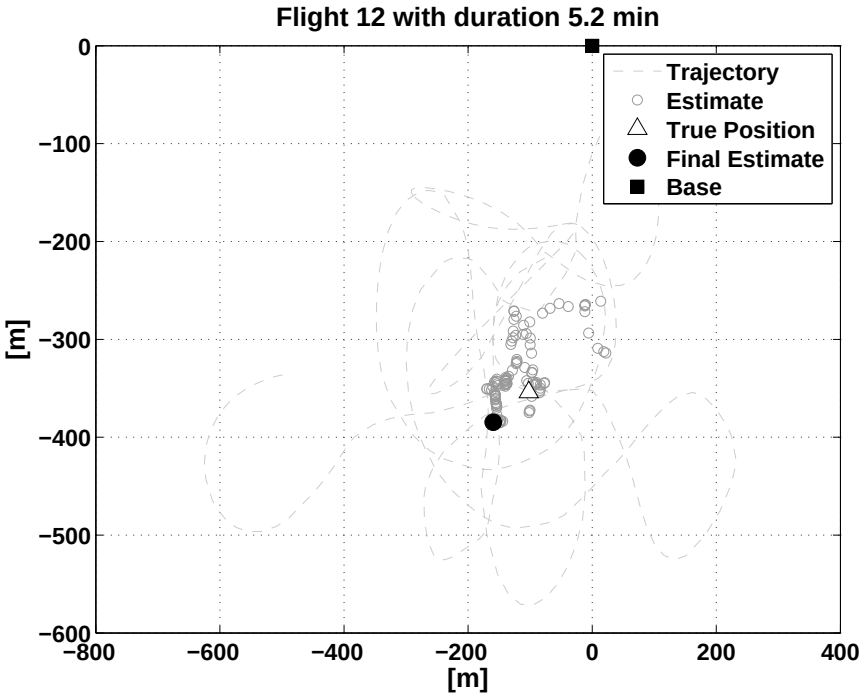

Figure 6.2: The trajectory for a flight with planning.

the waypoint plan was moved irregularly to give good coverage around the emitting node. The 6 experiments that ran the planning algorithm were sent to an orbit point prior to turning on the planning and estimation algorithms simultaneously. The trajectories flown, shown in Figure 6.2 and Appendix A.3, fly paths that attempt to get as close to the emitter as possible, limited by the altitude of the aircraft. It has been shown that for a range estimate the maximum information gain from measurements occurs as the distance between the UA and the emitter decreases [11] to a minimum, which is constrained by the altitude of the UA. The information contribution of each measurement can be calculated from the Jacobian of the measurement function. Since this will result in a matrix, we compute a scalar quantity based on *A-optimal* design [8], which is a simplification that utilizes the trace of the measurement contribution, $tr\left(\mathbf{H}^T\mathbf{R}^{-1}\mathbf{H}\right)$ to compute informative paths [26]. For the RF localization problem, the function is shown in Equation 6.2. In this equation the only term that can be controlled is the range r, and minimizing the r value will maximize this equation.

$$tr\left(\mathbf{H}^T\mathbf{R}^{-1}\mathbf{H}\right) = \frac{100}{\sigma_{RSSI}^2}\left[\frac{\alpha^2}{(\ln(10))^2}\left(\frac{\alpha^2}{r^2}+\frac{1}{\kappa^2}\right)+\log_{10}\left(\frac{1}{r}\right)\right] \tag{6.2}$$

Examining the performance of the localization for the planning vs. no planning case, Figure 6.3 is a plot comparing the distributions of the final position error for all 15 experiments. The plot shows that the final position error of the flights that included planning resulted in better performance with respect to the error versus the non-planing flights. Note that the initial error for all experiments was set to 100m in both the x and y axis relative to the true position for all experiments. Several experiments were conducted at different locations, though the global coordinate systems were converted to a local x-y frame centered at the true position of the RF emitter. The RMS error was averaged across the no-planning and the planning

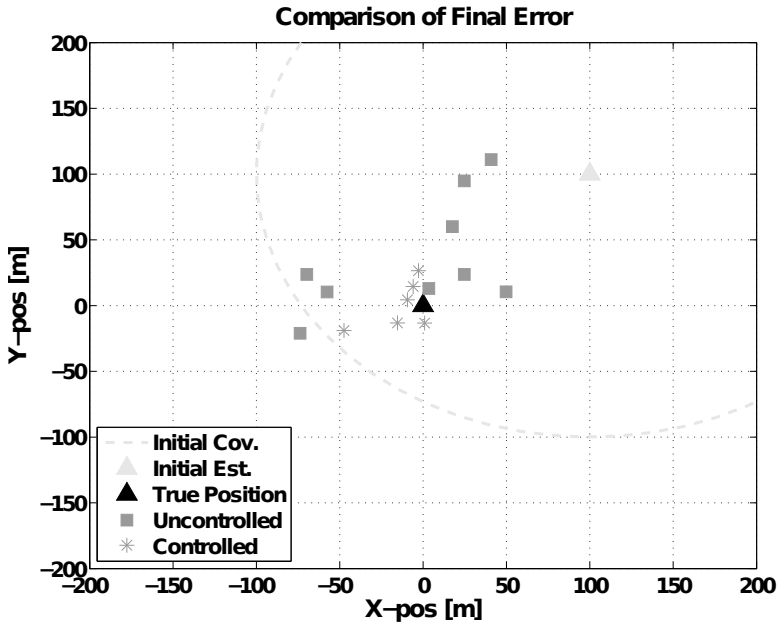

Figure 6.3: Overview of the final position error of the estimate comparing the planning vs. no planning experiments.

experiments. Because experiments were run for different durations, the RMS error for the first three minutes of each experiment was computed. The average RMS across the no-planning experiments was 108.6m with an average final error of 90.2m. For the planning experiments the average RMS was 67.0m with an average final error of 29.9m. This is a reduction in RMS error of 62%. Figure 6.4 shows the mutual information gained for all 15 flight experiments, comparing the flights with planning to those with none.

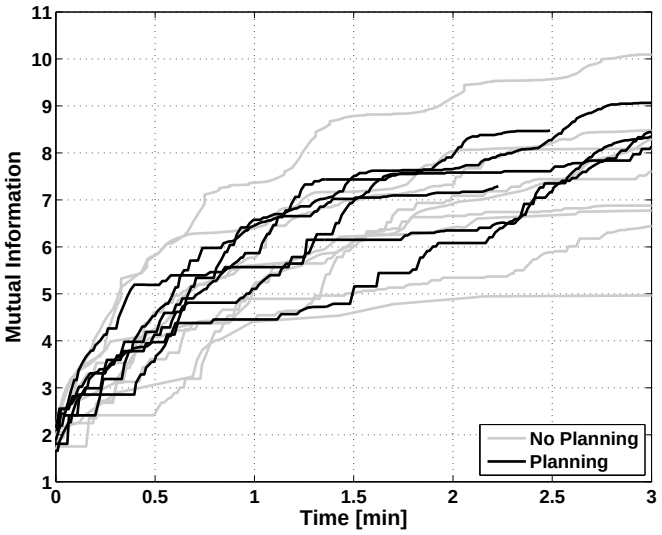

Figure 6.4: Comparison of mutual information gained for planning and no planning.

6.1.2 Communication Limitations

An additional experiment was run using the planning algorithm, with the base station and the RF source placed approximately 1km apart. The purpose of this experiment was to assess performance when communication is stressed. The algorithm works well in that it allows a single aircraft to achieve results that would not happen if communication was ignored. The planer does well in that it plans a trajectory that gets some information to the fusion center. The path planning algorithm pushed the aircraft to the point where 44.1% of packets were lost. A path planner based only on sensing would have flown close to the emitter putting it outside of communication range to where none of those measurements would have been received by the fusion center.

The measurements at this range resulted in poor performance by the UKF and a final RMS error of 121.6m and a final position error of 145.7m. This experiment was run to motivate the need for multiple aircraft to improve the range of the sensor network. Figure 6.5 is a plot of the flight trajectory and estimated position. Note that the estimate drifts to the North-East away from the true position over the course of the experiment.

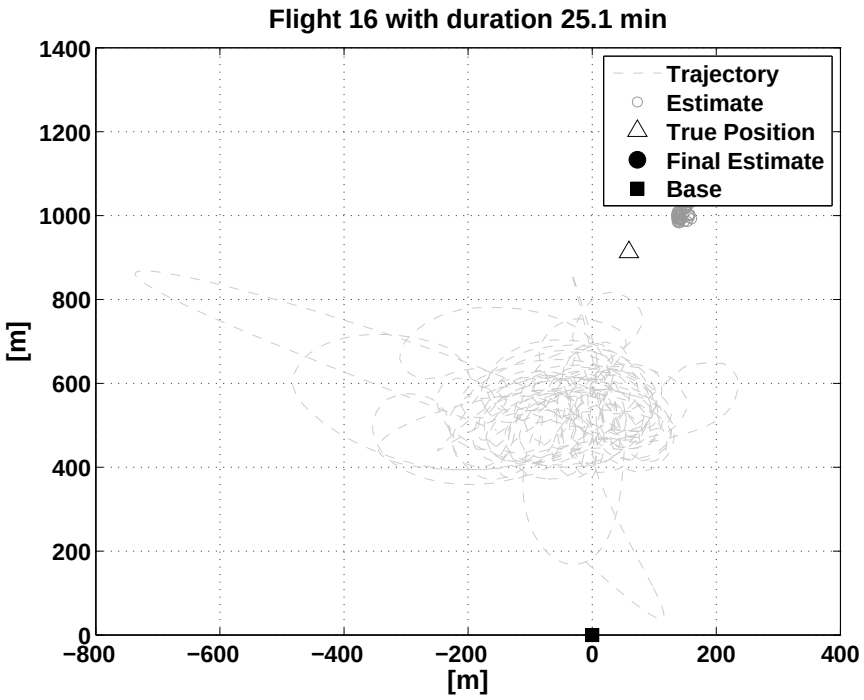

Figure 6.5: Trajectory overview of the communication limited single-aircaft experiment.

6.2 Multi UA Flight Experiments

The two-aircraft experiments involved the Tempest and Skywalker UAS performing cooperative localization with a ground based fusion center. The system utilized the B.A.T.M.A.N. Advanced mesh network. Figure 6.6 has a high level overview of this system. The fusion center was a MacBook Pro running Gentoo Linux. Collision avoidance was maintained by altitude separation, so one aircraft flew at approximately 100m AGL and the other at 120m AGL. The Tempest was flown at a commanded speed of 18m/s and the Skywalker at 14m/s. The two-aircraft experiments were flown on 2013-07-02, 2013-07-08, and 2013-07-11 at the Table Mountain site. A total of four experiments were flown. Due to FAA restrictions and RECUV practice, each experiment required six people to perform, limiting the number of experiments that could be performed.

As in the single-aircraft experiments each aircraft planned a 10s trajectory and then flew 5s before replanning. For these experiments the Skywalker was labeled vehicle #1 and the Tempest vehicle #2. Using the hierarchical planning scheme in Problem 3, the Skywalker planned first to optimize its own modified

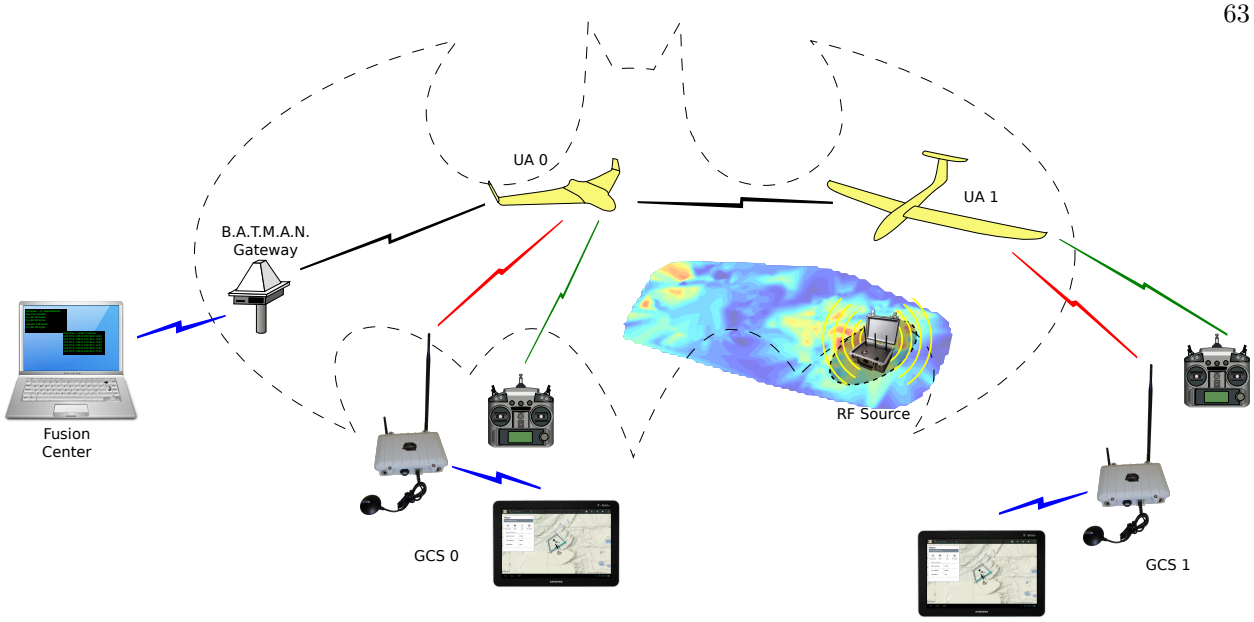

Figure 6.6: Overview of the two-aircraft testbed.

mutual information utility i.e.

$$\begin{aligned} \mathbf{u}^{1,h}_{1:10} = \quad & \arg\max J^1_3(\mathbf{u}^1_{1:10}) = \arg\max I(X_{10}, \tilde{y}^1_{1:10}(S^1_{10}(\mathbf{u}^1_{1:10})) \\ \textbf{subject to} \quad & \mathbf{u}^1_t \in [-\omega_{\max}, \omega_{\max}], \quad \forall t \in [1, \cdots, 10] \\ & \mathbf{s}^1_{t+1} = f^1_s\left(\mathbf{s}^1_t, \mathbf{u}^1_t\right) \end{aligned} \tag{6.3}$$

For these experiments the maximum bank angle was set to 30^o for both aircraft, which resulted in an $\omega_{max} = 18.0$deg/s for the Tempest and $\omega_{max} = 23.2$deg/s for the Skywalker. The Skywalker's plan is then passed to the Tempest which computes it's plan.

$$\begin{aligned} \mathbf{u}^{2,h}_{1:10} = \quad & \arg\max J^2_3(\mathbf{u}^2_{1:10}) = \arg\max I(X_{10}, \tilde{y}^2_{1:10}(S^2_{10}(\mathbf{u}^2_{1:10}))|\tilde{y}^{1,h}_{1:10}) \\ \textbf{subject to} \quad & \mathbf{u}^2_t \in [-\omega_{\max}, \omega_{\max}], \quad \forall t \in [1, \cdots, 10] \\ & \mathbf{s}^2_{t+1} = f^2_s\left(\mathbf{s}^2_t, \mathbf{u}^2_t\right) \end{aligned} \tag{6.4}$$

Each aircraft attempted to transmit any new measurements to the fusion center. The UKF at the fusion center performed an update whenever new data was received and sent out the updated state and covariance to each aircraft to use for the initial conditions in the planner. Since the first vehicle in the hierarchy only plans for itself it utilizes the single link model in Equation 2.13 while the second aircraft has to evaluate the two possible choices by solving:

$$\beta_t^2(\mathbf{s}_t) = \max\left[\beta_t^{2,b}, \beta_t^{2,1} \times \beta_t^{1,b}\right] \tag{6.5}$$

Three types of experiments were flown to compare different scenarios and evaluate the performance of the planning algorithm. The first involved having the fusion center close to the target. This effectively allowed the aircraft to plan in a perfect communication environment, resulting in both aircraft flying close to the target. The second multi-aircraft experiment involved an emitter much further from the fusion center with only direct communication. This was to assess the performance of the algorithm with an emitter at a range from the fusion center beyond the communication capabilities of the network. The third set of experiments involved the same configuration as the second with the change of using multi-hop communication to extend the range of the sensor network.

6.2.1 Good Communication Case

This experiment was used as a baseline for the best that two aircraft could do to localize a target without range limitations. The separation between the fusion center and the emitter was only 17m. The resulting trajectory from this flight experiment is shown in Figure 6.7. For the RF localization formulation, the most information is gained the closer the aircraft are to the emitter as shown in Equation 6.2. The trajectories overfly the estimated emitter position, where they achieve the minimum distance possible to the target based on their altitude.

6.2.2 Limited Direct Communication Case

The second experiment was done to assess the performance of the planning algorithm with direct communication using two aircraft when communication is stressed similar to the single-aircraft experiment in Section 6.1.2. The emitter was placed much further from the base station, precisely 1250m away. The resulting trajectories from this experiment are shown in Figure 6.8. The trajectories of both aircraft stayed close enough to the fusion center to allow communication similar to the single-aircraft experiment involving a similar scenario. These trajectories allowed the two aircraft to get some measurements back to the fusion center. Though this scenario is still submodular, the resulting trajectories motivate using multi-hop

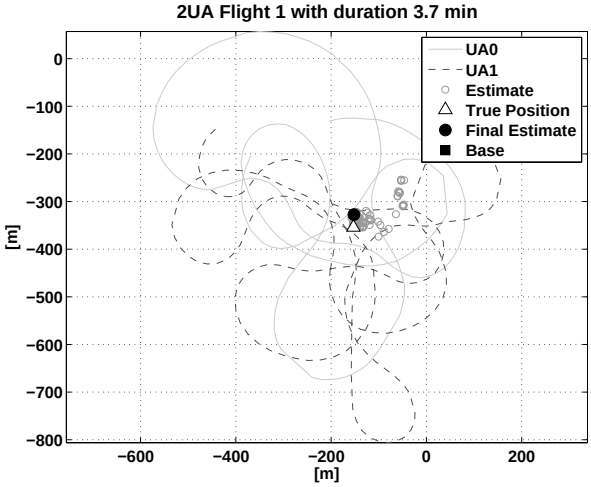

Figure 6.7: Flight trajectory of 2 UA localizing a close in target

capabilities to extend the range of the network to get one of the sensing aircraft closer to the emitter.

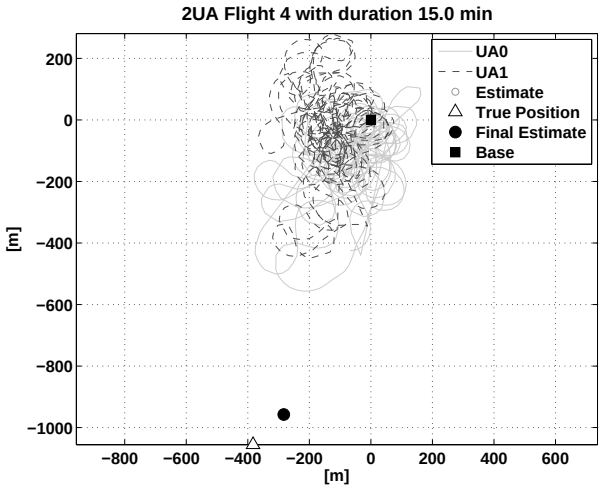

Figure 6.8: Flight trajectory of 2 UA localizing a far away target with only direct communication

6.2.3 Multi-hop Communication Case

The final set of experiments involved a similar scenario to the second experiment, but now the aircraft can perform multi-hop communication which the planning algorithm now incorporates. The resulting trajectories (Figures 6.9 and 6.10) have one of the aircraft position itself between the leading aircraft and the emitter, effectively acting as a relay. This shows one of the key features of this planning algorithm where

there is no explicit assignment of an aircraft to be a sensor or a relay but this behavior emerges for this scenario. This relay-like behavior is a direct result of the prioritization of the aircraft. Aircraft #1, which has the relay like behavior, optimizes only its own trajectory without factoring in the other aircraft. This constrains it to not exceed a certain range from the fusion center as was shown in the single-aircraft experiment with a far away emitter in Figure 6.5. Aircraft #2, which plans second in the priority and considers the first aircrafts trajectory, takes advantage of the location of aircraft #1 and flies closer to the emitter using #1 as a relay. These trajectories result in much better localization performance despite losing the submodularity property present in the trajectories in Figure 6.8.

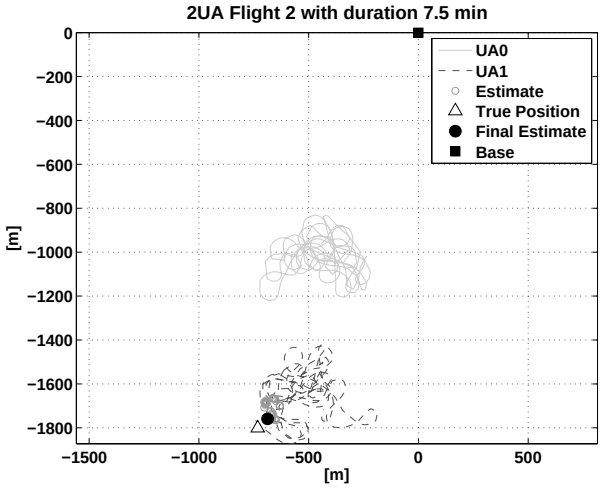

Figure 6.9: Flight trajectory of 2 UA localizing a far away target with multi-hop communication

6.2.4 Performance Comparison

The performance of these respective experiments is compared for a set time of 3 minutes from the start of the experiment. As expected, the close in case with two aircraft had the best performance, with an RMS error on the location estimate of 34.2m and a final error of 26.6m. This is also an improvement over the single-aircraft planning experiments that were flown close to the target with an average RMS error of 67.0m. The case with direct only communication for two aircraft did fairly poorly, having an RMS error of 140.4m and a final error of 139.7m. This performance was expected and is similar to the single-aircraft experiment with an emitter placed a distance from the fusion center with both showing very little improvement in

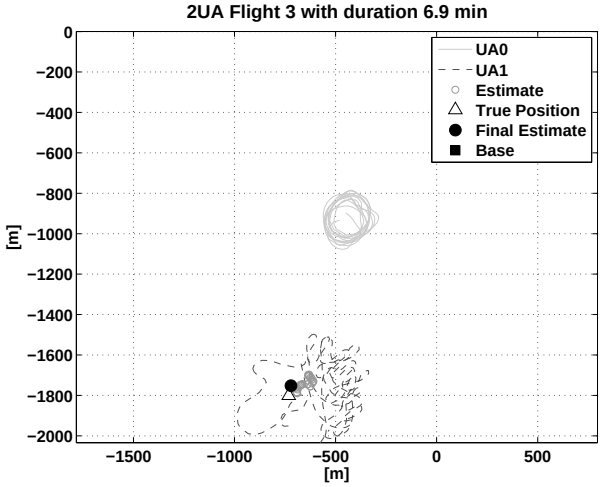

Figure 6.10: Flight trajectory of 2 UA localizing a far away target with multi-hop communication

sensing. Taking the measurements that far away from the target produced very little improvement in the localization of the target.

The multi-hop case produced an average RMS of 82.5m and a final position error averaging 55.9m, illustrating the utility of planning with multi-hop for this particular scenario. Figure 6.11 below shows a comparison of the final error for the 4 experiments; (1) the close in case, (2) the direct communication case, and (3) and (4) the multi-hop case. Figure 6.11 also contains the associated covariances to show the consistency of the estimator. The error ellipses plotted here are 2σ and for the plots the estimates are well within these bounds showing efficient estimation. Computing the mutual information gained for each of these 4 flights results in values of 9.0 for the "perfect" communication case, 3.0 for the direct communication case with the emitter far away, and 6.6 for both of the multi-hop experiments with the target far away.

The setup for the experiments with the target far away was at the edge of the ability of the aircraft to form a chain and get one aircraft close to the target, resulting in the primary sensing UA not being able to fully cover the area around the target, as seen in Figure 6.10. A slightly closer target probably would have reduced the multi-hop RMS to something closer to the single-aircraft cases discussed in the previous section and allowed the error in the two-aircraft experiment to likely come close to the case of one aircraft flying close to the RF emitter.

The two experiments involving multi-hop communication also pushed the limits of the network. They

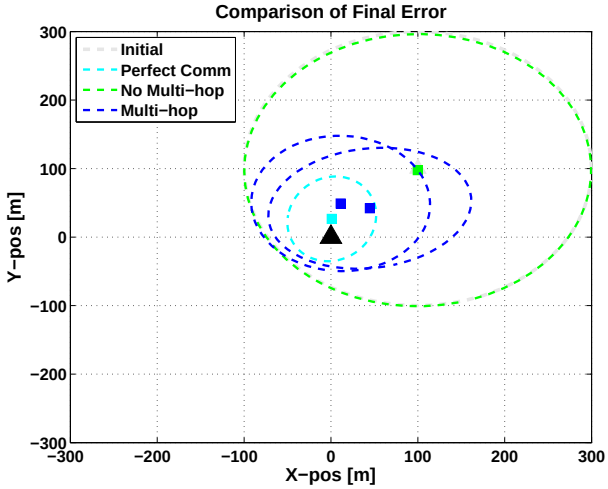

Figure 6.11: Comparison of the performance for different communication cases

resulted in 41.1% and 30.2% packet loss for the two flights for the aircraft more distant from the fusion center. This large number of dropped packets only had a small affect on the performance of the respective estimators. Figure 6.12 shows estimator performance at the base (with dropped packets) against the same estimator run offline using all of the measurements that were stored on-board each aircraft. The key part of these plots is the dashed lines, which represent the covariance bound of each estimator, which is a measure of how much information was gathered in the packet loss vs. the perfect communication case. Computing the mutual information, the estimator at the base achieved 93.0% and 96.8% of the mutual information using all of the measurements. This small difference indicates that the planner did a good job of balancing packet loss and sensing. In the first experiment, the estimator with dropped packets actually did better in terms of the final error in position with less packets but the uncertainty is less (i.e. there is more information) for the case with no dropped packets as expected. It should be noted that this discrepancy in final error is due to the stochastic nature of the estimator and examining the covariance based error is more useful.

Figure 6.13 shows a comparison of the mutual information gained for the four experiments. The performance of improving mutual information with each flight matches the error performance. The flight with the emitter close to the fusion center reached the highest mutual information in the shortest amount of time. The experiment with the emitter far from the fusion center that only planned with direct communication had the lowest mutual information. The two experiments with the emitter far away in which the planner

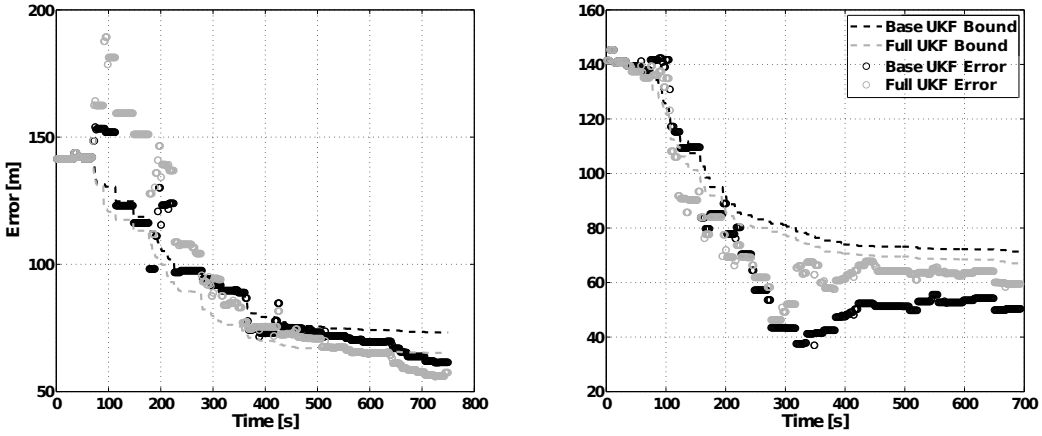

Figure 6.12: Plots analyzing the performance of the estimator in the face of packet loss

utilized multi-hop communication had mutual information values in between the other two cases.

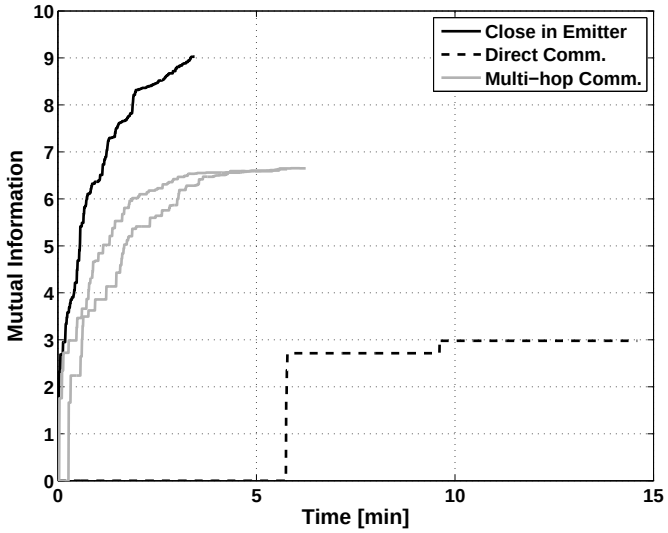

Figure 6.13: Comparison of mutual information gained for the two-aircraft experiments.

6.3 Multiple UA Simulations

Further simulations were run to analyze the performance of the algorithms for multiple UA. All of these examples are based on localization of stationary RF emitters with the sensing properties based on the 2.4GHz WiFi sources. In all cases the aircraft were tasked with getting the measurements back to a fixed

base station which is responsible for the sensor fusion. The communication is based on the multi-hop network with each individual link modelled with the packet erasure channel model. When packets are dropped, the measurements contained in them will not be incorporated into the target estimates. The objective of these example cases is to assess the performance of the planning algorithm along with running more complex scenarios than were possible for the flight experiments.

Two scenarios were established involving 2 aircraft localizing one RF node. Two separate trajectory planners were run, the first maximizing only the sensing gain by setting $\beta_t^{i,j} = 1$ for all links, i.e. ignoring the communication limitations of the aircraft. The second trajectory planner is utilized the empirical link model in Figure 2.5. Figure 6.14 shows the trajectories flown using the two approaches. The algorithm maximizing sensing only sends both aircraft towards the target, as seen in Figure 6.14(a). However, this is at the edge of their communication range resulting in a significant amount of dropped packets. The planning algorithm that incorporates the link model results in the trajectory seen in Figure 6.14(b). The algorithm maximized the flow of information to the base station, which resulted in one of the aircraft being positioned as a relay and the other flying close to the emitter.

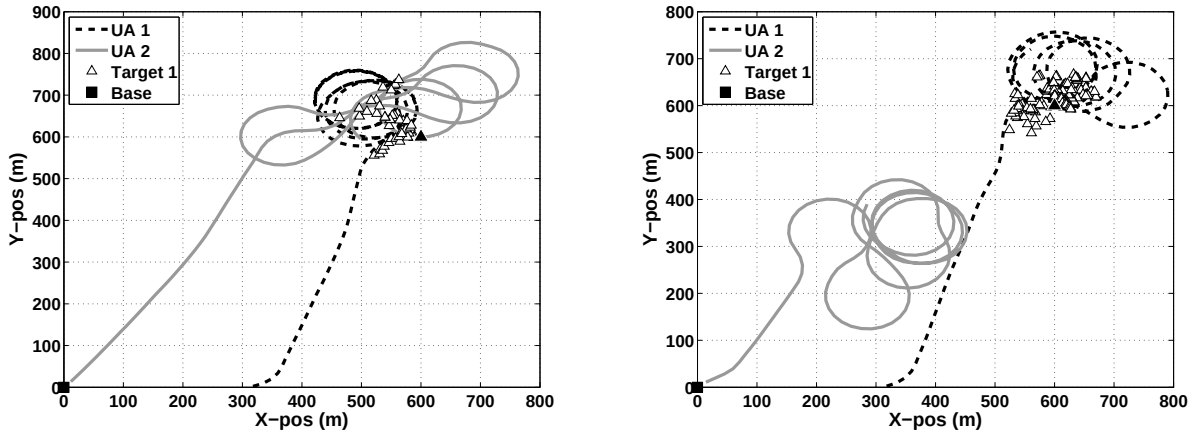

(a) (b)

Figure 6.14: Comparison of trajectories when (a) communication is not added to the planning and (b) when it is (right)

Figure 6.15 shows the error comparison between the two cases. The algorithm with communication

implicitly in the planning was able to converge to a good position solution. The long periods of time with no change in error for the sensing only planner occur because measurement packets cannot reach the base station. Figure 6.16 shows a comparison of the communication performance. The plot itself shows the probability of successful transmission for each aircraft back to the base station. The plot does not show which route is chosen, just the probability of the best available route. A solid point indicates a successful transmission and an open one indicates a dropped packet. As expected, the algorithm that factors in communication performs better in terms of communication for this specific scenario. It can be seen that the periods of flat error growth in Figure 6.15 correspond to the periods of low probability and no packet delivery in Figure 6.16.

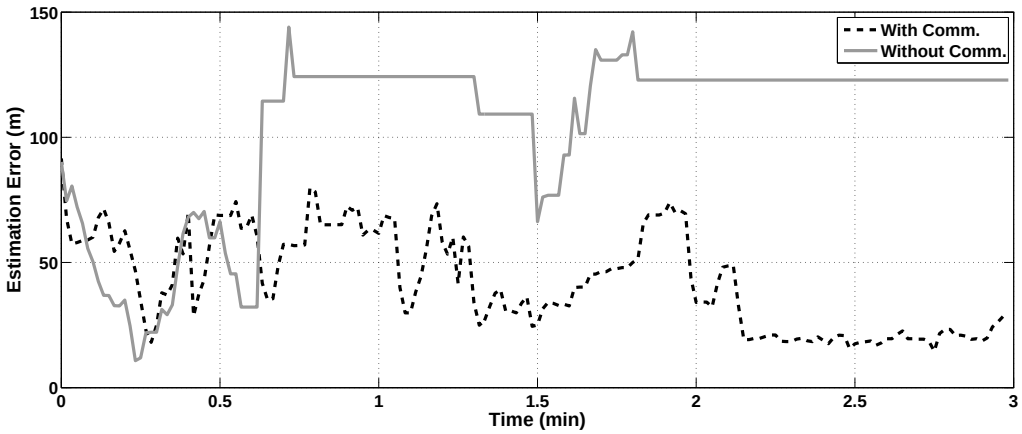

Figure 6.15: Comparison of the position errors when the trajectory planner does not factor in the communication and when it does so.

The next simulation includes two aircraft localizing three WiFi nodes. Figure 6.17 shows the trajectories and node position estimates along with the estimation error as a function of time. This case highlights trajectories where the aircraft switch between primarily sensing or communication roles but with no explicit task allocation. In particular, over the course of the simulation Aircraft 1 transitions from contributing to the information mainly from the content of sensed measurements to contributing as a communication relay. Initially, Aircraft 1 first spends just over a minute orbiting near Target 3, which is close enough to the base station where most of the measurement packets get through (Figure 6.18) causing the estimation error for Target 3 to drop quickly (Figure 6.17). Once there is little information to be gained by continuing to orbit

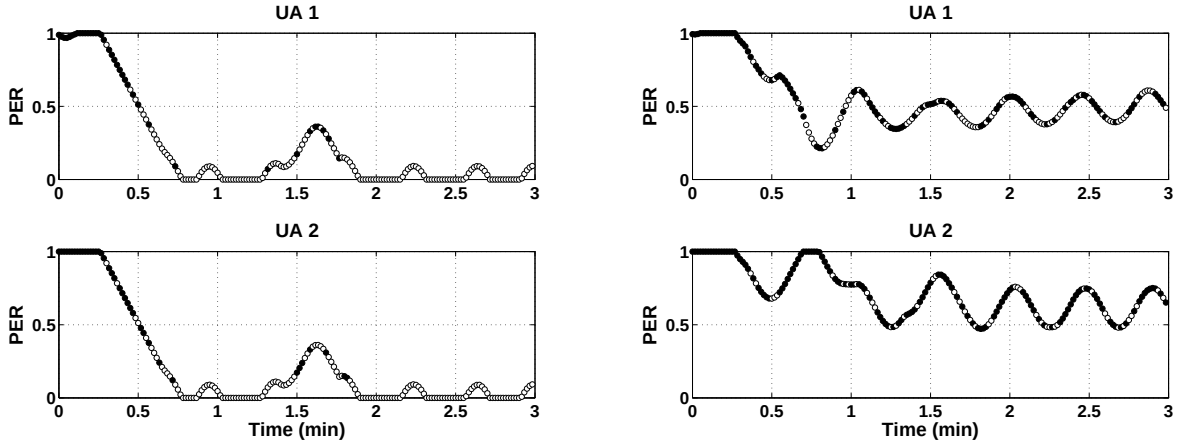

(a) (b)

Figure 6.16: Comparison of the communication performance for (a) no communication in the trajectory planning and (b) adding communication to the planning.

Target 3, Aircraft 1 moves up to act as a relay for the measurements being made by Aircraft 2. Up to this point Aircraft 2 is too far from the base station and few of its measurements get through (Figure 6.18). The communication for Aircraft 2 improves once Aircraft 1 starts relaying the measurement packets back to the base station around the 1 minute mark. From that time until just after the 2 minute mark Aircraft 2 is orbiting Target 1, and Figure 6.17 shows that shortly after these packets start to get through the error in Targets 1 position drops significantly. The error does climb again after 1.5 minutes, however, this is the actual error, while the planner is working off the predicted information gain in the estimated covariance which continues to drop. Just after the 2 minute mark, Aircraft 2 moves to orbit Target 2 and the error in that estimate drops accordingly.

The next scenario includes 3 aircraft and 2 WiFi targets. Figure 6.19 shows the trajectory and estimated position error. The two targets were deliberately placed far enough away from the base station so that direct communication would not be possible for an aircraft that is taking measurements close to the target. Aircraft 1 automatically sets itself up as a relay, while Aircraft 2 and 3 take advantage of Aircraft 1's position to fly closer to the targets and get better measurements back to the base station. The priority for the sequential planning algorithm goes Aircraft 1 $\rightarrow$ Aircraft 2 $\rightarrow$ Aircraft 3, meaning that Aircraft 1 plans

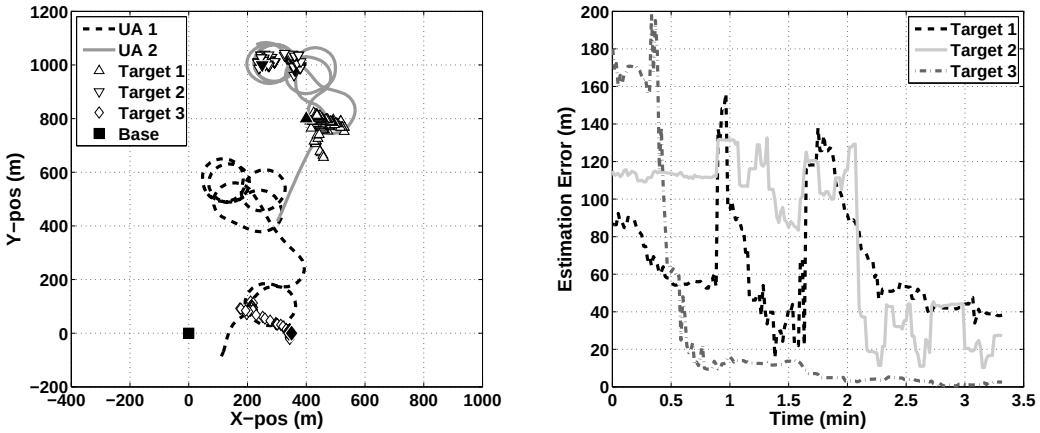

Figure 6.17: Trajectories and estimator errors for the case of two aircraft localizing three WiFi nodes.

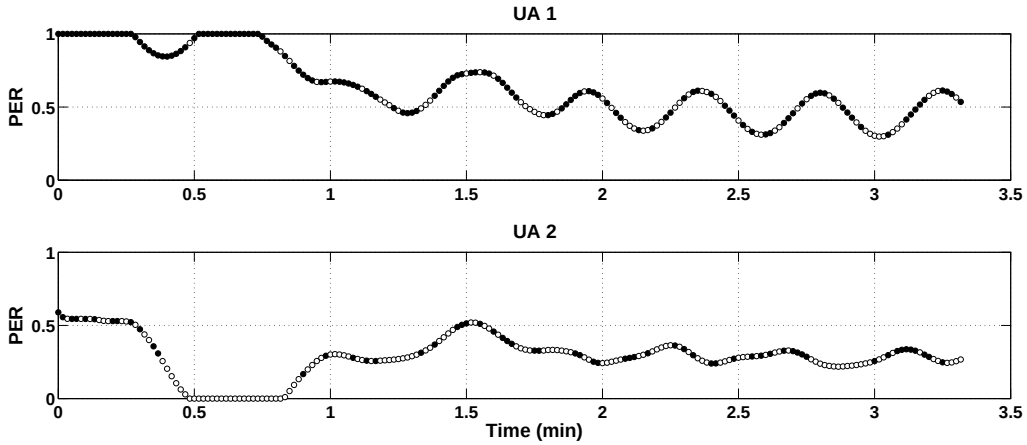

Figure 6.18: The packet error rate probability and dropped packets for the case of two aircraft localizing three WiFi nodes.

only for itself, while Aircraft 2 plans given Aircraft 1's chosen trajectory, etc. This implies that Aircraft 1 will always keep itself closer to the base station since the planner on this aircraft will not take advantage of the other aircraft to act as relays, even if it initially started closest to one of the targets.

Figure 6.20 shows the communication performance for this case. The packet error rate for Aircraft 2 and 3 is hovering around 50% or worse for most of this scenario. This illustrates how the algorithm trades between communication performance and sensing utility to improve overall information content delivered to the base. Even though only half the measurements get through, they are highly valued since the aircraft are close to the targets and total information gain is optimized.

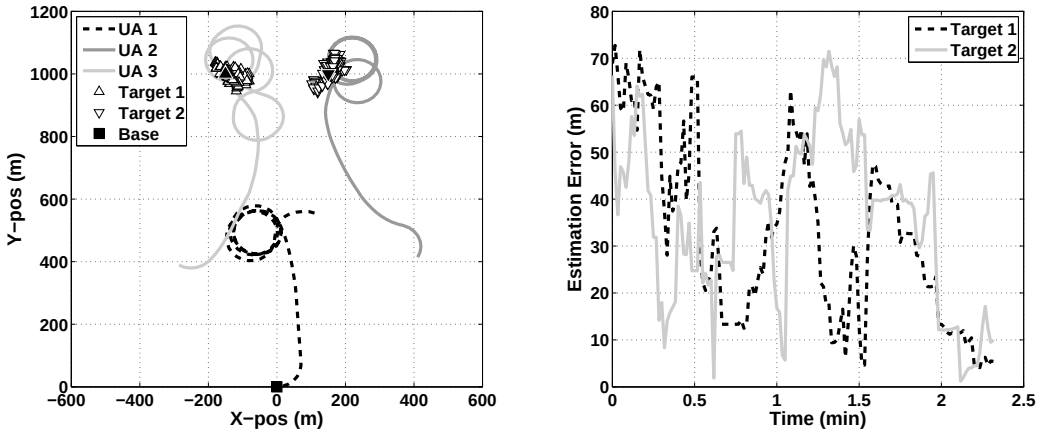

Figure 6.19: Trajectories and estimator errors for the case of three aircraft localizing two WiFi nodes.

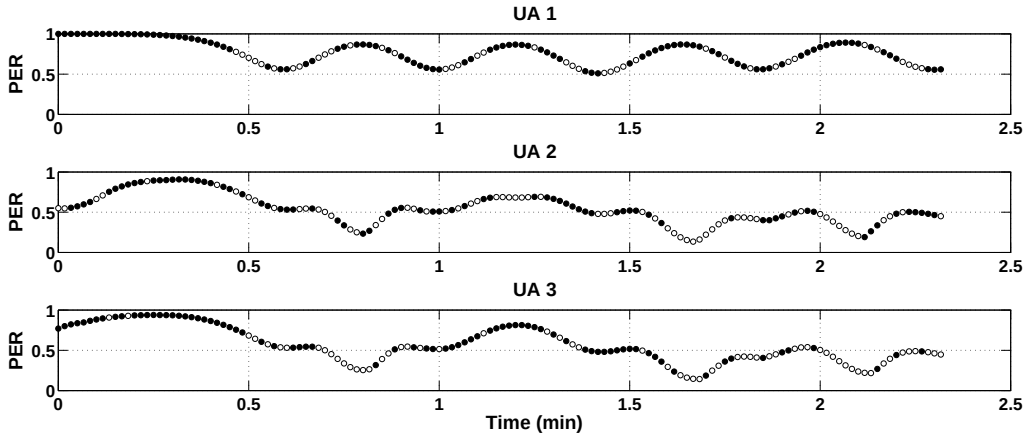

Figure 6.20: The packet error rate probability and dropped packets for the case of three aircraft localizing two WiFi nodes.

The last scenario shown in Figure 6.21 is similar to the 2 aircraft case in Figure 6.14 except now the WiFi node is further away and four aircraft are used. The team of aircraft automatically establish a multi-hop chain to get the very informative measurements from Aircraft 4 back to the base station. Though not obvious from the plot, Aircraft 4 takes approximately 1 minute to get close to the target from its starting point. The error plot in Figure 6.21 shows that the estimation error drops significantly just after the 1.25 minute mark. Looking at the packet probability of Aircraft 4 in Figure 6.22 from the 1 minute mark on, it takes about 6 measurements getting through from this time to see the drop in estimation error. This showcases the utility of measurements that are taken close to the target. The measurement packets from

Aircraft 4 are so informative that the algorithm converged to a configuration where these measurements are only getting through approximately 20% of the time (Figure 6.22). As in the previous examples, the order of the optimization goes from Aircraft 1 through Aircraft 4. This causes the multi-hop chain to always appear in this order despite the starting positions of the aircraft.

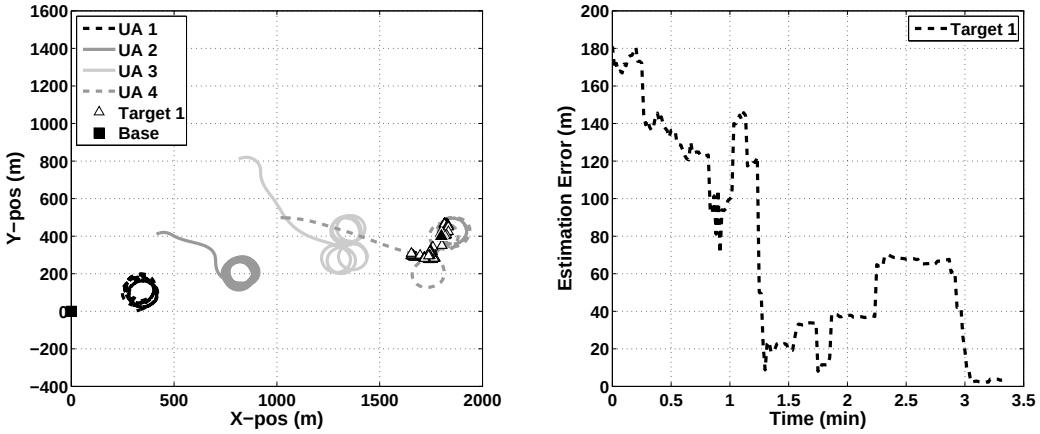

Figure 6.21: Trajectories and estimator errors for the case of four aircraft localizing one WiFi node.

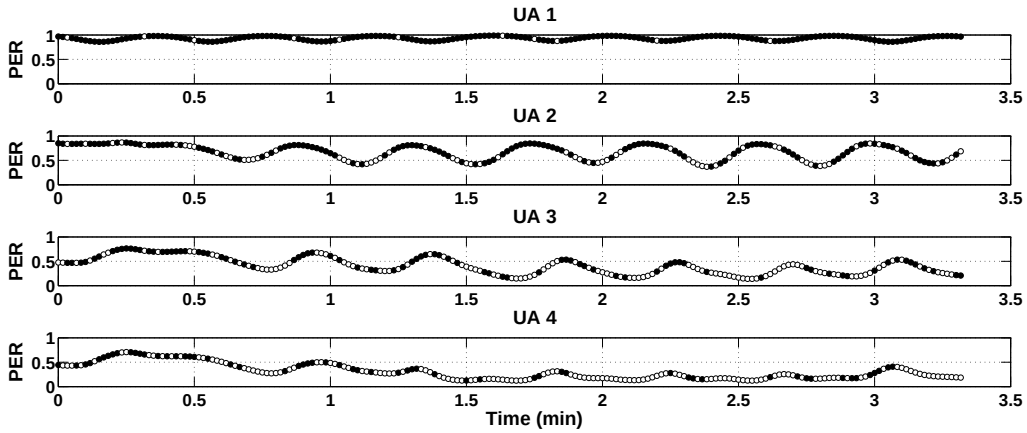

Figure 6.22: The packet error rate probability and dropped packets for the case of four aircraft localizing one WiFi node.

6.4 Summary

In this chapter experiments were presented to validate and demonstrate the algorithms and assess their performance. Using single-aircraft flight experiments a significant improvement was shown in the estimation performance for the 433MHz emitter localization problem over the flights that employed planning versus ones that did not. A similar experiment was run using two aircraft that showed further improvement in localization. The communication limitations were examined using the single-aircraft case with a target far from the base station. It was demonstrated that even using two aircraft with only the direct communication scheme had similarly poor performance because of the range to the target. It was demonstrated that using multi-hop communication to extend the range of the sensor network greatly improved performance for this scenario. Simulated experiments were also used to demonstrate the need for modelling communication in the planning along with demonstrating the distributed planning for more complex scenarios.

Chapter 7

Conclusion

This dissertation presented an algorithm for the control of a team of networked unmanned aircraft that utilized mutual information to incorporate both sensing and communication. Specifically the problem of distributed path planning for sensor networks composed of vehicles using packet erasure channels for communication was examined. The algorithm maximized the mutual information in a distributed manner for both the direct communication model and for systems employing multi-hop communication schemes.

7.1 Distributed Information Gathering Optimization Algorithm

A distributed path planning algorithm was presented and assessed. A local utility function used by each vehicle was derived as the local contribution to the mutual information of the entire team. The algorithm was assessed for both direct communication model and for systems employing multi-hop communication schemes. The planning was shown to be submodular for the direct communication scheme and could thus be bounded to within half of the global optimal. It was shown that submodularity breaks down for the multi-hop communication scheme. Over a large batch of runs it was shown that the hierarchical algorithm still has decent performance. Monte Carlo simulations were also employed to examine the sub-optimality of assumptions to make the problem tractable and these simulations showed that the performance was close to the full calculation of mutual information.

7.2 UAS Description

A key contribution of this work was the development and testing of several unmanned aircraft systems to gather communication data, demonstrate and assess the RF localization algorithms, and perform single and multi aircraft flight experiments of the planning algorithms. The NexSTAR WiFi Sensing UAS was used to develop and test the RF localization algorithm for 2.4GHz WiFi emitters. For the single and multi-vehicle path planning the Multi-aircraft RF sensing UAS was developed using both the Tempest and Skywalker airframes. All three aircraft types performed very well over a 5 year period. A total of 230 flight experiments were done in support of this work with only one aircraft lost over the entire period.

7.3 Radio Frequency Localization Experiments

RF localization experiments presented an unscented Kalman filter for WiFi emitters at 2.4GHz. Results were presented from different days of flight operations to show the performance of the algorithm for localizing stationary ground nodes. It was demonstrated that incorporating the radio parameters into the state estimate greatly improved the localization over just having the node position in the state. It was also demonstrated that using a true omni antenna over a regular dipole on the UA also resulted in a better estimate. The localization was done on ground nodes whose antennas were specifically designed to have good properties for communicating with aircraft overhead.

RF localization experiments were also flown using 433MHz emitters. These experiments were used to compare different estimation algorithms, including the EKF, UKF, and PF. 15 different experiments were flown to assess these estimation algorithms using both the Tempest and Skywalker systems. These experiments showed the EKF has the worst performance of these three setups as expected due to the non-linearity of the measurement equation. The UKF and PF were close in performance with the UKF being computationally much cheaper. These experiments verified the choice to utilize the UKF in the planning experiments for both single and multi aircraft flight experiments.

7.4 Flight Experiments of the Planning Algorithm

The planning experiments to demonstrate and assess the algorithms were presented in this dissertation. The packet loss data required for empirical link model was collected over the course of 21 flights and the link model derived. The planning algorithms were tested for the problem of localizing stationary 433MHz RF beacons. Single aircraft experiments were flown to demonstrate the algorithms running in real-time and measure the improvement in sensing from using the planning algorithm over unplanned trajectories. An experiment was also run to show the poor performance of the localization when the RF beacon is effectively outside of the communication range of the aircraft. This specific experiment was used to motivate the 2 aircraft experiments.

The multi-aircraft experiments were successfully used to demonstrated and evaluate the cooperative planning. The first aspect was demonstrating the planning and messaging architecture to perform real-time missions with the presented algorithms. Developing and fielding this system was a significant contribution of this work. The utility of cooperative sensing was demonstrated using 2 aircraft for the close in "perfect" communication case which showed improvement in estimation over the single vehicle planning experiments. The limitation of direct communication was shown for far away beacons in a third flight experiment with similar poor performance to the similar single vehicle scenario. The two final experiments run demonstrate the improvement for utilizing multi-hop communication can give in extending the range of the network. The multi-hop algorithm was also assessed and compared to a "best" case filter where all of the measurements were used (no dropped packets) and it was shown that this had little effect on the estimation and the planning algorithms found a good balance between sensing and comm.

7.5 Future Work

There are several improvements and follow-on studies that can be done to continue and improve this work. The communication link model used in the formulation of the utility metric only requires the computation of the probability of successful transmission. A natural extension of this work is to learn and adapt this model online. It was shown [5] that the radio frequency environment at the 2.4GHz spectrum

varies greatly. Learning this environment online [54] and feeding that into the link model will result in a system that is much more robust in a real-world environment. This would also allow very interesting scenarios such as dealing with active jamming sources [5] while robustly performing sensing missions.

Future work on the distributed path planning should involve new and improved schemes, specifically for the multi-hop communication case. Allowing multi-hop communication greatly extends the range and utility of UAS sensor networks and improving performance for these types of networks would improve this utility. Ideas for new planning schemes include a best response planner where each vehicle plans given assumptions of what the other team members will do.

Finally, from an experimental point of view, future work should include more testing under different conditions. These new conditions should include flying experiments with more aircraft along with testing for different configurations of RF emitters similar to the simulated experiments at the end of Chapter 6. Going one step further would involve new sensing scenarios including (1) moving targets, (2) bearings-only tracking of RF sources, and (3) entirely different sensing missions such as surface topography mapping. It was found over the course of this work that going beyond simulations and flying experiments can produce new and interesting insights into the area of path planning. Continuing this should be a big focus of future work.

Bibliography

[1] N.A. Ahmed and D.V. Gokhale. Entropy expressions and their estimators for multivariate distributions. Information Theory, IEEE Transactions on, 35(3):688 –692, may 1989.

[2] Frederic Bourgault and Hugh F. Durrant-Whyte. Communication in general decentralized filters and the coordinated search strategy. In Proc. of FUSION 04, pages 723–770, 2004.

[3] T.H. Chung, V. Gupta, J.W. Burdick, and R.M. Murray. On a decentralized active sensing strategy using mobile sensor platforms in a network. In 43rd IEEE Conference on Decision and Control, volume 2, pages 1914–1919, 2004.

[4] Thomas M. Cover and Joy A. Thomas. Elements of Information Theory 2nd Edition, chapter 7, pages 183–242. Wiley Series in Telecommunications and Signal Processing. Wiley-Interscience, July 2006.

[5] Cory Dixon. Controlled Mobility of Unmanned Aircraft Chains to Optimize Network Capacity in Realistic Communication Environments. PhD thesis, University of Colorado, 2010.

[6] Jack Elston. Semi-Autonomous Small Unmanned Aircraft Systems for Sampling Tornadic Supercell Thunderstorms. PhD thesis, University of Colorado, 2011.

[7] Jack Elston, Maciej Stachura, Cory Dixon, Brian Argrow, and Eric Frew. A layered approach to networked command and control of complex uas. Handbook of Unmanned Aerial Vehicles, 2012.

[8] V. Federov. Theory of Optimal Experiments (Probability and Mathematical Statistics). Academic Press, New York, June 1972.

[9] Brian Ferris, Dieter Fox, and Neil Lawrence. Wifi-slam using gaussian process latent variable models. In IJCAI'07: Proceedings of the 20th international joint conference on Artifical intelligence, pages 2480–2485, San Francisco, CA, USA, 2007. Morgan Kaufmann Publishers Inc.

[10] Jonathan Fink, Alejandro Ribeiro, and Vijay Kumar. Robust control for mobility and wireless communication in cyber-physical systems with application to robot teams. Proceedings of the IEEE, 100(1):164–178, 2012.

[11] Eric W. Frew. Sensitivity of cooperative target geolocalization to orbit coordination. AIAA Journal of Guidance, Control, and Dynamics, 31(4):1028–1040, July 2008.

[12] Eric W. Frew, Brian Argrow, Dale Lawrence, Jack Elston, and Maciej Stachura. Unmanned aircraft systems for communication and atmospheric sensing missions. In 2013 American Control Conference, June 2013.

[13] G. Fudge, P. Deignan, J. Anderson, E. Owoye, P. Scerri, and R. Glinton. Adaptive distributed sensing for emitter localization with autonomous uav team cooperation. In ASAP, 2007.

[14] A. Ghaffarkhah and Y. Mostofi. Communication-aware motion planning in mobile networks. IEEE Transactions on Automatic Control, 56(10):2478–2485, October 2011.

[15] B. Grocholsky. Information-theoretic control of multiple sensor platforms. Phd, The University of Sydney, 2002.

[16] Gabriel M. Hoffmann and Claire J. Tomlin. Mobile sensor network control using mutual information methods and particle filters. IEEE Transactions on Automatic Control, 55(1):32 – 47, 2010.

[17] C. Igel, N. Hansen, and S. Roth. Covariance matrix adaptation for multi-objective optimization. Evolutionary Computation, 15(1):1–28, 2007.

[18] Simon J. Julier and Jeffrey K. Uhlmann. A new extension of the kalman filter to nonlinear systems. In Int. Symp. Aerospace/Defense Sensing, Simul. and Controls, pages 182–193, 1997.

[19] Abdallah Kassir, Robert Fitch, and Salah Sukkarieh. Decentralised information gathering with communication costs. In IEEE International Conference on Robotics and Automation (ICRA), pages 2427–2432, 2012.

[20] C. Kim, D. Song, Y. Xu, and J. Yi. Localization of multiple unknown transient radio sources using multiple paired mobile robots with limited sensing ranges. Computer Science and Engineering Department, Texas A&M University, Tech. Rep, 2010.

[21] Andrew N. Kopeikin, Sameera S. Ponda, Luke B. Johnson, and Jonathan P. How. Multi-UAV Network Control through Dynamic Task Allocation: Ensuring Data-Rate and Bit-Error-Rate Support. In Wi-UAV 2012, 3rd International Workshop on Wireless Networking and Control for Unmanned Autonomous Vehicles at the IEEE GlobeComm Conference, Decemeber 2012.

[22] Andreas Krause, Carlos Guestrin, Anupam Gupta, and Jon Kleinberg. Near-optimal sensor placements: maximizing information while minimizing communication cost. In IPSN '06: Proceedings of the 5th international conference on Information processing in sensor networks, pages 2–10, New York, NY, USA, 2006. ACM.

[23] J. Le Ny, A. Ribeiro, and G.J. Pappas. Adaptive communication-constrained deployment of mobile robotic networks. In American Control Conference (ACC), 2012, pages 3742 –3747, June 2012.

[24] A. Logothetis, A. Isaksson, and R.J. Evans. An information theoretic approach to observer path design for bearings-only tracking. In Proceedings of the 36th IEEE Conference on Decision and Control (Cat. No.97CH36124), volume 4, pages 3132–3137, San Diego, CA, USA, 1997.

[25] L. Merino, F. Caballero, and A. Ollero. Active sensing for range-only mapping using multiple hypothesis. In Intelligent Robots and Systems (IROS), 2010 IEEE/RSJ International Conference on, pages 37–42, 2010.

[26] L. Mihaylova, T. Lefebvre, H. Bruyninckx, K. Gadeyne, and J. De Schutter. Active sensing for robotics - a survey. In in Proc. 5 th Intl Conf. On Numerical Methods and Applications, pages 316–324, 2002.

[27] Skip Miller. Uasusa. [online] `http://uasusa.com/`.

[28] G.L. Nemhauser, L.A. Wolsey, and M.L. Fisher. An analysis of approximations for maximizing submodular set functions - i. Mathematical Programming, 14:265–294, 1978.

[29] Open-mesh. B.A.T.M.A.N Advanced. [online] `http://www.open-mesh.org/`.

[30] Sameera S. Ponda, Luke B. Johnson, Andrew N. Kopeikin, Han-Lim Choi, and Jonathan P. How. Distributed planning strategies to ensure network connectivity for dynamic heterogeneous teams. IEEE Journal on Selected Areas in Communications, 30(5):861 – 869, June 2012.

[31] Zoya Popovic and Branko Popovic. Introductory Electromagnetics, chapter 24, pages 461–464. Prentice Hall, 2000.

[32] Theodore Rappaport. Wireless Communications: Principles and Practice, chapter 4, pages 138–141. Prentice Hall PTR, Upper Saddle River, NJ, USA, 2001.

[33] CloudCap Technology. Piccolo plus. [online] http://www.cloudcaptech.com/piccolo_plus.shtm.

[34] Hobby King. Skywalker x8. [online] http://www.hobbyking.com/hobbyking/store/__27132__skywalker_x_8_fpv_uav_flying_wing_2120mm.html.

[35] Hope RF. RFM22B Data Sheet. [online] https://www.sparkfun.com/datasheets/Wireless/General/RFM22B.pdf.

[36] Hope RF. RFM22B FSK transceiver. [online] "http://www.hoperf.com/rf_fsk/fsk/rfm22b.htm".

[37] OpenWRT Linux. [online] http://openwrt.org/.

[38] PC Engines. alix3d2. [online] http://www.pcengines.ch/alix3d2.htm.

[39] Research Engineering Center for Unmanned Vehicles. Nexstar uas. [online] http://recuv.colorado.edu/nexstar.

[40] Ubiquiti. [online] http://www.ubnt.com/.

[41] WiFi-Plus. WiFi 2.4GHz antennas & spec sheets. [online] http://www.wifi-plus.com/antennas/24ghzanennasspecs.html, 2011.

[42] Allison Ryan and J. Karl Hedrick. Particle filter based information-theoretic active sensing. Robotics and Autonomous Systems, 58(5):574–584, May 2010.

[43] D. Song, C.Y. Kim, and J. Yi. Monte carlo simultaneous localization of multiple unknown transient radio sources using a mobile robot with a directional antenna. In IEEE International Conference on Robotics and Automation (ICRA), Kobe, Japan, 2009.

[44] D.P. Spanos and R.M. Murray. Motion Planning with Wireless Network Constraints. In Proc. 2005 American Control Conference, Portland, OR, 2005.

[45] Maciej Stachura, Jack Elston, Brian Argrow, Eric Frew, and Cory Dixon. National airspace system integration strategy for nomadic missions with small uas. Handbook of Unmanned Aerial Vehicles, 2012.

[46] Maciej Stachura and Eric W. Frew. Cooperative target localization with a communication aware active sensor network. In AIAA Guidance, Navigation, and Control Conference, Toronto, Canada, August 2010.

[47] Maciej Stachura and Eric W. Frew. Cooperative target localization with a communication aware unmanned aircraft system. AIAA Journal of Guidance, Control, and Dynamics, 34(5), September 2011.

[48] Maciej Stachura and Eric W. Frew. Wifi localization experiments with an unmanned aircraft. In AIAA Guidance, Navigation, and Control Conference, Portland, OR, August 2011.

[49] William Stallings. Wireless Communications and Networks, chapter 5, pages 115–121. Prentice Hall, 2 edition, 2005.

[50] Byron D. Tapley, Bob E. Schutz, and George H. Born. Statistical Orbit Determination, chapter 4, pages 233–236. Elsevier, Inc, June 2004.

[51] D. Tardioli, A.R. Mosteo, L. Riazuelo, J.L. Villarroel, and L. Montano. Enforcing network connectivity in robot team missions. Int. J. Rob. Res., 29(4):460–480, April 2010.

[52] Sebastian Thrun, Wolfram Burgard, and Dieter Fox. Probabilistic Robotics (Intelligent Robotics and Autonomous Agents). The MIT Press, 2005.

[53] Neeti Wagle and Eric W. Frew. A particle filter approach to wifi target localization. In AIAA Guidance, Navigation, and Control Conference, Toronto, Canada, August 2010.

[54] Neeti Wagle and Eric W. Frew. Transfer learning for dynamic rf environments. In In Proceedings 2012 American Control Conference, Montreal, Canada, June 2012.

[55] M. Wall. GAlib: A C++ library of genetic algorithm components. [online] `http://lancet.mit.edu/ga/`, 1996.

[56] Jason L. Williams. Information Theoretic Sensor Management. PhD thesis, Massachusetts Institute of Technology, February 2007.

[57] Z. Xiang, S. Song, J. Chen, H. Wang, J. Huang, and X. Gao. A wireless lan-based indoor positioning technology. IBM J. Res. Dev., 48(5/6):617–626, 2004.

[58] Yuan Yan and Yasamin Mostofi. Co-Optimization of Communication and Motion Planning of a Robotic Operation under Resource Constraints and in Fading Environments. IEEE Transactions on Wireless Communications, pages 1–11, 2013.

[59] Shengwei Yu and C S George Lee. Mobility and routing joint design for lifetime maximization in mobile sensor networks. In 2011 IEEERSJ International Conference on Intelligent Robots and Systems, pages 2300–2305. IEEE, 2011.

[60] M.M. Zavlanos, M.B. Egerstedt, and G.J. Pappas. Graph-theoretic connectivity control of mobile robot networks. Proceedings of the IEEE, 99(9):1525–1540, 2011.

[61] M.M. Zavlanos, A. Ribeiro, and G.J. Pappas. Mobility amp; routing control in networks of robots. In Decision and Control (CDC), 2010 49th IEEE Conference on, pages 7545 –7550, December 2010.

[62] D. Zwillinger and S. Kokoska. CRC standard probability and statistics tables and formulae. CRC, 1999.

Appendix A

Appendix

A.1 Optimal Bounds for Submodular Functions

First, it is necessary to show that the utility function is a submodular set function, which is essentially a function with diminishing returns as more sensor trajectories are added. The definition comes from looking at the incremental value of adding trajectory j to some set of trajectories A, defined as $\rho_j(A) = J(A \cup \{j\}) - J(A)$. This results in the formal definition of a submodular set function

$$\rho_j(S) \geq \rho_j(T), \forall\ S \subseteq T \subseteq E \text{ and } j \in E - T \tag{A.1}$$

See [28] for more equivalent definitions. For the case of perfect communication, the utility function is submodular per planning epoch. For each vehicle to compute its own trajectory at each planning epoch, we establish a fixed planning hierarchy where each vehicle plans and then uploads it's plan, along with those higher in the order, to the next vehicle. Each vehicle plans its path by solving:

$$\tau_n^h = \arg\max_{\tau_n} J\left(\tau_n | \tau_{1:n-1}\right) \tag{A.2}$$

Note that the notation was relaxed, where $\{\tau_1, \ldots, \tau_n\} = \tau_{1:n}$. Vehicle n will now transmit a full trajectory vector $\tau_{1:n}$ to vehicle $n+1$. This will allow vehicle $n+1$ to plan with the same estimates as vehicle n.

$$
\begin{aligned}
J\left(\tau^{*},\tau^{h}\right) &= J\left(\tau^{h}\right)+\sum_{k=1}^{N}\left[J\left(\tau^{h},\tau^{*}_{1:\,k}\right)-J\left(\tau^{h},\tau^{*}_{1:\,k-1}\right)\right] \\
&\leq J\left(\tau^{h}\right)+\sum_{k=1}^{N}\left[J\left(\tau^{h}_{1:\,k-1},\tau^{*}_{k}\right)-J\left(\tau^{h}_{1:\,k-1},\emptyset\right)\right] \\
&\leq J\left(\tau^{h}\right)+\sum_{k=1}^{N}\left[J\left(\tau^{h}_{1:\,k-1},\tau^{h}_{k}\right)-J\left(\tau^{h}_{1:\,k-1},\emptyset\right)\right] \\
&= J\left(\tau^{h}\right)+\sum_{k=1}^{N}\left[J\left(\tau^{h}_{1:\,k}\right)-J\left(\tau^{h}_{1:\,k-1}\right)\right] \\
&= 2J\left(\tau^{h}\right)
\end{aligned}
\tag{A.3}
$$

The first step is true do to cancelling terms over the sum. The second step utilizes submodularity, the incremental gain will be more for a smaller set. The third step is due to τ^{h}_{k} being better than τ^{*}_{k} for the cost given that $\tau^{h}_{1:\,k-1}$ were chosen for the first $k-1$ terms by definition in the hierarchical planner. Using this result and re-arranging results in:

$$
\frac{1}{2}J\left(\tau^{*}\right)\leq J\left(\tau^{h}\right)\leq J\left(\tau^{*}\right) \tag{A.4}
$$

which proves that the hierarchical approach will be at least as good as half the optimal solution for perfect communication.

A.2 Estimation algorithms

Three estimation algorithms are compared for the RF localization problem. These are the Extended Kalman Filter (EKF), the Unscented Kalman Filter (UKF), and the Particle Filter (PF). This section provides an overview of each of these three algorithms.

A.2.1 EKF Development

The EKF utilizes linearized equations of a non-linear system to estimate the first two moments, mean and covariance, of the system [50]. The two main steps of the EKF are the time update and measurement update.

The first step of the EKF is the time update. Starting with a previous position estimate $\hat{\mathbf{x}}_k$ and covariance $\mathbf{P}_k$ and owing to the fact that the targets are stationary, the state and covariance are computed:

$$
\overline{\mathbf{x}}_{k+1}=\hat{\mathbf{x}}_k \tag{A.5}
$$

$$\overline{P}_{k+1} = Q_{k+1} + P_k \tag{A.6}$$

where $\mathbf{Q}_k = E[\mathbf{w}_k \mathbf{w}_k^T]$ is the process noise matrix.

The second step is the measurement update to process a new RSSI measurement, $\mathbf{z}_{k+1}$. First the deviations of the measurement from the predicted RSSI based on the estimated state $\overline{\mathbf{x}}_{k+1}$ and the aircraft position $\mathbf{u}_{k+1}$ is computed.

$$\mathbf{y}_{k+1} = \mathbf{z}_{k+1} - h(\overline{\mathbf{x}}_{k+1}, \mathbf{u}_{k+1}, 0) \tag{A.7}$$

Next, the Kalman gain is computed:

$$K = \overline{P}_{k+1} \tilde{H}^T (\tilde{H} \overline{P}_{k+1} \tilde{H}^T + R_{k+1}) \tag{A.8}$$

where the sensor noise covariance $R_k = E[\mathbf{v}_k \mathbf{v}_k^T]$ is assumed constant in time and the $\tilde{H}$ matrix is found using:

$$\tilde{H} = \nabla_{\mathbf{x}} h\left(\overline{\mathbf{x}}_{k+1}, 0\right) \tag{A.9}$$

which for this system is:

$$\tilde{H} = \left[\frac{-10\alpha(x - x_s)}{r^2 \log(10)}, \frac{-10\alpha(y - y_s)}{r^2 \log(10)}, 1, -10 \log_{10} r \right] \tag{A.10}$$

where $r = \|\mathbf{p}_{r,k} - \mathbf{p}_{s,k}\|$ is the range from the aircraft to the emitter. The last step is to update the estimate of the state and covariance.

$$\hat{\mathbf{x}}_{k+1} = \overline{\mathbf{x}}_{k+1} + K(\mathbf{y}_{k+1} - \tilde{H} \overline{\mathbf{x}}_{k+1}) \tag{A.11}$$

$$P_{k+1} = (I - K\tilde{H}) \overline{P}_{k+1} (I - K\tilde{H})^T + K R_{k+1} K^T \tag{A.12}$$

A.2.2 UKF Development

The UKF represents probability density functions as a select set of sample points that are propagated through the state and measurement equations. The main steps of the UKF are presented here, see reference [18] for more details.

The first step of the UKF is the time update. The time update equations for the RF localization problem is the same as for the EKF described above. The second step is the measurement update. Using the

result of the time update the $2n+1$ σ points are first, where n is the dimension of the state vector resulting in nine σ points using the matrix square root:

$$\begin{aligned} \chi_{k+1|k,0} &= \overline{\mathbf{x}}_{k+1} \\ \chi_{k+1|k,1:n} &= \overline{\mathbf{x}}_{k+1} + \gamma\sqrt{\overline{\mathbf{P}}_{k+1}} \\ \chi_{k+1|k,n+1:2n} &= \overline{\mathbf{x}}_{k+1} - \gamma\sqrt{\overline{\mathbf{P}}_{k+1}} \end{aligned} \tag{A.13}$$

where for this work $\gamma = \sqrt{3}$. Next, the measurement sigma points are computed by taking these sigma points and putting them through the observation equation.

$$Z_{k+1|k,i} = h(\chi_{k+1|k,i}, \mathbf{p}_{s,k+1}0)) \tag{A.14}$$

$$\overline{\mathbf{z}}_{k+1} = \sum_{i=0}^{2n} W_{m,i} Z_{k+1|k,i} \tag{A.15}$$

where $W_{m,i}$ are the measurement weights with $W_{m,0} = -\frac{1}{3}$ and $W_{m,i} = \frac{1}{6}$ for $i = 1 \ldots 8$. The measurement innovation and cross-correlation covariances are computed next,

$$P_{zz} = R_{k+1} + \sum_{i=0}^{2n} W_{c,i}(Z_{k+1|k,i} - \overline{\mathbf{z}}_{k+1})(Z_{k+1,i} - \overline{\mathbf{z}}_{k+1|k})^T \tag{A.16}$$

$$P_{xz} = \sum_{i=0}^{2n} W_{c,i}(\chi_{k+1|k,i} - \overline{\mathbf{x}}_{k+1})(Zk+1, i - \overline{\mathbf{z}}_{k+1|k})^T \tag{A.17}$$

where $\mathbf{R}_k = E[\mathbf{v}_k \mathbf{v}_k^T]$ is the sensor noise covariance and $W_{c,i}$ are the cross-correlation weights with values $W_{c,0} = \frac{5}{3}$ and $W_{c,i} = \frac{1}{6}$ for $i = 1 \ldots 8$. Finally the estimate and covariance for time $k+1$ are computed using:

$$P_{k+1|k+1} = \overline{P}_{k+1} - K P_{zz} K^T \tag{A.18}$$

where

$$K = P_{xz} P_{zz}^{-1} \tag{A.19}$$

Using the sensor measurement, $\mathbf{z}_{k+1}$ the new estimate and covariance are computed:

$$\hat{\mathbf{x}}_{k+1} = \overline{\mathbf{x}}_{k+1} + K(\mathbf{z}_{k+1} - \overline{\mathbf{z}}_{k+1}) \tag{A.20}$$

$$P_{k+1|k+1} = \overline{P}_{k+1} - P_{xz} P_{zz}^{-1} P_{xz}. \tag{A.21}$$

A.2.3 Particle Filter Development

The particle filter used in the localization comparison is developed next [53]. When localizing a point (in two or three dimensions) in presence of uncertainty, filtering techniques like Extended Kalman filter and Unscented Kalman filter have the advantage of providing a compact representation of the position estimate and its uncertainty. However, they fail to represent non-Gaussian and multi modal distributions[52], which can be easily handled by a particle filter.

The particle filter localizes each target using sampling importance re-sampling[52]. Each of the particles $\mathbf{x}_k^{[i]}$ $(i = 1, \ldots, M)$ in this particle filter represent a hypothesis of the state for a single RF source. Thus the state of the i^{th} particle at time step k is given by

$$\mathbf{x}_k^{[i]} = [x_k^{[i]} \quad y_k^{[i]} \quad \kappa_k^{[i]} \quad \alpha_k^{[i]}]^T$$

The particle filter is initialized at time step $k = 0$. During initialization, all its particles are uniformly distributed in a circular region centered around $\mathbf{p}_{UA}$. The radius of this circular region is set equal to the listening radius or maximum detection range. This fixed parameter initialization prevents the particle filter from failing due to an extremely noisy first measurement. The pessimistic and signal independent initialization of the particle filter increases the probability that the particle cloud covers the true location of the target.

In the case of static targets, the particles' states do not change. Hence the state time update is given by,

$$\mathbf{x}_{k+1}^{[i]} = \mathbf{x}_k^{[i]} + \mathbf{w}_k^{[i]} \qquad \forall i \tag{A.22}$$

where $\mathbf{w}_k^{[i]} \sim \mathcal{N}(\mathbf{0}, \mathbf{Q}_k)$ is the process noise.

The measurement equation 2.23 is used to predict the observation at each of the particles $\mathbf{x}_k^{[i]}$

$$\hat{\mathbf{z}}_{k+1}^{[i]} = h(\mathbf{x}_{k+1}^{[i]}, \mathbf{u}_{k+1}, 0) \tag{A.23}$$

Based on their predicted observations, the particles are weighted to determine the importance of their hypotheses. These importance weights are given by

$$w_{k+1}^{[i]} = \frac{1}{\sqrt{2\pi\mathbf{R_k}}} \exp\left[-\frac{1}{2}(\hat{\mathbf{z}}_{k+1}^{[i]} - \mathbf{z}_{k+1})^T \mathbf{R}_k^{-1} (\hat{\mathbf{z}}_{k+1}^{[i]} - \mathbf{z}_{k+1})\right] \tag{A.24}$$

The new state estimate of the target is given by

$$\hat{\mathbf{x}}_{k+1} = \frac{\sum_{i=1}^{M} w_{k+1}^{[i]} \mathbf{x}_{k+1}^{[i]}}{\sum_{i=1}^{M} w_{k+1}^{[i]}} \tag{A.25}$$

In order for the particles to approximate the target distribution i.e. $p(x_k|z_1, z_2, \ldots, z_k)$, they have to be re-sampled using importance weights. These re-sampled particles are propagated to the next time-step. Particles with higher weights i.e. particles that represent higher probability hypotheses have a higher chance of being re-sampled. Thus, re-sampling concentrates the particles in regions of higher probability.

This spread or distribution of the particles can be used to compute the estimated covariance matrix

$$\Sigma_{k+1} = \sum_{i=1}^{M} w_k^{[i]} \tilde{\mathbf{x}}_k^T \tilde{\mathbf{x}}_k \tag{A.26}$$

$$\text{where } \tilde{\mathbf{x}}_{k+1} = \mathbf{x} - \hat{\mathbf{x}}_{\mathbf{k+1}} \tag{A.27}$$

A.3 Single Vehicle Flight Trajectories

The following plots, Figures A.1 through A.8 contain trajectories for single vehicle flights conducted for localizing 433MHz RF emitters.

Figures A.9 through 6.5 contain trajectories for single vehicle flights conducted for localizing 433MHz RF emitters that utilize the planning algorithm.

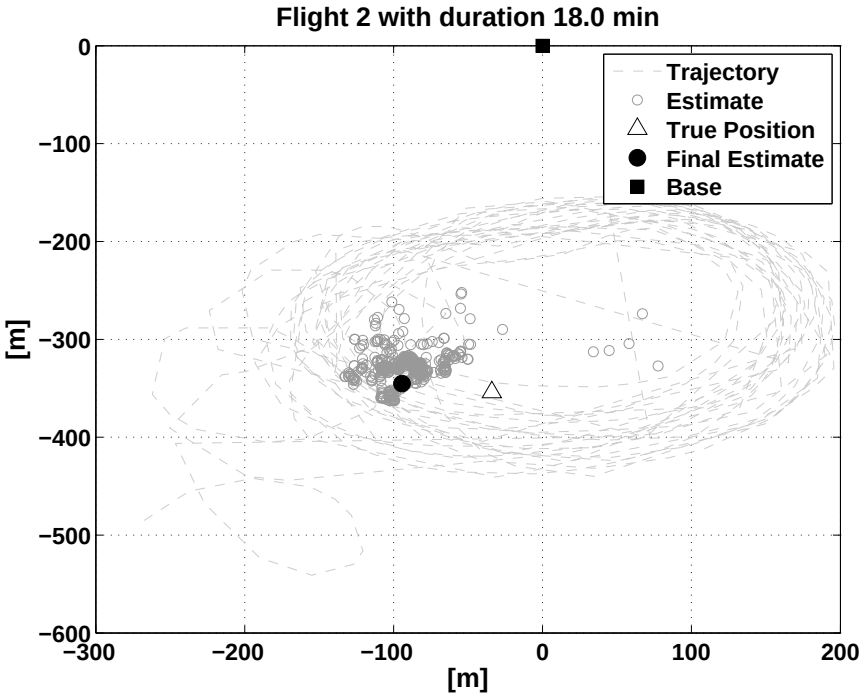

Figure A.1: The trajectory for a flight 2 with no planning

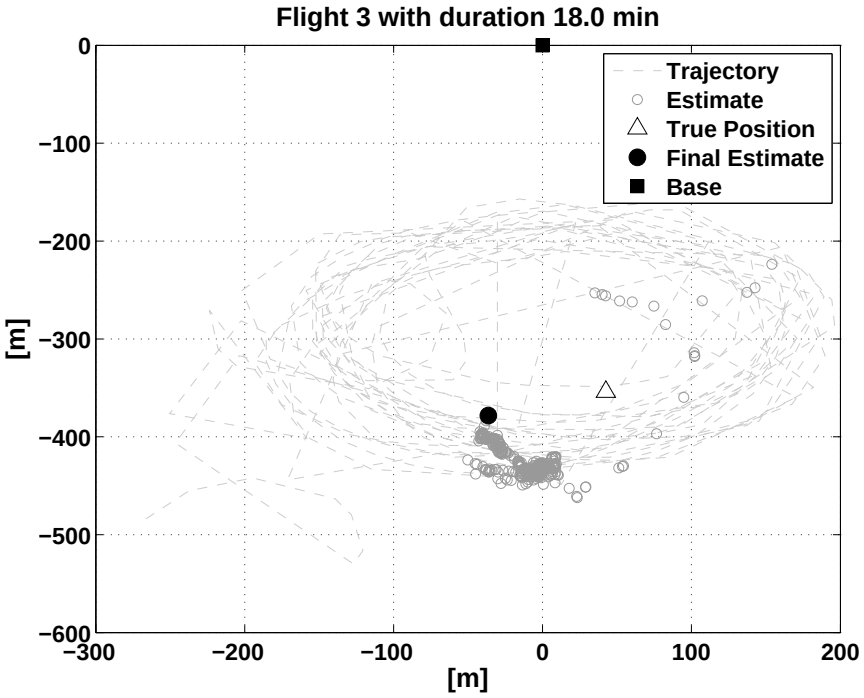

Figure A.2: The trajectory for a flight 3 with no planning

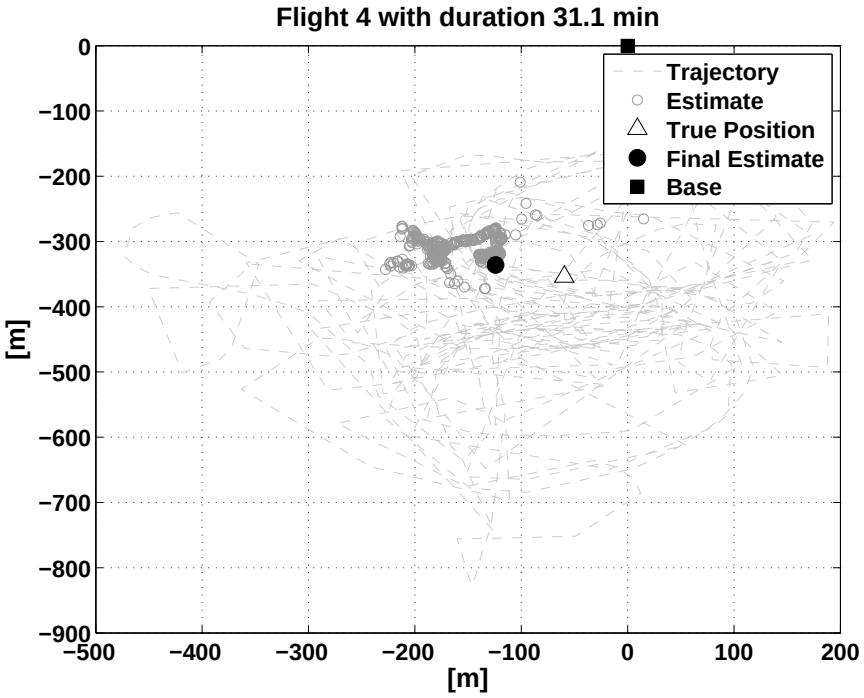

Figure A.3: The trajectory for a flight 4 with no planning

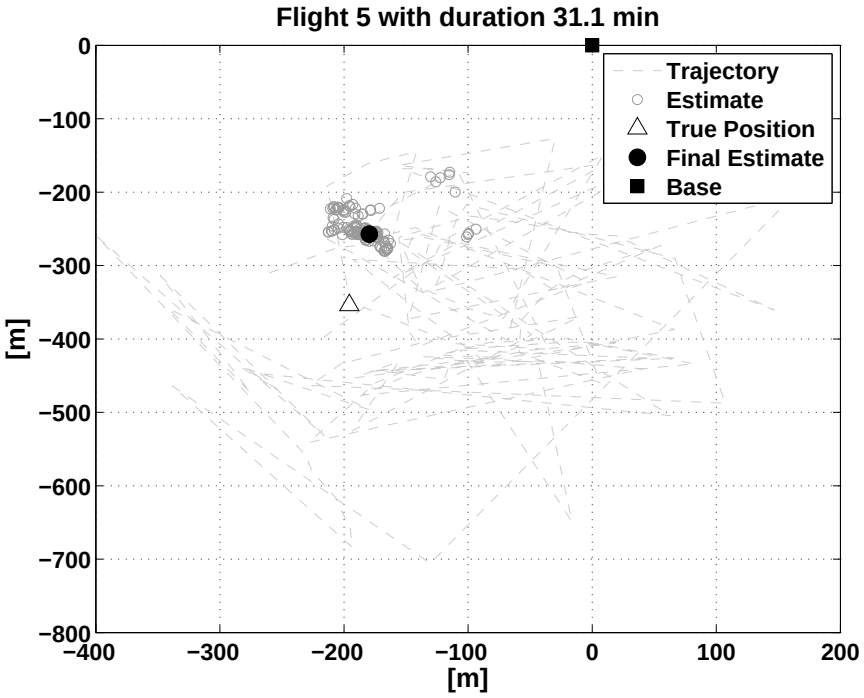

Figure A.4: The trajectory for a flight 5 with no planning

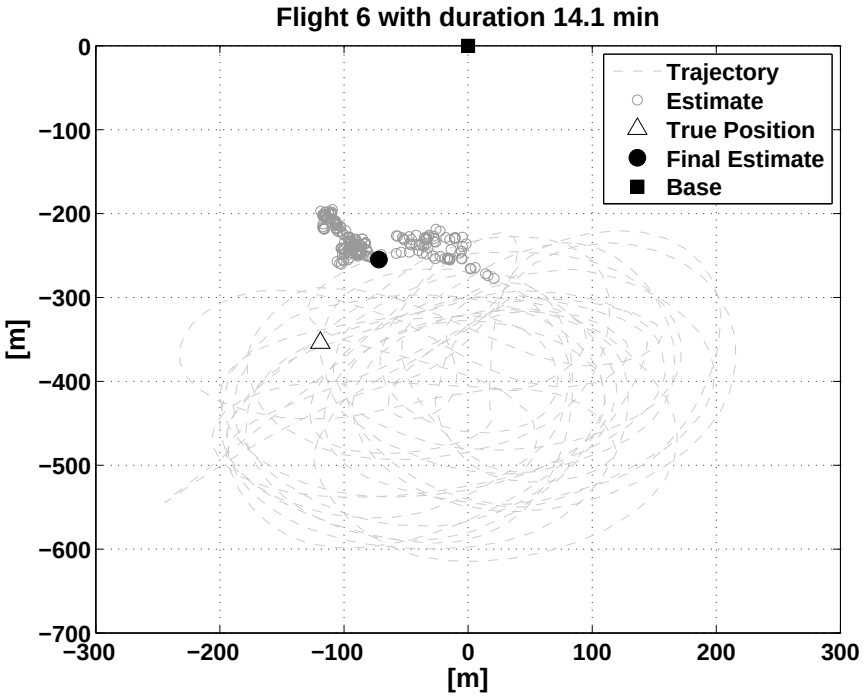

Figure A.5: The trajectory for a flight 6 with no planning

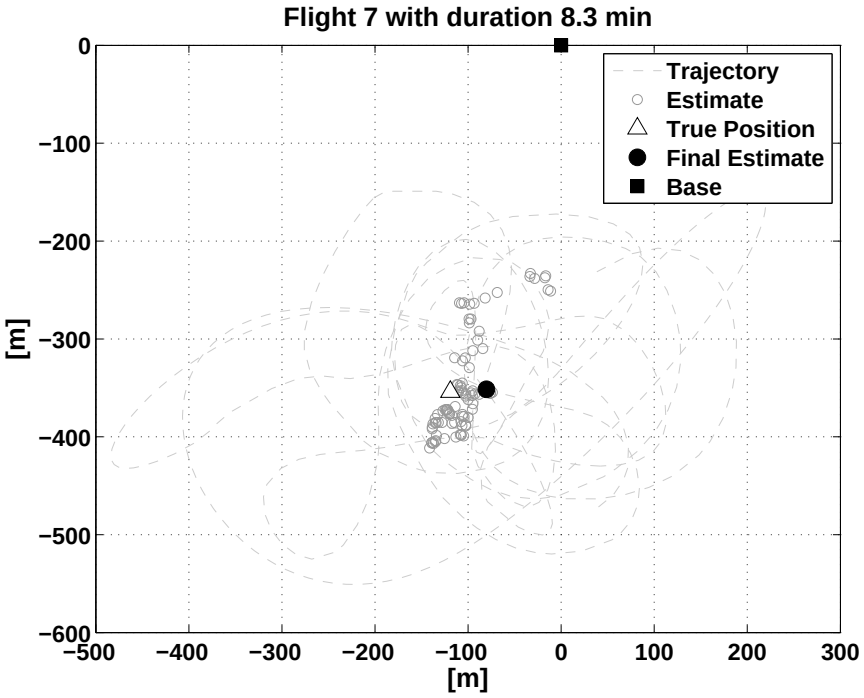

Figure A.6: The trajectory for a flight 7 with no planning

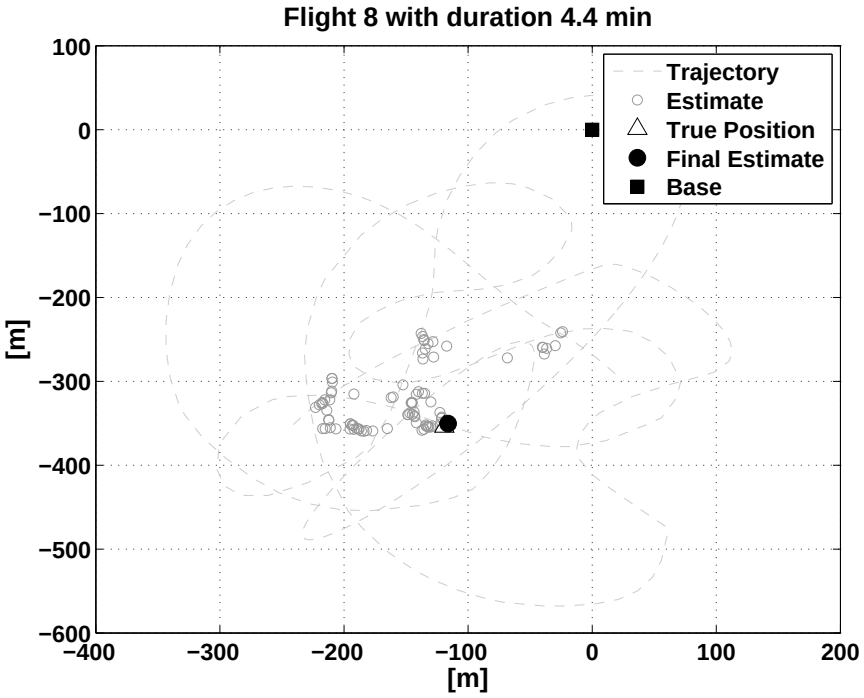

Figure A.7: The trajectory for a flight 8 with no planning

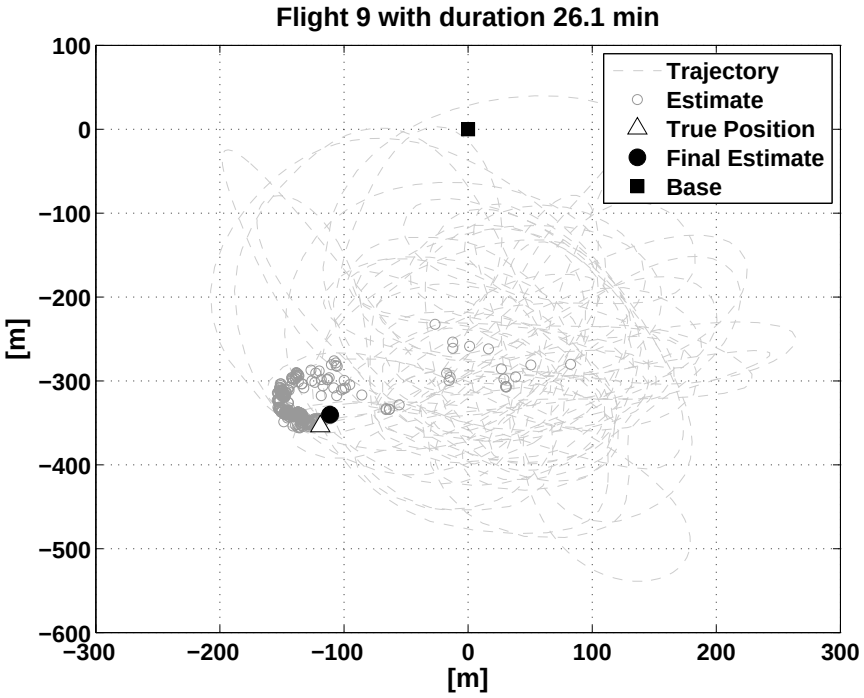

Figure A.8: The trajectory for a flight 9 with no planning

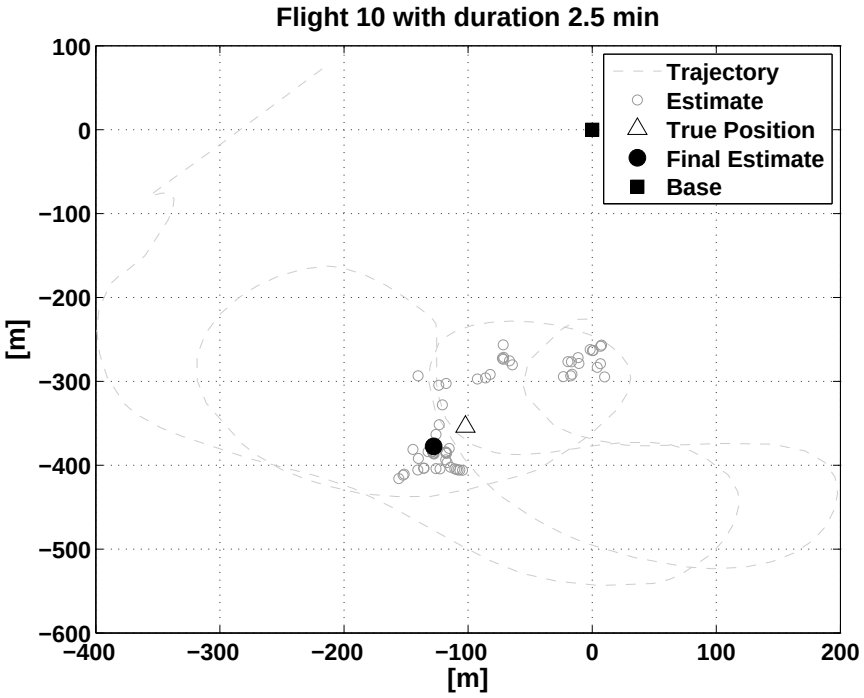

Figure A.9: The trajectory for a flight 10 with planning

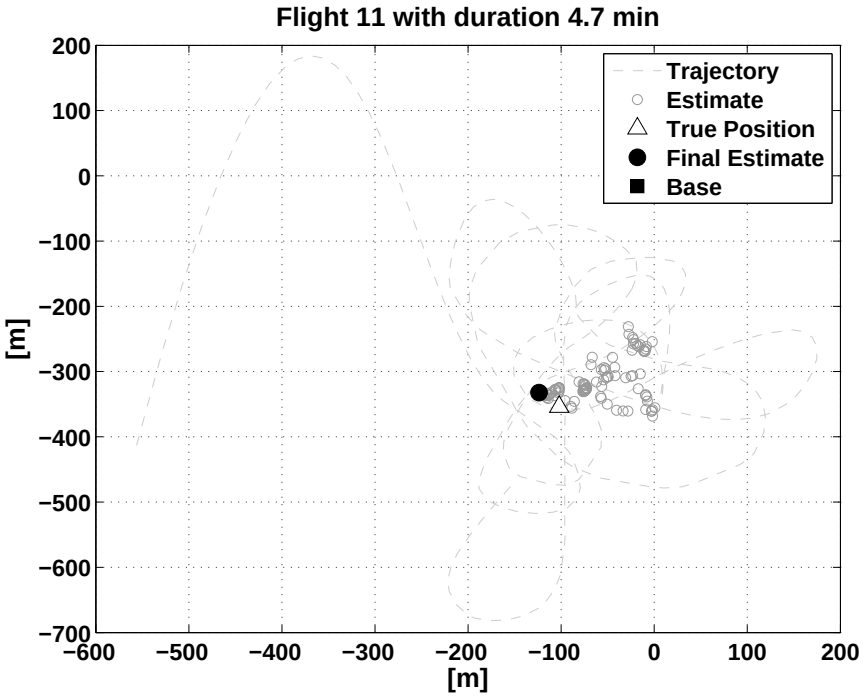

Figure A.10: The trajectory for a flight 11 with planning

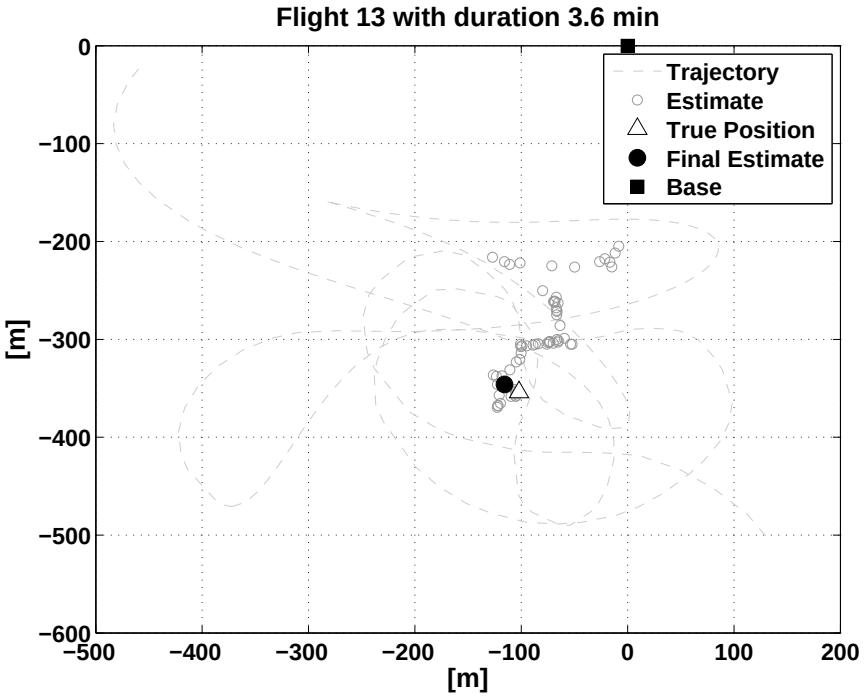

Figure A.11: The trajectory for a flight 13 with planning

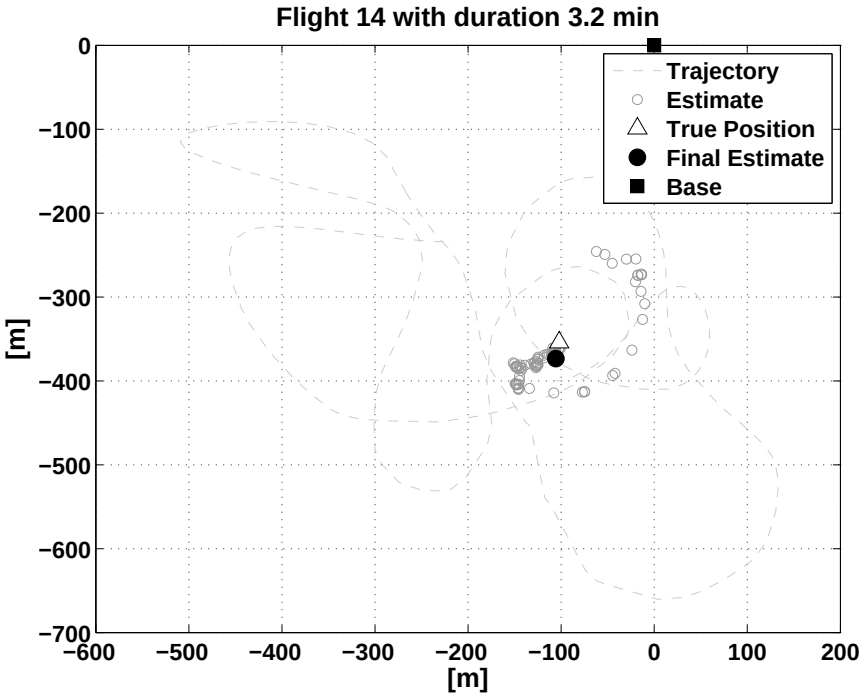

Figure A.12: The trajectory for a flight 14 with planning

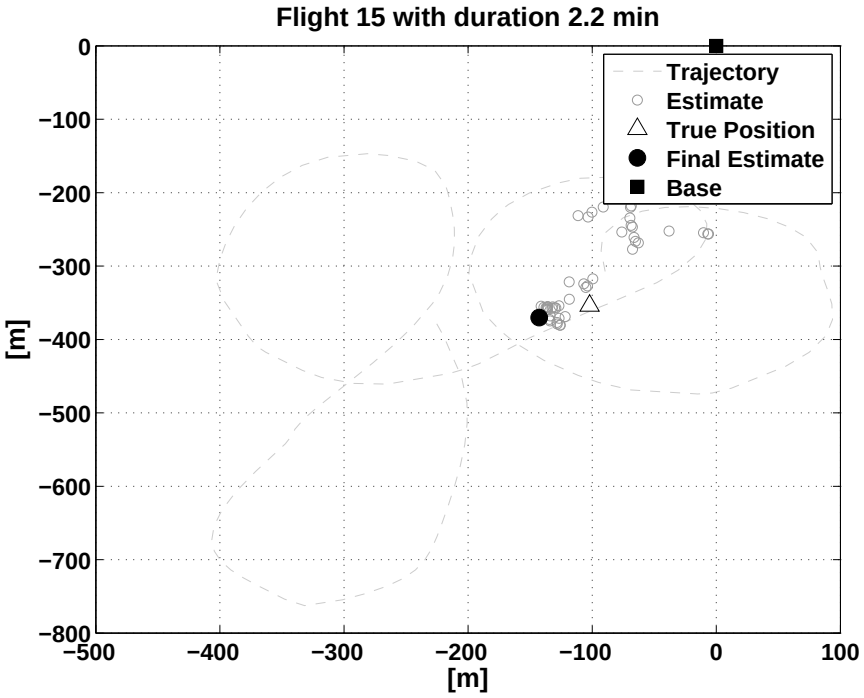

Figure A.13: The trajectory for a flight 15 with planning